

Phase Transitions in Collective Damage of Civil Structures under Natural Hazards

Sebin Oh^a, Jinyan Zhao^b, Raul Rincon^c, Jamie E. Padgett^c, Ziqi Wang^{a,*}

^a*Department of Civil and Environmental Engineering, University of California, Berkeley, CA, United States of America*

^b*Department of Mechanical and Civil Engineering, California Institute of Technology, Pasadena, CA, United States of America*

^c*Department of Civil and Environmental Engineering, Rice University, Houston, TX, United States of America*

Abstract

The fate of cities under natural hazards depends not only on hazard intensity but also on the coupling of structural damage, a collective process that remains poorly understood. Here we show that urban structural damage exhibits phase-transition phenomena. As hazard intensity increases, the system can shift abruptly from a largely safe to a largely damaged state, analogous to a first-order phase transition in statistical physics. Higher diversity in the building portfolio smooths this transition, but multiscale damage clustering traps the system in an extended critical-like regime—analogous to a Griffiths phase—suppressing the emergence of a more predictable disordered (Gaussian) phase. These phenomenological patterns are characterized by a random-field Ising model, with the external field, disorder strength, and temperature interpreted as the effective hazard demand, structural diversity, and modeling uncertainty, respectively. Applying this framework to real urban inventories reveals that widely used engineering modeling practices can shift urban damage patterns between synchronized and volatile regimes, systematically biasing exceedance-based risk metrics by up to 50% under moderate earthquakes ($M_w \approx 5.5\text{--}6.0$)—equivalent to a several-fold gap in repair costs. This phase-aware description turns the collective behavior of civil infrastructure damage into actionable diagnostics for urban risk assessment and planning.

Keywords: Natural hazards risk assessment, Phase transitions, Urban resilience

1. Introduction

Cities are increasingly exposed to natural hazards whose impacts extend far beyond individual buildings. The 2023 Kahramanmaraş earthquakes (M_w 7.8 and 7.5) severely damaged over 280,000 buildings and displaced millions, causing losses exceeding US\$34 billion [10, 36, 41]. Similarly, the 2024 Category 4 Hurricane

*Corresponding author

Email address: zqiwang@berkeley.edu(Ziqi Wang)

Helene unleashed catastrophic flooding across the southeastern United States, resulting in losses estimated at US\$78.7 billion [5, 27]. Such extensive impacts necessitate a move beyond parcel-level analysis toward regional assessments that capture the emergence of collective vulnerabilities [6, 26, 30, 31, 39].

Facilitating this shift, rapid advances in computational modeling and data availability have enabled the prediction of regional disaster impacts at unprecedented granularity [25, 38, 49]. Fine-grained building inventories, physics-based hazard models, and field reconnaissance data can now be integrated seamlessly into probabilistic analysis frameworks that evaluate hazard impacts at building-level resolution [3, 9, 46, 49]. This has spurred a widespread focus on fidelity: improving model accuracy, refining component-level physics, and accelerating simulations [9, 15, 18, 33, 43, 44], implicitly assuming that increasing local precision automatically yields a better understanding of global resilience.

Yet a fundamental question persists: even if every structure in a city could be modeled with absolute fidelity, would the governing principles of urban resilience emerge? We contend they would not. Beyond the barriers of computational cost, the sheer granularity of such an approach risks obscuring damage patterns behind a fog of detail. This mirrors the philosophy of statistical physics: the laws of thermodynamics emerge not from tracking individual molecular trajectories, but from identifying how micro-interactions organize into macro-behavior [19, 22]. Similarly, natural hazards engineering must transcend the pursuit of ever-finer resolution to uncover the universal organizing principles of collective structural response—insights that brute-force, high-resolution simulation alone can never yield.

Here we uncover the underlying physics that governs collective responses in city-scale building portfolios. Using large-scale nonlinear time-history analyses coupled with stochastic and physics-based earthquake models, we identify two phase transitions in structural damage. First, in regions with low structural diversity, the system exhibits a *synchronized state*, where regional damage can shift abruptly from largely safe to widespread failure, analogous to a first-order phase transition. Second, increasing diversity does not decouple the system into a predictable Gaussian average; instead, the inherent spatial clustering of structures traps cities in an extended critical-like regime—analogous to a Griffiths phase. In this *volatile state*, engineering predictions become highly sensitive to modeling details, undermining their reliability. Conventional portfolio-level simplifications can inadvertently toggle a city model between synchronized and volatile regimes, introducing systematic bias in tail-risk metrics. Consequently, establishing both the validity and fundamental limits of engineering predictions requires diagnosing these underlying regimes, calling for *phase-awareness* in city-scale hazard risk assessment.

2. Collective behavior in city-scale structural damage

Milpitas, California, a residential city in the San Francisco Bay Area, serves as the study region, with earthquakes considered as the representative hazard for the city (Fig. 1a). The analysis focuses on multistory buildings (two or more stories), which dominate regional seismic risk due to their greater vulnerability and damage consequences. Building-level data are integrated into multi-degree-of-freedom structural models, whose nonlinear time-history analyses yield statistical distributions of structural capacities. These capacities are evaluated against spatially correlated ground-motion fields to generate damage realizations, which are then aggregated into ensembles of damage fractions (see [Methods](#) and [Supplementary Note 1](#)).

As hazard intensity increases, the response shifts from a collectively safe to a collectively damaged state (Fig. 1c). At low magnitudes, most buildings remain undamaged; at high magnitudes, nearly all are damaged. While this trend is expected, the abruptness of the transition is striking: around $M_w = 5-6$, the collective state switches suddenly from safe to damaged. Within this range, the damage-fraction distributions become bimodal, peaking at the two extremes, indicating that the region tends to be either largely safe or largely damaged rather than partially so. This synchronization emerges under moderate-intensity hazards, where engineering decisions are most consequential yet most uncertain. Unlike weak or extreme events, where appropriate actions are relatively straightforward (ignore or fully mobilize), moderate events require calibrated preparedness, but their polarized outcomes make such decisions inherently complex. Extended Data Figs. 1 and 2 show the results for the full building portfolio, including single-story buildings.

Different cities may exhibit distinct collective behaviors under similar hazard conditions. To examine how the nature of the transition depends on the composition of the building portfolio, we vary structural diversity systematically. Specifically, we adjust the dispersion in structural capacities to represent cities with different levels of portfolio heterogeneity (Fig. 1b). This heterogeneity is parameterized by σ , which quantifies the *additional* dispersion in structural capacities across the region (see [Methods](#)), with $\sigma = 0$ denoting the real-inventory baseline. This allows us to trace how the collective response evolves with increasing structural diversity.

At high structural diversity, the bimodality observed at moderate magnitudes ($M_w = 5.6$ in Fig. 1d) is suppressed, smoothing the transition from collectively safe to collectively damaged states (Extended Data Fig. 3). Synchronization vanishes around $\sigma \approx 0.5$, where the damage-fraction distribution flattens and collective damage becomes highly volatile. Notably, increasing diversity does not drive the system immediately into a fully disordered phase; instead, it remains in a volatile regime with persistently high variability and non-Gaussian statistics.

To map the collective response across a wide range of earthquake magnitudes and structural diversities, we construct a heatmap of the most probable regional damage fraction (the mode) (Fig. 2b). Two synchronized states emerge: a collectively safe state (near-zero damage) and a collectively damaged state (near-complete damage). At low σ , the transition between them is sharp, marked by a narrow phase-coexistence band where the damage-fraction distribution is bimodal. Beyond a critical diversity $\sigma_c \approx 0.5$, the transition smooths into a broad volatile regime characterized by high-variance, non-Gaussian statistics. Analysis of the northeastern San Francisco portfolio, which spans diverse districts and is therefore more heterogeneous, corroborates this trend (Extended Data Figs. 2 and 4), demonstrating that greater heterogeneity weakens synchronization and broadens the transition.

Specific quantitative details, such as the exact shape of the transition boundary or the extent of the volatile regime, vary with modeling assumptions, but the core phenomenological features remain robust. Supplementary sensitivity analyses confirm that these collective behaviors consistently emerge across a spectrum of model fidelities, ranging from alternative probabilistic models to physics-based simulations involving finite-element analysis with seismic wave propagation (Supplementary Figs. 1–4). This consistency indicates that the observed regimes are not artifacts of specific modeling choices, but rather inherent regularities governing the interplay between hazards and structural systems.

These observed shifts in collective behaviors mirror phase transitions in ferromagnetic systems, where disorder modulates the abruptness of the transition. The resulting heatmap thus serves as an empirical phase diagram, motivating the statistical physics-based interpretation formalized in the next section.

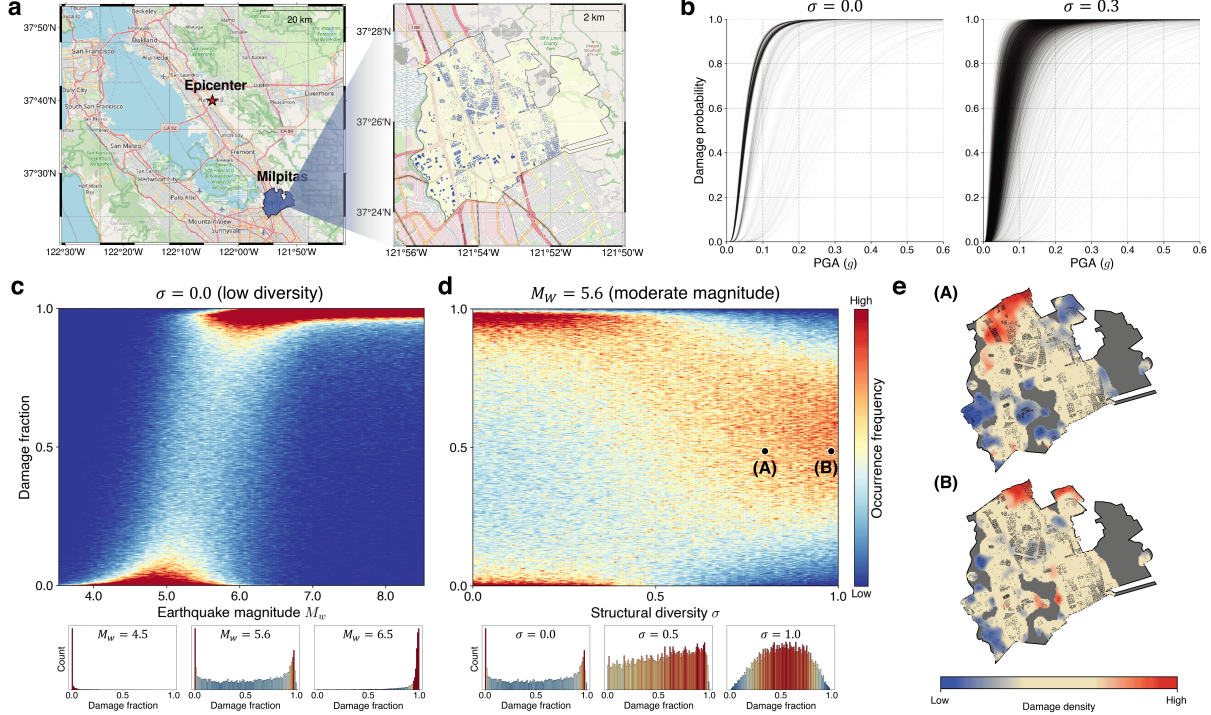


Fig. 1: **Collective structural responses and transition behavior in a city-scale building portfolio.** **a**, Study region and building distribution. Milpitas (San Francisco Bay Area), near the modeled earthquake epicenter (left). Locations of the 5,943 multistory buildings analyzed (right). **b**, Fragility curves for the Milpitas portfolio (left) and a counterpart with greater dispersion in structural capacity (right), representing a city with higher structural diversity. Here, σ quantifies additional heterogeneity introduced in structural capacity, with $\sigma = 0$ denoting the real-inventory baseline. A fragility curve probabilistically defines structural capacity in terms of peak ground acceleration (PGA), expressed in units of gravitational acceleration, g . **c**, Evolution of damage-fraction distributions with increasing earthquake magnitude at relatively low structural diversity, showing a jump from a collectively safe to a collectively damaged state, indicative of a first-order transition. The color scale denotes occurrence frequency. Snapshots at $M_w = 4.5$, 5.6 , and 6.5 are shown below. At moderate magnitudes ($M_w \approx 5$ – 6), the distributions become bimodal, revealing bistable collective response. **d**, Evolution of the distributions with increasing structural diversity at a moderate magnitude ($M_w = 5.6$). Greater diversity smooths the transition and suppresses bistability, yielding a continuous transition to an extended critical-like state characterized by non-Gaussian statistics. The histograms below show snapshots at $\sigma = 0$, 0.5 , and 1.0 . Markers (A) and (B) indicate the $\sigma = 0.8$ and 1.0 cases, respectively, mapped in panel **e**. **e**, Damage clustering at $(M_w, \sigma) = (5.6, 0.8)$ and $(5.6, 1.0)$. Colors indicate damage density (low to high); areas without buildings are masked (gray). Damage states of buildings form clusters across multiple spatial scales, counteracting the homogenization expected under the Central Limit Theorem.

3. Ising model interpretation for phase transitions

Regional-scale hazard risk can be interpreted through the lens of the Ising model, where binary spins correspond to the damaged or undamaged states of civil structures and the magnetic field represents the effective hazard demand [28]. We cast spatial heterogeneity among cities in the random-field Ising model (RFIM), whose Hamiltonian is

$$\mathcal{H}(\{s\}) = - \sum_i (H + h_i) s_i - \sum_{i < j} J_{ij} s_i s_j, \quad (1)$$

where s_i denotes the binary damage state of the i th building, H is the mean effective hazard demand, and h_i is a quenched local perturbation from that mean, capturing site- or building-specific variations in capacity or demand (Fig. 2a). The interaction term J_{ij} characterizes pairwise dependence between building damage, reflecting correlated vulnerabilities or shared environmental influences that give rise to collective damage. The system magnetization, $m = \frac{1}{N} \sum_{i=1}^N s_i$ with N spins, can then be interpreted as the regional damage fraction $m_d \in [0, 1]$ via a linear transformation from the spin domain $\{-1, 1\}$ to $\{0, 1\}$. Supplementary analyses further justify the use of damage fraction as the system's order parameter (Supplementary Method 1 and Supplementary Figs. 5–10).

A key distinction from the classical Ising-type models lies in its Z_2 symmetry. The conventional Ising system is symmetric under spin inversion when the external field is zero, whereas civil structures are inherently biased toward the safe state in the absence of hazard excitation. The inherent safety margin of engineered structures acts as an effective inertia opposing hazard excitation, shifting the zero-field condition to the point where this inertia balances the excitation [28].

Temperature is a key control parameter in the RFIM, and an analogous concept arises in regional hazard impact simulations. In the Ising model, temperature induces thermal fluctuations; spins may flip randomly even under fixed disorder [14, 22]. By contrast, regional simulations map a given realization of structural capacity and hazard demand deterministically to a binary outcome: damaged if demand exceeds capacity, undamaged otherwise. Each realization therefore corresponds to a zero-temperature limit. Introducing a non-zero temperature recasts this deterministic damage-assignment rule as a stochastic limit state, where temperature serves as a proxy for epistemic uncertainty (or the lack of confidence) in the hazard–structure model. Extended Data Figs. 5 and 6 summarize the resulting non-zero-temperature simulations (see Supplementary Method 2 for implementation).

In the zero-temperature limit, an RFIM with independent Gaussian disorder $h_i \sim \mathcal{N}(0, \Delta^2)$ and uniform

coupling $J_{ij} = J/N$ admits the mean-field self-consistent equation for the magnetization (see Supplementary Method 3),

$$m = \operatorname{erf}\left(\frac{Jm + H}{\sqrt{2}\Delta}\right), \quad (2)$$

where $\operatorname{erf}(\cdot)$ is the Gaussian error function. The stable solution of this equation, the equilibrium magnetization m^* , corresponds to the most probable regional damage fraction m_d^* under the linear spin-to-damage mapping. For each (M_w, σ) grid point obtained from engineering models, we infer (H, Δ) such that the RFIM reproduces the simulated m_d^* , yielding the mappings $H(M_w)$ and $\Delta(\sigma)$ (see Methods and Extended Data Fig. 7). Substituting these mappings into Eq. (2) yields the RFIM phase diagram, which effectively reconstructs the empirical phase diagram (Fig. 2b).

Free energy provides a comprehensive description of equilibrium behavior in statistical physics [14, 19, 22]. Using $H(M_w)$ and $\Delta(\sigma)$, we recast the associated mean-field free energy $F(m; H, \Delta)$ (see Supplementary Method 3) in terms of hazard and damage variables as $F(m_d; M_w, \sigma)$. The resulting free-energy landscapes capture both the abrupt, first-order transitions at low structural diversity and the smooth, continuous transitions at high structural diversity (Fig. 2c).

Within the RFIM framework, our empirical findings in Fig. 1 admit clear physical interpretations. When structural diversity is relatively low, effective couplings dominate local disorder, placing the city in an ordered state where buildings respond in synchronization to hazards; increasing hazard intensity then drives a sharp transition. At high structural diversity, one might expect local disorder to overwhelm coupling, yielding a fully disordered phase where aggregated metrics converge to Gaussian statistics. Yet, even at σ values where the dispersion of fragility curves becomes unrealistically broad (Extended Data Fig. 8), the system remains non-Gaussian, exhibiting high sensitivity to perturbations (slowly decaying susceptibility) and an elevated correlation length (Figs. 2d,e; see also Supplementary Method 4 and Supplementary Figs. 11 and 12). The persistence of a large correlation length indicates multiscale structure in the damage patterns: correlations decay slowly with separation distance (inset in Fig. 2e), producing damage clusters that span many sizes rather than being governed by a single characteristic scale (Fig. 1e). These anomalies suggest a Griffiths-like regime, likely sustained by the spatial clustering of building properties inherent to urban development (e.g., zoning and construction cohorts; Fig. 1e). In this volatile regime, the persistence of multiscale correlations dictates that aggregated risk metrics remain intrinsically sensitive to modeling details and preclude reliable predictions.

Overall, the RFIM provides a quantitative baseline for delineating collective damage phases. Its mean-field phase diagram condenses regional hazard responses into a two-dimensional space spanned by hazard

intensity and structural diversity, approximately capturing the critical-point location, the width of the phase-coexistence band, and the extent of the volatile regime. However, the mean-field solution predicts a fully disordered phase for $\sigma > \sigma_c$, missing the subtle Griffiths-like behavior observed in real portfolios. While the precise topology of the diagram varies across urban configurations—for instance, cities with skewed or multimodal disorder distributions can produce asymmetric boundaries or sequential transitions (Extended Data Figs. 1 and 2)—the core physics remains universal. The framework captures the fundamental competition between cooperative coupling and local disorder, governing the shift between synchronized damage and volatile fluctuations.

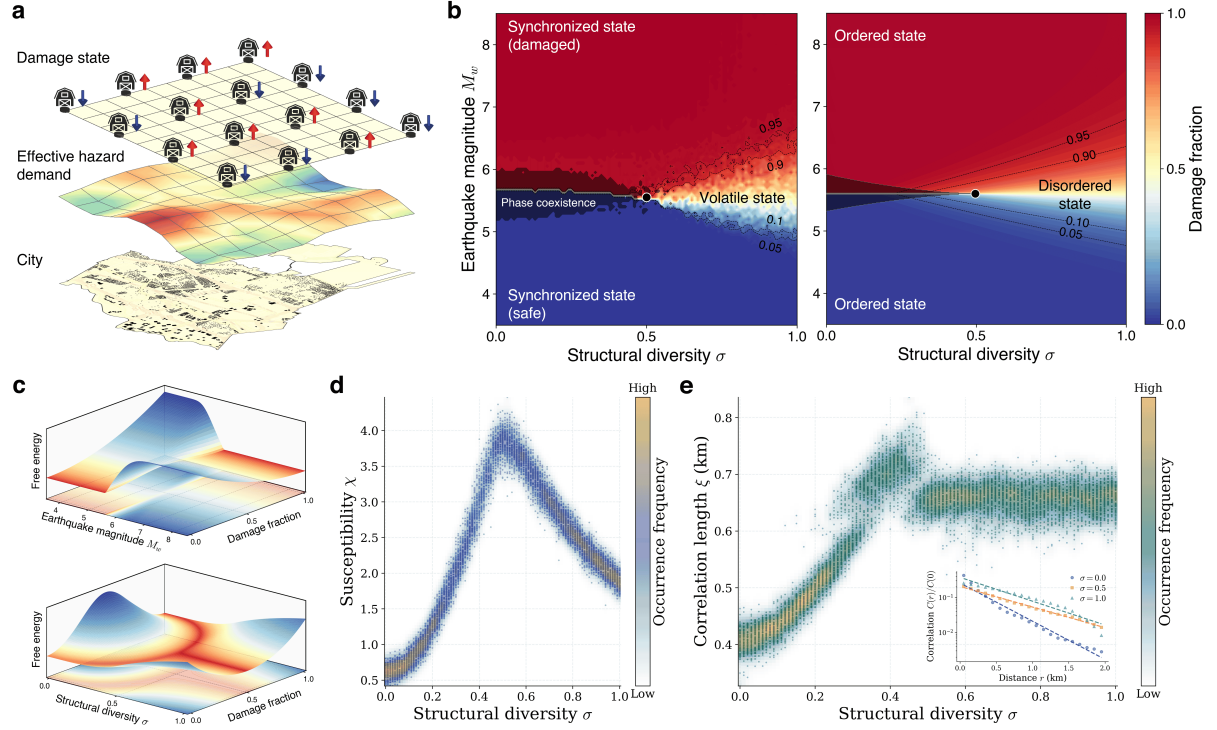


Fig. 2: Random-field Ising-model representation of collective structural damage transitions. **a**, In the random-field Ising model (RFIM) mapping, each building's damage state is represented as a binary spin. The effective hazard demand acts as an external field combining intrinsic safety bias and hazard-driven excitation; inter-building dependency induces collective response. **b**, Damage-fraction phase diagram from regional simulations for Milpitas (left) and the RFIM-reconstruction (right). Color denotes damage fraction, and contours indicate isodamage levels. The reconstruction captures the distinct collective states, the phase-coexistence band, and the critical point (black circle). **c**, Mean-field free energy landscapes $F(m_d; M_w, \sigma)$ at $\sigma = 0$ (top) and $M_w = 5.6$ (bottom), where m_d is the damage fraction. Increasing M_w drives an abrupt switch between free-energy minima, whereas increasing σ flattens and merges the minima, converting a discontinuous transition into a continuous crossover. Projections provide an RFIM-based reconstruction of Figs. 1c,d. **d**, Susceptibility peak and broadened critical region. Near the critical magnitude $M_{w_c} \approx 5.6$, we compute susceptibility χ from 50 independent portfolio realizations at each σ (see [Methods](#)) and summarize their distribution as a background heatmap. χ exhibits a pronounced but finite peak at $\sigma_c \approx 0.5$. The depleted density (absence of yellow) over $\sigma \in [0.3, 0.6]$ indicates strong realization-to-realization variability, consistent with a broadened critical regime (Griffiths-like behavior); in the volatile regime ($\sigma > \sigma_c$), χ decays slowly, reflecting persistent sensitivity. **e**, Correlation-length peak and persistence through the volatile regime. Using the same portfolio realizations, we estimate connected two-point correlations $C(r)$ (see [Methods](#)) and infer the correlation length ξ by fitting the decay $C(r)/C(0) \propto e^{-r/\xi}$ versus distance r (inset). The correlation length remains elevated for $\sigma > \sigma_c$, indicating persistent correlations across multiple spatial scales beyond criticality.

4. Phase-aware urban hazard risk assessment

Despite recent advances in regional-scale risk and resilience analysis for natural hazards, current engineering practices and design codes remain centered on individual structures, with limited consideration of their collective behavior at the city scale. For example, risk and loss assessment frameworks such as the *Hazus Earthquake Model Technical Manual*, published by Federal Emergency Management Agency (FEMA), classify buildings by coarse categories such as structural type, material, and construction year, and then assign capacities by class [11]. While efficient, such coarse categorization can impose artificial homogeneity within each class and obscure the diversity that governs the collective response [29]. Likewise, although spatial correlations of hazard intensities have long been recognized and incorporated into risk assessment guidelines [13, 17], correlations among structural capacities, arising from shared materials, typologies, or construction practices [4, 12, 20, 42, 45], have only recently begun to receive attention and remain under-represented [16]. Structural capacities are still often modeled as conditionally independent given hazard intensity [38], suppressing collective behavior and biasing regional decision metrics.

Fig. 3 quantifies the practical stakes of these assumptions by comparing regional repair-cost distributions in the north-eastern part of San Francisco, subjected to the same earthquake scenarios as the Milpitas case, with and without coarse structural categorization. Compared with the Milpitas building portfolio, the selected San Francisco region, which includes commercial districts such as the Financial District and Mission Bay and residential zones such as Pacific Heights and Hayes Valley, exhibits a more diverse building portfolio (Extended Data Fig. 9). Enforcing coarse categories narrows the portfolio's effective capacity spread and exacerbates collective clustering, changing the shape of the distribution and rendering spurious first-order phase transitional behavior. Fig. 3 further contrasts analyses with and without the conditional-independence assumption for the Milpitas portfolio; neglecting inter-building correlation obscures collective alignment in damage and leads to a biased distribution shape. In both cases, mean repair costs remain similar, yet the tails alter markedly; exceedance probabilities for repair costs are biased by up to 50% at moderate earthquake magnitudes ($M_w \approx 5.5\text{--}6.0$), and the 1% quantile repair cost is misestimated by up to one to two orders, ranging from a 30-fold underestimation under coarse categorization in San Francisco and to a 30-fold overestimation under conditional independence in Milpitas (Supplementary Figs 13 and 14). Since preparedness, resource prepositioning, and retrofit prioritization are governed by tail measures (e.g., exceedance probabilities, value-at-risk, or conditional value-at-risk), these assumption-driven shifts are decision-critical. The distributional change is most pronounced at moderate hazard intensities, where design and policy choices are most consequential and challenging, in contrast to weak or extreme hazards for which

decisions are relatively straightforward.

Viewed through the lens of collective phases, engineering simplifications do not merely reduce precision; they may shift a portfolio into an incorrect collective phase. Coarse structural categorization artificially synchronizes the modeled portfolio, inducing abrupt transitions, whereas the conditional-independence assumption pushes it toward the volatile regime. Phase distortion is most pronounced at moderate hazard intensity where the system is near a critical phase boundary, but becomes negligible under extreme hazards. Consequently, model validity is not absolute but contingent on the portfolio’s proximity to phase boundaries. This motivates a phase-aware diagnostic framework for constructing balanced engineering models that remain faithful to the underlying collective phase while maximizing efficiency. Crucially, such a framework identifies when a system enters the volatile regime, where critical-like behavior fundamentally constrains predictability and renders aggregated risk metrics intrinsically sensitive to modeling choices.

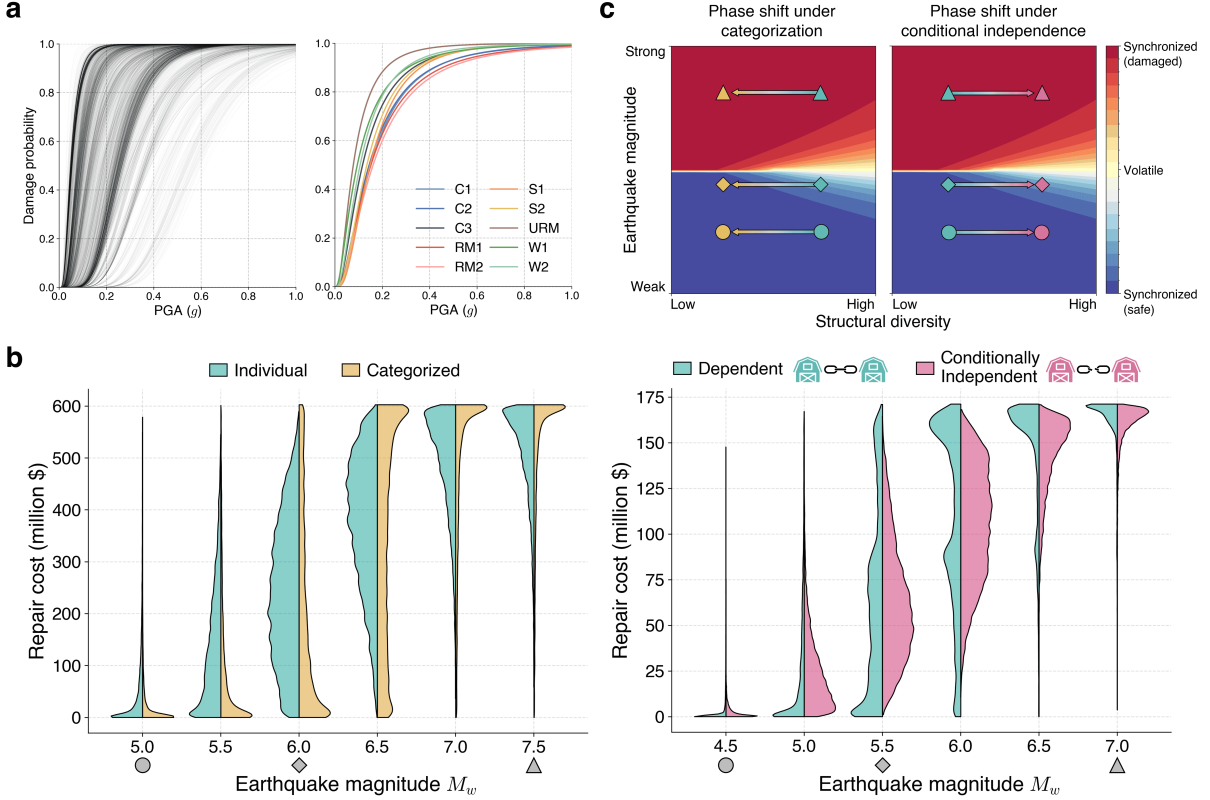


Fig. 3: Engineering implications of collective behavior and phase awareness. **a**, Fragility curves for the northeastern San Francisco building portfolio analyzed with (colored) and without (gray) coarse structural-type categorization. Categories for structural type are defined according to Hazus 6.1 [11]. **b**, Regional repair-cost distributions illustrating two common engineering simplifications: coarse structural-type categorization for the San Francisco portfolio (left) and conditional-independence assumption for the Milpitas portfolio (right). In San Francisco, replacing individual fragility curves (teal) with category-based curves (gold) imposes artificial homogeneity and reshapes the total repair-cost distributions, producing clustered behavior. In Milpitas, assuming conditionally independent structural capacities (pink) instead of explicitly dependent capacities (teal) suppresses collective alignment in damage and broadens the repair-cost distributions. In both cases, these distributional changes mainly alter quantile-based tail-risk metrics while leaving mean risk metrics largely unchanged. Marker symbols below the x-axis identify representative earthquake magnitudes used in panel **c**. **c**, Phase-diagram interpretation of the engineering simplifications. Background colors denote collective-risk phases; the two synchronized regimes correspond to collectively damaged (red) and collectively safe states (blue), respectively. Each simplification changes the inferred phase-diagram location of the same underlying portfolio by altering its effective heterogeneity: coarse categorization (left) reduces apparent diversity (moving the portfolio leftward), whereas the conditional-independence assumption (right) increases apparent diversity (moving it rightward). Under weak or strong hazards, these shifts do not change the qualitative phase, but at moderate intensities they can push the portfolio across the phase boundary. Such phase misrepresentation systematically distorts loss predictions, particularly in the tail of the distribution, where risk-informed decisions are most sensitive. Marker symbols correspond to the representative magnitudes in panel **b**.

5. Discussion

The emergence of collective damage regimes reveals that regional disaster risk follows universal laws of collective behavior. Rather than acting as a sum of independent building failures, a city behaves as a coupled system whose collective state is determined jointly by hazard intensity and structural diversity. The Random Field Ising Model captures these dynamics, demonstrating that the competition between inter-building coupling and local disorder governs whether the regional response is abrupt and synchronized, or continuous and volatile.

These findings generalize beyond seismic risk. Any hazard capable of imposing correlated demand across a region, such as hurricanes, floods, or wildfires, may induce similar collective phase transitions when interacting with the underlying heterogeneity of the built environment. Furthermore, this framework naturally extends to infrastructure networks, where failure can be redefined as functional outages in power grids, transportation blockages, or water supply disruptions. Future work utilizing scaled experiments that mimic the interplay of spatial correlation and disorder could provide physical validation of these predicted collective dynamics.

The statistical physics perspective also clarifies the fundamental limits of current engineering risk models. Simplifications that distort hazard correlations or structural diversity do not merely reduce precision; they can inadvertently shift a region across a phase boundary, fundamentally altering the nature of the predicted response. This is particularly critical when the system resides in the volatile phase, where persistent multiscale correlations slow the self-averaging of fluctuations. This non-Gaussian behavior imposes an intrinsic limit on predictability, leaving tail-risk metrics sensitive to modest modeling changes. Embedding phase awareness through diagnostics such as critical points or free-energy landscapes offers a path toward balanced engineering models that remain computationally practical while respecting the underlying physics of collective behavior.

More broadly, situating urban risk within the physics of critical phenomena reframes the paradigm of urban resilience modeling. Recognizing cities as complex systems operating near criticality reveals a fundamental limit to the constructionist approach: refining individual component models alone cannot capture the full risk landscape; it must be complemented by a macroscopic framework that navigates the transitions between collective stability and instability.

Methods

Regional simulation framework

The detailed framework for regional-scale structural response simulations is summarized in Supplementary Method 5, and the specific implementation used in this study is detailed in Supplementary Method 6.

Study regions and building inventories

Building-level attributes were obtained from the Natural Hazards Engineering Research Infrastructure (NHERI) database, which provides detailed inventory data for the San Francisco Bay Area, including the number of stories, construction year, and structural type [48]. Two representative regions were analyzed: Milpitas and northeastern San Francisco. The Milpitas dataset includes 5,943 buildings, predominantly residential, whereas the San Francisco dataset comprises 6,323 buildings spanning commercial districts such as the Financial District and Mission Bay, as well as residential neighborhoods including Pacific Heights and Hayes Valley. District boundaries were retrieved from the San Francisco Open Data Portal [8]. Extended Data Fig. 9 shows maps of the two regions and the distributions of structural attributes; detailed inventory statistics are provided in the Supplementary Figs. 15–18.

Structural modeling

Using the retrieved building attributes, multi-degree-of-freedom (MDOF) shear models were constructed for each building following established simulation frameworks [21, 25]. Each model reflected the building's material, typology, construction year, number of stories, height, and plan area, while each story was modeled as a zero-length element with a hysteretic uniaxial material capable of reproducing nonlinear stiffness degradation and pinching behavior. Story-wise stiffness and strength parameters were derived from the Hazus 6.1 Earthquake Model database [11] according to structural type and design era, and implemented in the open-source finite-element platform OpenSeesPy [24, 47]. The models were subjected to ground motions through a uniform base-excitation pattern applied at the structures' base supports, and the peak inter-story drift ratio was extracted as the primary engineering demand parameter (EDP).

Incremental Dynamic Analyses (IDA) [37] were conducted to estimate structural capacities using 100 empirical ground-motion records from the NGA-West2 database [2]. Each record was incrementally scaled until the structure reached its threshold EDP, defined as the EDP corresponding to the *slight* damage state according to the inter-story drift limits defined in Hazus 6.1 [11] for the respective structural type and construction era. A lognormal distribution is fitted to the resulting set of 100 capacity estimates

per building, whose cumulative density function represents the fragility curve for each building. Regional correlations among structural capacities were then computed from the ensemble of simulated capacities across all buildings in the study region.

To emulate cities with more heterogeneous building portfolios, we introduced variability in structural capacities. For each prescribed diversity level σ , we perturbed each building's median capacity (i.e., the mean of the log-capacity) by multiplying it by lognormal noise, whose logarithm has mean zero and standard deviation σ . This procedure effectively broadened the regional fragility-curve portfolio across a region, as illustrated in Extended Data Fig. 8.

Hazard modeling

A strike-slip earthquake scenario on the Hayward fault, representative of the San Francisco Bay Area, was defined with an epicenter at (37.666°N, 122.076°W), strike 325°, dip 90°, rake 180°, and a 3 km depth to the top of rupture. The moment magnitude M_w served as the intensity measure. Site conditions were assigned using V_{S30} values from the U.S. Geological Survey dataset [35]. These parameters defined the input for simulating spatially correlated ground motions under a California strike-slip mechanism.

For stochastic ground-motion field generation, we adopted the ground-motion prediction equation (GMPE) of Chiou and Youngs [7], applicable to active crustal regions in California, to compute the logarithmic mean and standard deviation of peak ground acceleration (PGA) for each site. Fault rupture length and width were estimated from the moment magnitude using the empirical scaling relations of Wells and Coppersmith [40]. Spatial correlation of intra-event residuals was modeled following Jayaram and Baker [17], with an exponential decay function calibrated for strike-slip mechanisms and soil conditions representative of the Bay Area. The resulting spatially correlated residual fields were superimposed on the GMPE-based median predictions to generate regional PGA maps consistent with the specified earthquake scenario.

To maximize the physical realism of generated ground-motion fields, the stochastically simulated intensity measures over Milpitas were cross-validated against physics-based simulations from the SCEC Broadband Platform (BBP) [23]. The BBP generates broadband (0-20+ Hz) seismic wave synthetics using a combination of physics-based components to simulate fault rupture and three-dimensional wave propagation. The same earthquake scenarios were used in both approaches. The comparison (Extended Data Fig. 10; Supplementary Figs. 19–22) shows close agreement in PGA levels and spatial variability within aleatory uncertainties.

Simulation procedure

For each seismic scenario, we generated building capacities and ground-motion demands, then evaluated damage deterministically. Capacities C_i (in g units) for building i were sampled from the fitted lognormal distributions with parameters calibrated from the IDA-based fragility analysis, including the IDA-derived correlations. Seismic demands D_i were sampled as lognormal from the GMPE median and variance, including inter- and intra-event residuals. Damage was assigned by the binary rule $I_i = \mathbb{1}\{D_i > C_i\}$, and the regional damage fraction was $m_d = \frac{1}{N} \sum_{i=1}^N I_i$ for N buildings. We performed 10,000 Monte Carlo realizations at each (M_w, σ) pair to obtain the distribution of m_d . The magnitude range was $M_w = 3.5$ to 8.5 in increments of 0.05 (101 values). The diversity parameter spanned $\sigma = 0.00$ to 1.00 in increments of 0.01 (101 values), with $\sigma = 0.00$ denoting code-specified structural parameters with no extra variability.

Loss and cost estimation

Repair costs were estimated using building-level data from the SimCenter Earthquake Testbed for the San Francisco Bay Area [48], which provides replacement and repair costs computed via the PELICUN framework [50]. The ratio between the provided repair and replacement costs was approximately 3%, corresponding to the *moderate* damage state in the Hazus 6.1 Earthquake Model [11]. Since this study focused on the *slight* damage state, repair costs were scaled by a factor of five to reflect the typical cost ratio between slight and moderate damage. For each simulated realization, the repair cost of building i was computed as $R_i = \text{Cost}_i I_i / 5$, where Cost_i is the building's replacement cost and I_i is the simulated binary damage indicator. The regional repair cost fraction was then $r = \frac{\sum_i R_i}{\sum_i \text{Cost}_i}$, representing the proportion of total replacement value requiring repair.

Construction of phase representations

Statistical heatmap construction

For each panel in which one parameter varies (the tuning parameter) while the other is held fixed, we aggregated outcomes across tuning-parameter values to form a two-dimensional histogram with axes given by the tuning parameter and the damage fraction m_d . Occurrence frequency was computed on a uniform grid with bin widths of 0.05 in M_w , 0.01 in σ , and 10^{-3} in m_d . To stabilize the color scale, counts were clipped at a robust upper cutoff and then normalized (95th percentile for the M_w panels; 99th percentile for the σ panels). The resulting normalized occurrence frequencies were rendered as 100-level filled contours, with the horizontal axis denoting the tuning parameter and the vertical axis denoting m_d .

Empirical phase representation

For the empirical phase diagram, we estimated the most probable damage fraction m_d^* at each (M_w, σ) grid point. We constructed a 100-bin uniform histogram of m_d , ranked bins by count, and averaged samples within the smallest set of top bins whose cumulative count exceeded 100 (1% of 10,000 simulations) to obtain a stable estimate. The resulting field $m_d^*(M_w, \sigma)$ was visualized as a 100-level filled contour map with σ on the horizontal axis and M_w on the vertical axis.

RFIM mapping and free-energy analysis

Parameter mapping

We estimated the RFIM mean-field parameters H and Δ on the (M_w, σ) grid by fitting m_d^* to the self-consistent equation $m = \text{erf}\left(\frac{m+a_1}{\sqrt{2}a_2}\right)$, fixing $J = 1$ so that $a_1 \equiv H$ and $a_2 \equiv \Delta$. We parameterized $a_1(M_w)$ and $a_2(\sigma)$ with low-order polynomials (quadratic in M_w ; non-decreasing linear in σ) and estimated coefficients by least squares over the grid. To stabilize the a_2 fit and avoid spurious bistability, we excluded data from the synchronized regime and applied a light regularization to suppress unrealistically sharp transitions. Extended Data Fig. 7 shows the fitted relations.

RFIM phase diagram

Using the fitted maps $a_1(M_w)$ and $a_2(\sigma)$, we numerically solved $m = \text{erf}\left(\frac{m+a_1}{\sqrt{2}a_2}\right)$ on the (M_w, σ) grid. At each grid point, we obtained the equilibrium magnetization m^* and used the corresponding damage fraction m_d^* for visualization. Because $a_2(\sigma)$ was fitted using data in the volatile regime, we extrapolated this relation into the synchronized regime. We identified the bistable region as grid points where solutions initialized from opposite states ($m_0 = \pm 1$) differed by more than 10^{-4} . The critical magnitude and diversity, M_{w_c} and σ_c , were then inferred from the fitted free energy (see [Methods](#), *Identification of critical magnitude and diversity*).

Free-energy landscape

The corresponding mean-field free energy (see [Supplementary Method 3](#)),

$$F(m; M_w, \sigma) = \frac{1}{2}m^2 - (m + a_1(M_w)) \text{erf}\left(\frac{m + a_1(M_w)}{\sqrt{2}a_2(\sigma)}\right) - \sqrt{\frac{2}{\pi}} a_2(\sigma) \exp\left(-\frac{(m + a_1(M_w))^2}{2(a_2(\sigma))^2}\right) + C,$$

was evaluated on dense grids in m over slices at fixed M_w or fixed σ , with $C = 0$. Since only relative differences in F are physically meaningful, each slice was normalized by subtracting its minimum and

dividing by the global maximum height (after minimum subtraction). For visualization in Fig. 2c, we applied a power-law normalization to emphasize low-energy basins corresponding to equilibrium states, and mapped m to m_d .

Identification of critical magnitude and diversity

The critical magnitude M_{w_c} is the point at which the equilibrium magnetization m changes sign, which in the mean-field form corresponds to $a_1(M_w) = 0$. From the fitted relation, this occurs at $M_{w_c} \approx 5.6$ for the benchmark Milpitas case at $\sigma = 0.0$. The critical diversity σ_c , beyond which m varies smoothly with increasing M_w and no abrupt change occurs, is defined by the condition $\frac{d^2F}{dm^2}|_{m=0} = 0$. Evaluating this condition for the mean-field free energy yields $a_{2c} = \sqrt{2/\pi}$, corresponding to $\sigma_c \approx 0.49$.

Susceptibility and correlation estimation

For the ensemble at fixed (M_w, σ) , we first identified an equilibrium range. We then estimated susceptibility from equilibrium fluctuations of the damage fraction m as $\chi = N \text{Var}(m) = N (\langle m^2 \rangle - \langle m \rangle^2)$, where $\langle \cdot \rangle$ denotes an ensemble average over equilibrium samples and N is the number of buildings. This fluctuation-based definition serves as a practical proxy for linear-response sensitivity to an external-field perturbation. Spatial dependence was quantified using the connected two-point correlation $C(i, j) = \langle s_i s_j \rangle - \langle s_i \rangle \langle s_j \rangle$. We radially averaged $C(i, j)$ over all distinct pairs by separation r_{ij} (bin width Δr) to obtain $C(r)$, and reported $C(r)/C(0)$, where $C(0)$ is the mean on-site variance. We repeated the analysis over 50 independent portfolio realizations to obtain robust distributions of χ and ξ (Supplementary Method 4).

References

- [1] Amnon Aharony. Tricritical points in systems with random fields. *Physical Review B*, 18(7):3318–3327, October 1978. ISSN 0163-1829. doi: 10.1103/PhysRevB.18.3318. URL <https://link.aps.org/doi/10.1103/PhysRevB.18.3318>.
- [2] Timothy D. Ancheta, Robert B. Darragh, Jonathan P. Stewart, Emel Seyhan, Walter J. Silva, Brian S.-J. Chiou, Katie E. Wooddell, Robert W. Graves, Albert R. Kottke, David M. Boore, Tadahiro Kishida, and Jennifer L. Donahue. NGA-West2 Database. *Earthquake Spectra*, 30(3):989–1005, August 2014. ISSN 8755-2930, 1944-8201. doi: 10.1193/070913EQS197M. URL <https://journals.sagepub.com/doi/10.1193/070913EQS197M>.
- [3] Karen Angeles and Tracy Kijewski-Correa. Advancing parcel-level hurricane regional loss assessments using open data and the regional resilience determination tool. *International Journal of Disaster Risk Reduction*, 95:103818, September 2023. ISSN 22124209. doi: 10.1016/j.ijdrr.2023.103818. URL <https://linkinghub.elsevier.com/retrieve/pii/S2212420923002984>.
- [4] Jack W Baker, Ed Almeter, Dustin Cook, Abbie B Liel, and Curt Haselton. A model for partially dependent component damage fragilities in seismic risk analysis. *Earthquake Spectra*, 40(1):609–628, February 2024. ISSN 8755-2930, 1944-8201. doi: 10.1177/87552930231205790. URL <https://journals.sagepub.com/doi/10.1177/87552930231205790>.
- [5] Michael J. Brennan and John P. Cangialosi. Tropical Cyclone Report: Hurricane Helene (AL092024). Technical report, National Hurricane Center, National Oceanic and Atmospheric Administration (NOAA), Miami, FL, USA, October 2024. URL https://www.nhc.noaa.gov/data/tcr/AL092024_Helene.pdf.
- [6] Sergey V. Buldyrev, Roni Parshani, Gerald Paul, H. Eugene Stanley, and Shlomo Havlin. Catastrophic cascade of failures in interdependent networks. *Nature*, 464(7291):1025–1028, April 2010. ISSN 0028-0836, 1476-4687. doi: 10.1038/nature08932. URL <https://www.nature.com/articles/nature08932>.
- [7] Brian S.-J. Chiou and Robert R. Youngs. Update of the Chiou and Youngs NGA Model for the Average Horizontal Component of Peak Ground Motion and Response Spectra. *Earthquake Spectra*, 30(3):1117–1153, August 2014. ISSN 8755-2930, 1944-8201. doi: 10.1193/072813EQS219M. URL <https://journals.sagepub.com/doi/10.1193/072813EQS219M>.

[8] City and County of San Francisco. Analysis neighborhoods. <https://data.sfgov.org/dataset/Analysis-Neighborhoods/p5b7-5n3h>, 2024. Accessed October 21, 2025.

[9] Laxman Dahal, Henry Burton, and Kuanshi Zhong. High-Fidelity High-Resolution Regional Seismic Risk and Resilience Assessment of Large Building Inventories. *Earthquake Engineering & Structural Dynamics*, 54(5):1376–1396, 2025. ISSN 1096-9845. doi: 10.1002/eqe.4313. URL <https://onlinelibrary.wiley.com/doi/abs/10.1002/eqe.4313>. _eprint: <https://onlinelibrary.wiley.com/doi/pdf/10.1002/eqe.4313>.

[10] Abdullah Dilsiz, Selim Gunay, Khalid Mosalam, Eduardo Miranda, Carlos Arteta, Halil Sezen, Erica Fischer, Manouchehr Hakhamaneshi, Wael Hassan, Bilal ALhawamdeh, Samuel Andrus, Jorge Archbold, Safak Arslanturkoglu, NURULLAH BEKTAS, Luis Ceferino, Jade Cohen, Burak Duran, Kalil Erazo, Gloria Faraone, Tali Feinstein, Rajendra Gautam, Abhineet Gupta, Salah Haj Ismail, Amalesh Jana, Sajad Javadinasab Hormozabad, Amarnath Kasalanati, Maha Kenawy, Zeyad Khalil, Irene Liou, Marko Marinkovic, Amory Martin, Yvonne Merino-Peña, Maziar Mivehchi, Luis Moya, César Pájaro Miranda, nicolas quintero, Juliana Rivera, Xavier Romão, Maria Camila Lopez Ruiz, Shokrullah Sorosh, Laura Vargas, Pulkit Dilip Velani, Hartanto Wibowo, Susu Xu, TANER YILMAZ, Mohammad Alam, Gabor Holtzer, Tracy Kijewski-Correa, Ian Robertson, David Roueche, and Amir Safey. StEER: 2023 Mw 7.8 Kahramanmaraş, Türkiye Earthquake Sequence Preliminary Virtual Reconnaissance Report (PVRR). Technical report, Designsafe-CI, 2023. URL <https://www.designsafe-ci.org/data/browser/public/designsafe.storage.published/PRJ-3824/#detail-942732811040452115-242ac11b-0001-012/?version=2>.

[11] Federal Emergency Management Agency (FEMA). Hazus Earthquake Model Technical Manual: Hazus 6.1. Technical report, Federal Emergency Management Agency, Washington, D.C., July 2024. URL <https://www.fema.gov/flood-maps/products-tools/hazus>.

[12] Jayadipta Ghosh, Keivan Rokneddin, Jamie E. Padgett, and Leonardo Dueñas-Osorio. Seismic Reliability Assessment of Aging Highway Bridge Networks with Field Instrumentation Data and Correlated Failures, I: Methodology. *Earthquake Spectra*, 30(2):795–817, May 2014. ISSN 8755-2930, 1944-8201. doi: 10.1193/040512EQS155M. URL <https://journals.sagepub.com/doi/10.1193/040512EQS155M>.

[13] K. Goda and H. P. Hong. Spatial Correlation of Peak Ground Motions and Response Spectra. *Bulletin of the Seismological Society of America*, 98(1):354–365, February 2008. ISSN 0037-1106. doi: 10.1785/0120070078. URL <https://pubs.geoscienceworld.org/bssa/article/98/1/354-365/341898>.

[14] Nigel Goldenfeld. *Lectures on Phase Transitions and the Renormalization Group*. CRC Press, 1 edition, March 2018. ISBN 978-0-429-49349-2. doi: 10.1201/9780429493492. URL <https://www.taylorfrancis.com/books/9780429962042>.

[15] Himadri Sen Gupta, Omar N. Nofal, Andrés D. González, Charles D. Nicholson, and John W. Van De Lindt. Machine Learning-Based Prediction of Optimal Building-Level Flood Mitigation Strategies in At-Risk Communities. *Natural Hazards Review*, 26(4):04025044, November 2025. ISSN 1527-6988, 1527-6996. doi: 10.1061/NHREFO.NHENG-2330. URL <https://ascelibrary.org/doi/10.1061/NHREFO.NHENG-2330>.

[16] Pablo Heresi and Eduardo Miranda. RPBEE: Performance-based earthquake engineering on a regional scale. *Earthquake Spectra*, 2023. ISSN 19448201. doi: 10.1177/87552930231179491. Publisher: SAGE Publications Inc.

[17] Nirmal Jayaram, Jack W Baker, N Jayaram, and J W Baker. Correlation model for spatially distributed ground-motion intensities. *Earthquake Engineering & Structural Dynamics*, 38(15):1687–1708, 12 2009. ISSN 1096-9845. doi: 10.1002/EQE.922. URL <https://onlinelibrary.wiley.com/doi/full/10.1002/eqe.922> <https://onlinelibrary.wiley.com/doi/abs/10.1002/eqe.922> <https://onlinelibrary.wiley.com/doi/10.1002/eqe.922>.

[18] Luke T. Jenkins, Maggie J. Creed, Karim Tarbali, Manoranjan Muthusamy, Robert Šakić Trogrlić, Jeremy C. Phillips, C. Scott Watson, Hugh D. Sinclair, Carmine Galasso, and John McCloskey. Physics-based simulations of multiple natural hazards for risk-sensitive planning and decision making in expanding urban regions. *International Journal of Disaster Risk Reduction*, 84:103338, January 2023. ISSN 22124209. doi: 10.1016/j.ijdrr.2022.103338. URL <https://linkinghub.elsevier.com/retrieve/pii/S221242092200557X>.

[19] Leo Kadanoff. *Statistical physics: statics, dynamics, and renormalization*. World Scientific, 2000. ISBN 978-981-02-3764-6.

[20] Chulyoung Kang, Oh Sung Kwon, and Junho Song. Evaluation of correlation between engineering demand parameters of structures for seismic system reliability analysis. *Structural Safety*, 93, 11 2021. ISSN 01674730. doi: 10.1016/j.strusafe.2021.102133.

[21] Xinzheng Lu, Frank McKenna, Qingle Cheng, Zhen Xu, Xiang Zeng, and Stephen A Mahin. An open-source framework for regional earthquake loss estimation using the city-scale nonlinear time history

analysis. *Earthquake Spectra*, 36(2):806–831, May 2020. ISSN 8755-2930, 1944-8201. doi: 10.1177/8755293019891724. URL <https://journals.sagepub.com/doi/10.1177/8755293019891724>.

[22] Shang-Keng Ma. *Modern theory of critical phenomena*. Routledge, 2019. ISBN 978-0-367-09537-6.

[23] P. J. Maechling, F. Silva, S. Callaghan, and T. H. Jordan. SCEC Broadband Platform: System Architecture and Software Implementation. *Seismological Research Letters*, 86(1):27–38, January 2015. ISSN 0895-0695, 1938-2057. doi: 10.1785/0220140125. URL <https://pubs.geoscienceworld.org/srl/article/86/1/27-38/315492>.

[24] Frank McKenna. OpenSees: A Framework for Earthquake Engineering Simulation. *Computing in Science & Engineering*, 13(4):58–66, 2011.

[25] Frank McKenna, Stevan Gavrilovic, Jinyan Zhao, Kuanshi Zhong, Adam Zsarnoczay, Barbaros Cetiner, Sina Naeimi, Sang ri Yi, Akash Bangalore Satish, Amin Packzad, Pedro Arduino, and Wael Elhaddad. NHERI-SimCenter/R2DTool: Version 5.5.0 (v5.5.0), 2025. URL <https://doi.org/10.5281/zenodo.16884221>. NHERI SimCenter, Rapid Regional Resilience Determination Tool (R2DTool).

[26] Chandrakala Meena, Chittaranjan Hens, Suman Acharyya, Simcha Haber, Stefano Boccaletti, and Baruch Barzel. Emergent stability in complex network dynamics. *Nature Physics*, 19(7):1033–1042, July 2023. ISSN 1745-2473, 1745-2481. doi: 10.1038/s41567-023-02020-8. URL <https://www.nature.com/articles/s41567-023-02020-8>.

[27] NOAA National Centers for Environmental Information. U.S. billion-dollar weather and climate disasters, 2025. URL <https://www.ncei.noaa.gov/access/billions/>.

[28] Sebin Oh, Sangri Yi, and Ziqi Wang. Long-range Ising model for regional-scale seismic risk analysis. *Earthquake Engineering & Structural Dynamics*, 53(12):3904–3923, 2024.

[29] Raul Rincon and Jamie Ellen Padgett. Fragility modeling practices and their implications on risk and resilience analysis: From the structure to the network scale. *Earthquake Spectra*, 40(1):647–673, February 2024. ISSN 8755-2930. doi: 10.1177/87552930231219220. URL <https://doi.org/10.1177/87552930231219220>. Publisher: SAGE Publications Ltd STM.

[30] Tom R. Robinson, Nicholas J. Rosser, Alexander L. Densmore, Katie J. Oven, Surya N. Shrestha, and Ramesh Guragain. Use of scenario ensembles for deriving seismic risk. *Proceedings of the Na-*

tional Academy of Sciences, 115(41), October 2018. ISSN 0027-8424, 1091-6490. doi: 10.1073/pnas.1807433115. URL <https://pnas.org/doi/full/10.1073/pnas.1807433115>.

[31] Nitheshnirmal Sadhasivam, Leonard Ohenen, Mohammad Khorrami, Susanna Werth, and Manoochehr Shirzaei. Building damage risk in sinking Indian megacities. *Nature Sustainability*, October 2025. ISSN 2398-9629. doi: 10.1038/s41893-025-01663-0. URL <https://www.nature.com/articles/s41893-025-01663-0>.

[32] Rafael M. Sebastianes and V. K. Saxena. Phase diagram of the random-field Ising model with a trimodal distribution. *Physical Review B*, 35(4):2058–2060, February 1987. ISSN 0163-1829. doi: 10.1103/PhysRevB.35.2058. URL <https://link.aps.org/doi/10.1103/PhysRevB.35.2058>.

[33] Mohamadreza Sheibani and Ge Ou. Accelerated Large-Scale Seismic Damage Simulation With a Bimodal Sampling Approach. *Frontiers in Built Environment*, 7:677560, May 2021. ISSN 2297-3362. doi: 10.3389/fbuil.2021.677560. URL <https://www.frontiersin.org/articles/10.3389/fbuil.2021.677560/full>.

[34] Theodorakis and Fytas. Random-field Ising model: Insight from zero-temperature simulations. *Condensed Matter Physics*, 17(4):43003, December 2014. ISSN 1607324X. doi: 10.5488/CMP.17.43003. URL <http://www.icmp.lviv.ua/journal/zbirnyk.80/43003/abstract.html>.

[35] Eric M. Thompson. An updated Vs30 map for California with geologic and topographic constraints (ver. 2.0, July 2022), 2018. URL <https://doi.org/10.5066/F7JQ108S>. U.S. Geological Survey data release.

[36] United Nations Office for the Coordination of Humanitarian Affairs (OCHA). Humanitarian transition overview: Türkiye earthquake response. Technical report, United Nations Office for the Coordination of Humanitarian Affairs (OCHA), August 2023. URL <https://reliefweb.int/report/turkiye/humanitarian-transition-overview-turkiye-earthquake-response-august-2023>.

[37] Dimitrios Vamvatsikos and C. Allin Cornell. Incremental dynamic analysis. *Earthquake Engineering & Structural Dynamics*, 31(3):491–514, March 2002. ISSN 0098-8847, 1096-9845. doi: 10.1002/eqe.141. URL <https://onlinelibrary.wiley.com/doi/10.1002/eqe.141>.

[38] John W. van de Lindt, Jamie Kruse, Daniel T. Cox, Paolo Gardoni, Jong Sung Lee, Jamie Padgett, Therese P. McAllister, Andre Barbosa, Harvey Cutler, Shannon Van Zandt, Nathanael Rosenheim,

Christopher M. Navarro, Elaina Sutley, and Sara Hamideh. The interdependent networked community resilience modeling environment (IN-CORE). *Resilient Cities and Structures*, 2(2):57–66, June 2023. ISSN 2772-7416. doi: 10.1016/j.rcns.2023.07.004. URL <https://www.sciencedirect.com/science/article/pii/S277274162300039X>.

[39] Alessandro Vespignani. The fragility of interdependency. *Nature*, 464(7291):984–985, April 2010. ISSN 0028-0836, 1476-4687. doi: 10.1038/464984a. URL <https://www.nature.com/articles/464984a>.

[40] Donald L. Wells and Kevin J. Coppersmith. New empirical relationships among magnitude, rupture length, rupture width, rupture area, and surface displacement. *Bulletin of the Seismological Society of America*, 84(4):974–1002, August 1994. ISSN 1943-3573, 0037-1106. doi: 10.1785/BSSA0840040974. URL <https://pubs.geoscienceworld.org/bssa/article/84/4/974/119792/New-empirical-relationships-among-magnitude>.

[41] World Bank and Global Facility for Disaster Reduction and Recovery. *Global Rapid Post-Disaster Damage Estimation (GRADE) Report: February 6, 2023 Kahramanmaraş Earthquakes - Türkiye Report*. Washington, DC, February 2023. doi: 10.1596/39468. URL <https://hdl.handle.net/10986/39468>.

[42] Mengjie Xiang, Jiaxu Shen, Zekun Xu, and Jun Chen. Structure-to-structure seismic damage correlation model. *Earthquake Engineering & Structural Dynamics*, 53(10):3205–3229, 2024. ISSN 1096-9845. doi: 10.1002/eqe.4172. URL <https://onlinelibrary.wiley.com/doi/abs/10.1002/eqe.4172>. _eprint: <https://onlinelibrary.wiley.com/doi/pdf/10.1002/eqe.4172>.

[43] Zekun Xu, Jun Chen, Jiaxu Shen, and Mengjie Xiang. Regional-scale nonlinear structural seismic response prediction by neural network. *Engineering Failure Analysis*, 154, December 2023. ISSN 13506307. doi: 10.1016/j.engfailanal.2023.107707. Publisher: Elsevier Ltd.

[44] Takahiro Yabe, P. Suresh C. Rao, Satish V. Ukkusuri, and Susan L. Cutter. Toward data-driven, dynamical complex systems approaches to disaster resilience. *Proceedings of the National Academy of Sciences*, 119(8):e2111997119, February 2022. ISSN 0027-8424, 1091-6490. doi: 10.1073/pnas.2111997119. URL <https://pnas.org/doi/full/10.1073/pnas.2111997119>.

[45] Tian You and Solomon Tesfamariam. Spatial correlation in building seismic performance for regional resilience assessment. *Resilient Cities and Structures*, 3(2):57–65, June 2024. ISSN 27727416. doi: 10.1016/j.rcns.2024.06.004. URL <https://linkinghub.elsevier.com/retrieve/pii/S2772741624000267>.

[46] Jian Zhong, Sien Zhou, Hao Wang, and Huimin Hu. Regional seismic fragility of bridge network derived by covariance matrix model of bridge portfolios. *Engineering Structures*, 309, June 2024. ISSN 18737323. doi: 10.1016/j.engstruct.2024.118035. Publisher: Elsevier Ltd.

[47] Minjie Zhu, Frank McKenna, and Michael H. Scott. OpenSeesPy: Python library for the OpenSees finite element framework. *SoftwareX*, 7:6–11, January 2018. ISSN 23527110. doi: 10.1016/j.softx.2017.10.009. URL <https://linkinghub.elsevier.com/retrieve/pii/S2352711017300584>.

[48] Adam Zsarnóczay, Wael Elhaddad, Barbaros Cetiner, Kuanshi Zhong, Frank McKenna, and Gregory Deierlein. SimCenter Earthquake Testbed: San Francisco, CA, 2023. URL <https://www.designsafe-ci.org/data/browser/public/designsafe.storage.published/PRJ-3880>.

[49] Adam Zsarnóczay, Gregory G. Deierlein, Frank McKenna, Matthew Schoettler, Sang-Ri Yi, Barbaros Cetiner, Aakash Bangalore Satish, Jinyan Zhao, Justin Bonus, Abiy F. Melaku, Sina Naeimi, Pedro Arduino, Rachel Davidson, Catherine Gorle, Sanjay Govindjee, Ahsan Kareem, Tracy L. Kijewski-Correa, Laura N. Lowes, Michael Motley, Seymour M. J. Spence, Ertugrul Taciroglu, Alexandros A. Taflanidis, and Matthew DeJong. An open-source simulation platform to support and foster research collaboration in natural hazards engineering. *Frontiers in Built Environment*, 11, August 2025. ISSN 2297-3362. doi: 10.3389/fbuil.2025.1590479. URL <https://www.frontiersin.org/journals/built-environment/articles/10.3389/fbuil.2025.1590479/full>. Publisher: Frontiers.

[50] Ádám Zsarnóczay and Gregory G. Deierlein. Pelicun – a computational framework for estimating damage, loss and community resilience. In *Proceedings of the 17th World Conference on Earthquake Engineering (17WCCEE)*, page Paper No. C003438, Sendai, Japan, September 13–18 2020. International Association for Earthquake Engineering, The 17th World Conference on Earthquake Engineering. URL <https://github.com/NHERI-SimCenter/pelicun>. © The 17th World Conference on Earthquake Engineering.

Acknowledgements

Data availability

The data that support the findings of this study are available in the paper and the Supplementary Information and/or from the corresponding author upon reasonable request.

Code availability

Code used to generate the results is available at [URL that will be available once the manuscript is accepted].

Author contributions

S.O. and Z.W. conceived and developed the core ideas. S.O., R.R., J.E.P., and Z.W. contributed to the study methodology. S.O. developed the software for the overall workflow and performed the simulations. J.Z. developed and executed the physics-based ground-motion time-history generation. S.O. curated the data, conducted the investigation, performed the formal analyses, and produced the visualizations. S.O. wrote the original manuscript. S.O., J.Z., R.R., J.E.P., and Z.W. reviewed and edited the manuscript. Z.W. supervised the project. R.R. provided baseline code for GMPE-based intensity-measure generation. Z.W. provided access to high-performance computing resources.

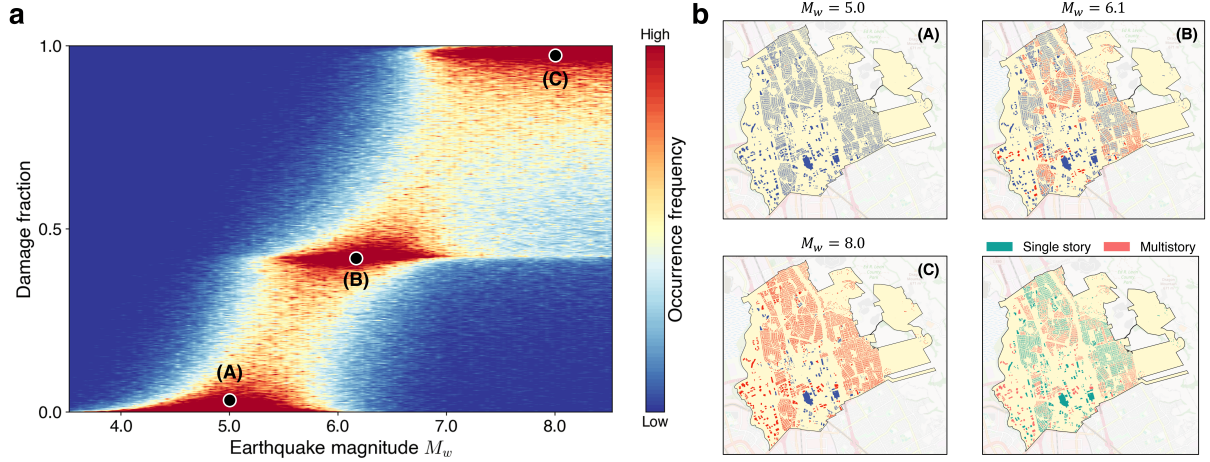
Competing interests

There are no competing interests to declare.

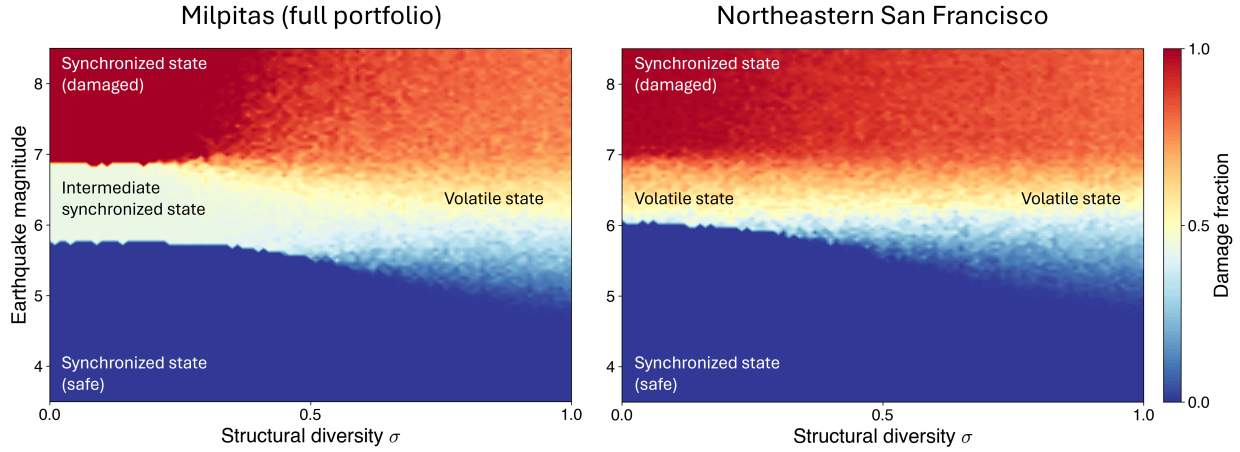
Additional information

Supplementary information is available for this paper. Correspondence and requests for materials should be addressed to Ziqi Wang.

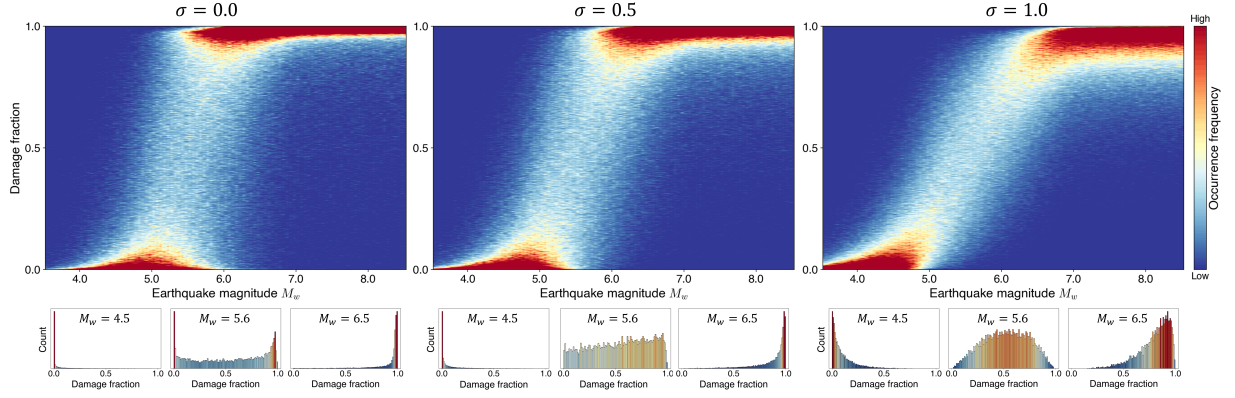
Extended Data



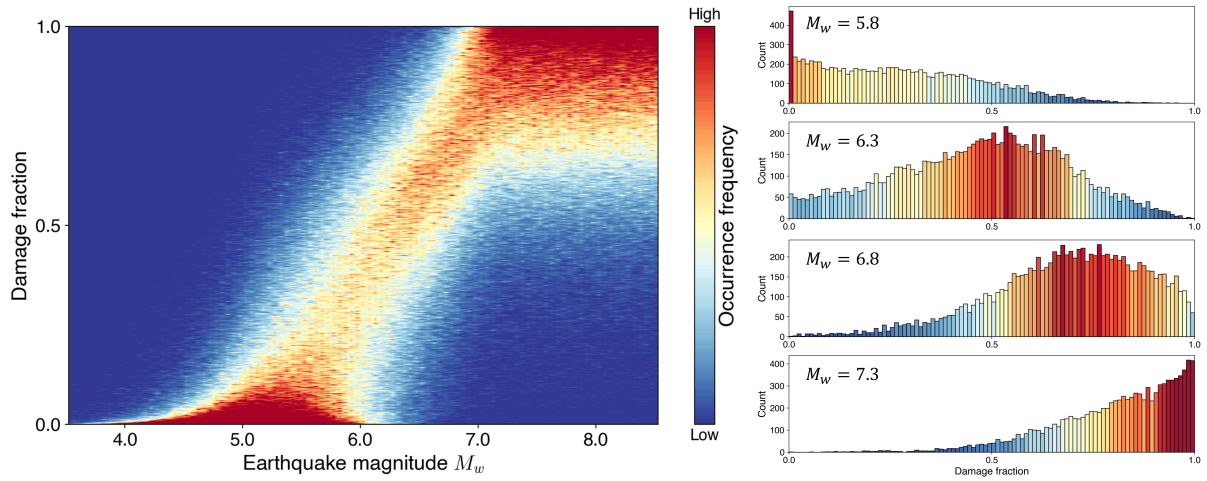
Extended Data Fig. 1: **Evolution of damage-fraction distributions with increasing earthquake magnitude for the full Milpitas portfolio.** **a**, Heatmap of regional damage-fraction distributions versus earthquake magnitude; colors indicate relative occurrence frequency. In Milpitas, the number of stories is nearly bimodal, whereas structural type is nearly uniform across the city (Extended Data Fig. 9). This bimodality gives rise to three collective states (A, B, and C) separated by two sequential transitions. **b**, Representative spatial damage maps for the three collective states, shown with the spatial distribution of the number of stories for reference. Blue and red indicate undamaged and damaged states, respectively. Damage in the intermediate state B aligns with multistory buildings, indicating collective damage of multistory structures. States A and C correspond to the collectively safe and collectively damaged states, respectively.



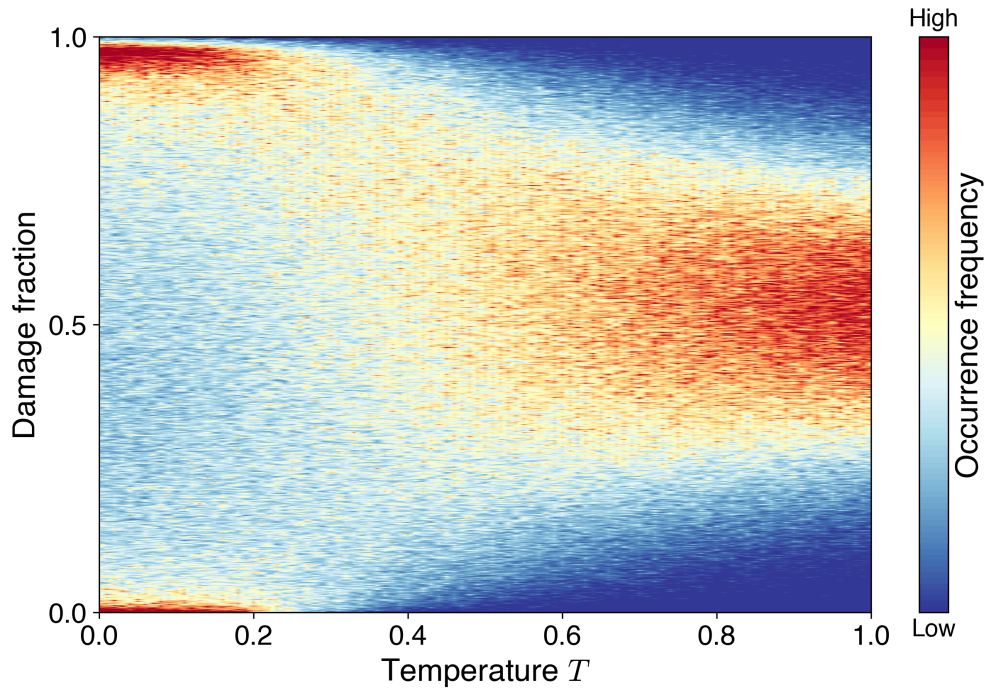
Extended Data Fig. 2: **Simulation-derived phase diagrams for the full Milpitas portfolio (left) and the northeastern San Francisco portfolio (right).** The full Milpitas portfolio exhibits three collective states at low structural diversity, consistent with the three-state behavior in Fig. 1. The San Francisco portfolio does not show a distinct transition boundary between the collectively safe and collectively damaged states; instead, the change is gradual, producing a smooth transition rather than a sharp phase boundary.



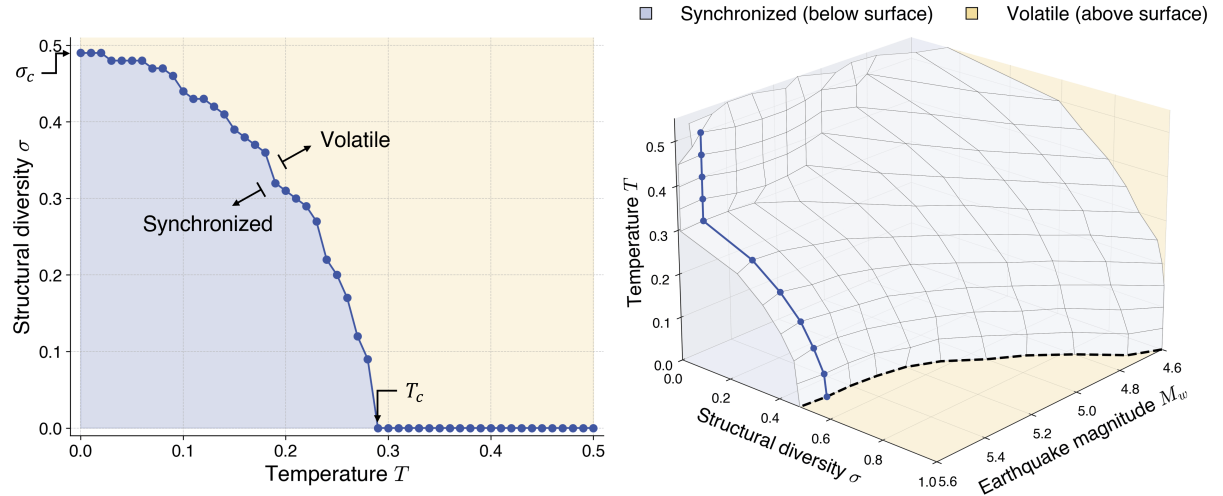
Extended Data Fig. 3: **Evolution of regional damage-fraction distributions at representative structural diversity levels.** Heatmaps show the evolution of the Milpitas damage-fraction distribution at three structural diversity levels ($\sigma = 0.0$, 0.5 , and 1.0). Snapshots below each panel show the corresponding histograms at representative magnitudes ($M_w = 4.5$, 5.6 , and 6.5). As structural diversity increases, the transition from the collectively safe to the collectively damaged state becomes progressively smoother, and the bimodality at intermediate magnitudes disappears.



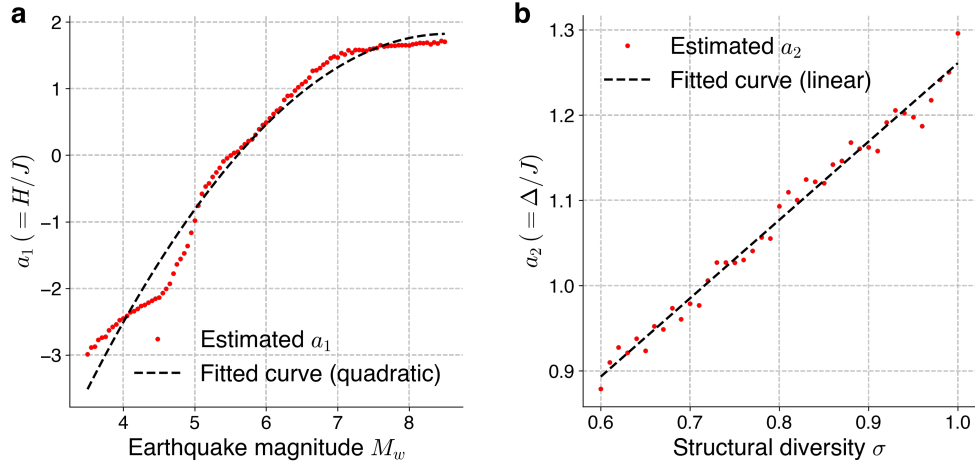
Extended Data Fig. 4: **Evolution of damage-fraction distributions with increasing earthquake magnitude for the northeastern San Francisco portfolio.** Heatmap (left) shows regional damage-fraction distributions versus earthquake magnitude, with the color indicating relative occurrence frequency. Histograms (right) show the distributions at selected magnitudes ($M_w = 5.8, 6.3, 6.8$, and 7.3), highlighting a smooth transition from the collectively safe to the collectively damaged state in this high-diversity portfolio.



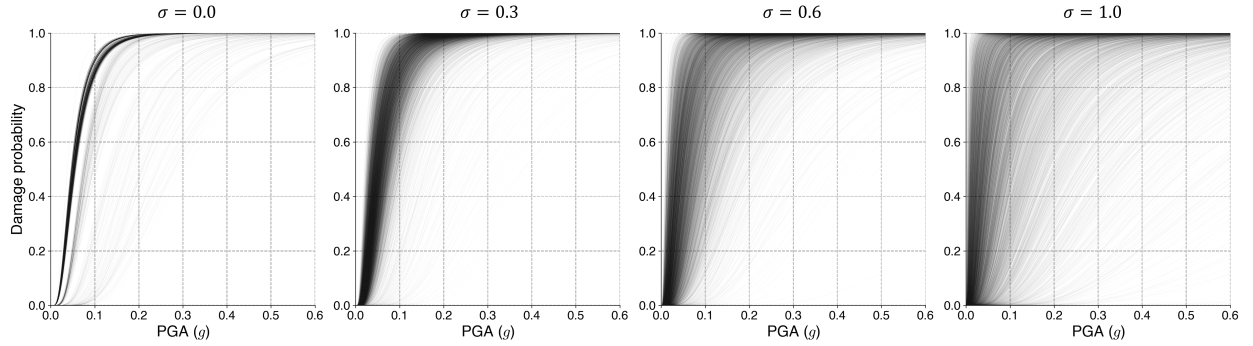
Extended Data Fig. 5: **Evolution of damage-fraction distribution with temperature in regional simulations.** Each column corresponds to a fixed earthquake magnitude, and each row to the probabilistic-margin parameter T . Increasing T progressively smooths the transition between the collectively safe and collectively damaged states, illustrating the analogy of temperature in the random-field Ising model to uncertainty in the hazard–structure interaction model; see Supplementary Method 2 for implementation details.



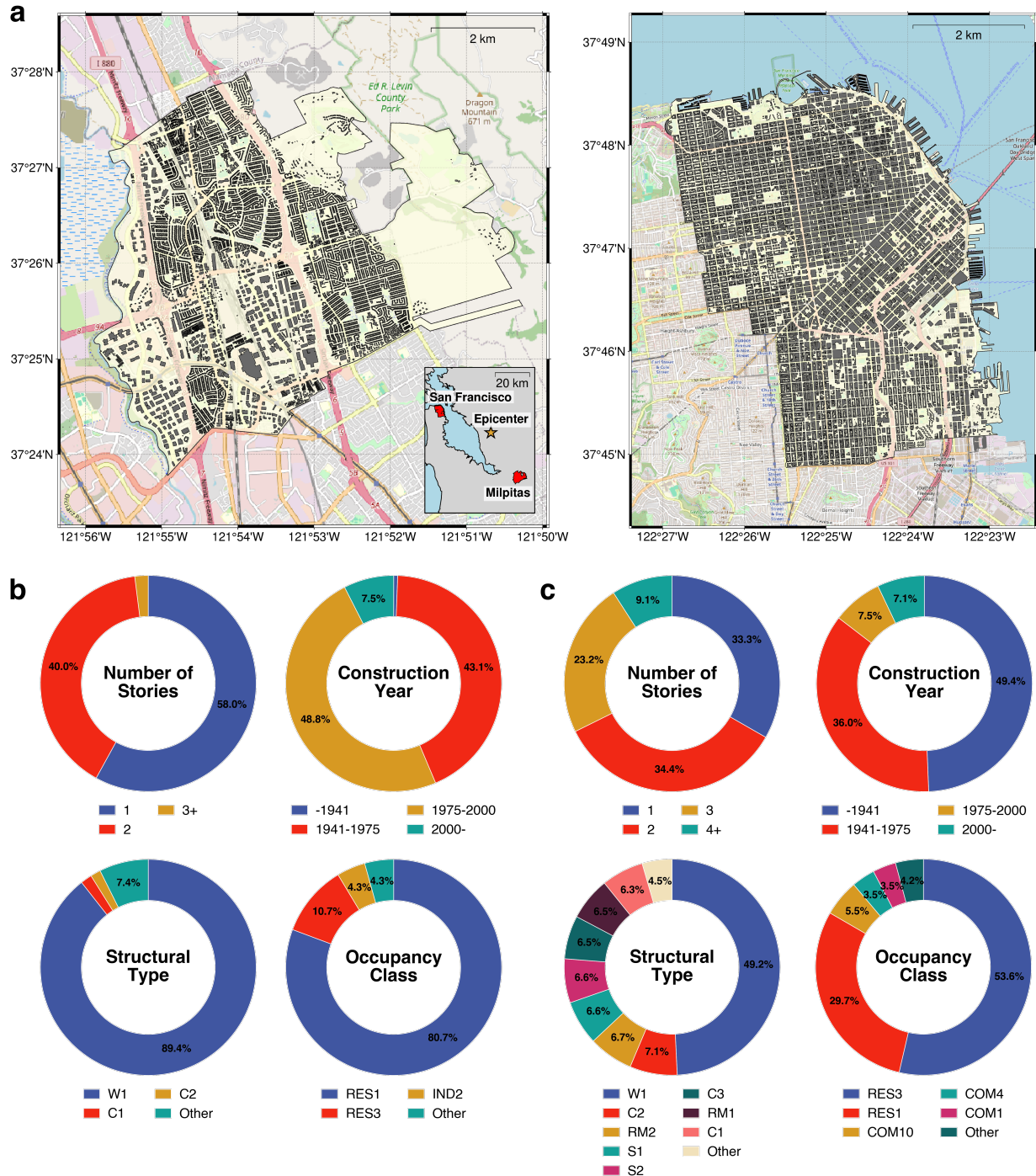
Extended Data Fig. 6: **Phase diagram for Milpitas, California, with temperature as a control parameter.** Collective behavior is shown in structural diversity–temperature space at $M_w = 5.5$ (left) and in structural diversity–temperature–magnitude space (right). The left panel shows the decrease in the critical diversity σ_c with increasing T , which marks the boundary between synchronized regimes (collectively safe or collectively damaged city-scale risk) and a volatile regime with mixed outcomes. The right panel extends this relationship across earthquake magnitudes M_w , yielding a continuous phase surface separating synchronized and volatile regions. Increasing T suppresses abrupt transitions, smoothing the boundary and weakening phase separation, consistent with the random-field Ising model [1, 32, 34]; see Supplementary Method 2 for implementation details.



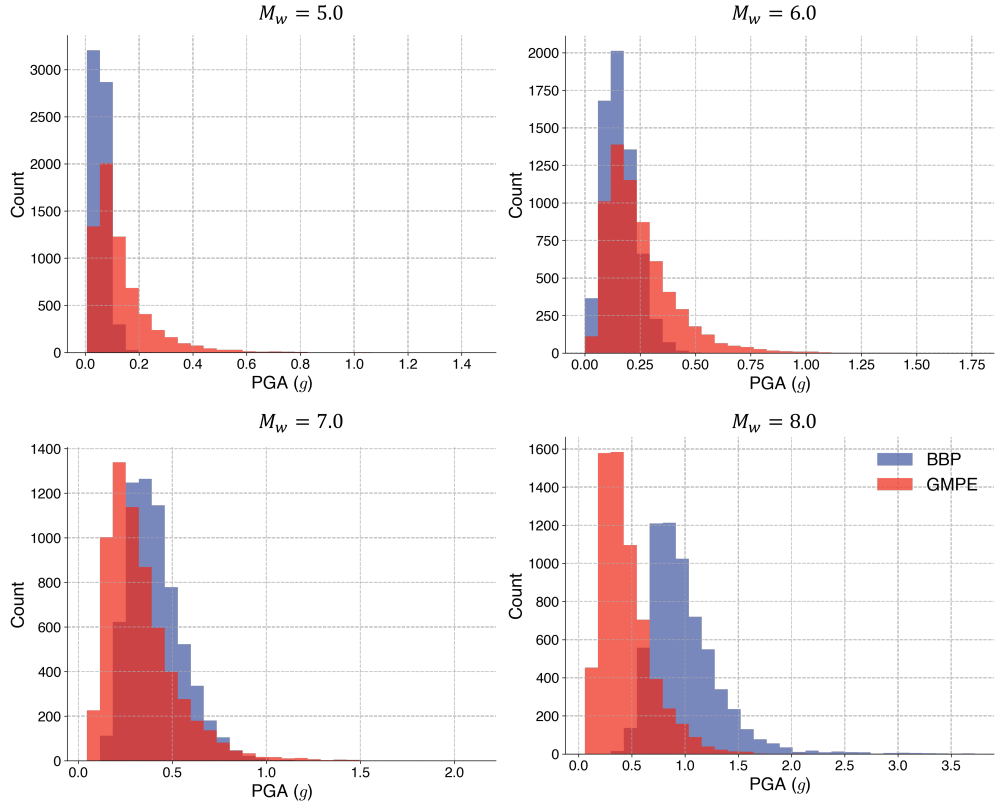
Extended Data Fig. 7: **Dependence of free-energy coefficients on hazard intensity and structural diversity.** **a**, First-order coefficient a_1 versus earthquake magnitude M_w , with a quadratic fit that crosses zero at the inferred critical magnitude. **b**, Second-order coefficient a_2 versus structural diversity σ , with a non-decreasing linear fit consistent with progressive smoothing of the transition as heterogeneity increases. To stabilize the fit and avoid spurious bistability, only data in the volatile regime ($\sigma > 0.6$) were used.



Extended Data Fig. 8: **Evolution of fragility curves with increasing structural diversity.** Fragility curves for the multistory building portfolio in Milpitas, California, shown for four structural diversity levels. Here, σ denotes the additional variability introduced to emulate cities with different levels of structural heterogeneity. $\sigma = 0.0$ corresponds to the baseline fragility-curve distribution estimated from incremental dynamic analysis (IDA) for Milpitas, with no added heterogeneity. g denotes gravitational acceleration.



Extended Data Fig. 9: **Regional building portfolios of Milpitas and San Francisco, California.** **a**, Building footprints of Milpitas (left) and northeastern San Francisco (right), with an inset map showing their relative locations and the earthquake epicenter. **b**, Composition of the Milpitas portfolio by number of stories, year built, structure type, and occupancy class, showing the dominance of low-rise residential buildings. **c**, Same distributions for San Francisco, revealing greater structural and functional diversity across the urban core. Categories for structural type and occupancy class follow Hazus 6.1 [11].



Extended Data Fig. 10: **Comparison of peak ground acceleration (PGA) distributions between physics-based and empirical models across four earthquake magnitudes.** Histograms show PGA from physics-based SCEC Broadband Platform (BBP) simulations and the empirical Chiou–Youngs ground-motion prediction equation (GMPE) [7]. PGA was sampled at 64 recording stations (the same for BBP and GMPE), uniformly distributed within Milpitas. For each method, 100 realizations were generated, yielding $64 \times 100 = 6,400$ samples per histogram. Supplementary Figs. 19–22 show the corresponding station-by-station spatial comparisons for the four magnitudes.

Supplementary Information for:
Phase Transitions in Collective Damage of Civil Structures
under Natural Hazards

Sebin Oh^a, Jinyan Zhao^b, Raul Rincon^c, Jamie Padgett^c, Ziqi Wang^{a,*}

^a*Department of Civil and Environmental Engineering, University of California, Berkeley, CA, United States of America*

^b*Department of Mechanical and Civil Engineering, California Institute of Technology, Pasadena, CA, United States of America*

^c*Department of Civil and Environmental Engineering, Rice University, Houston, TX, United States of America*

This PDF file includes:

Supplementary Note 1

Supplementary Methods 1–6

Supplementary Figs. 1–22

References

*Corresponding author
Email address: zqiwang@berkeley.edu(Ziqi Wang)

Table of Contents

Supplementary Notes	40
Supplementary Note 1. Probabilistic simulations in regional-scale risk analysis	40
Supplementary Methods	41
Supplementary Method 1. Order parameter identification using principal component analysis	41
Supplementary Method 2. Non-zero temperature simulation	43
Supplementary Method 3. Ising model revisited	44
Supplementary Method 4. Ensemble-based estimation of susceptibility, correlations, and data-driven Landau free energy	48
Supplementary Method 5. Simulation framework for regional-scale structural responses	50
Supplementary Method 6. Implementation of regional-scale structural simulations	51
Supplementary Figures	55
Supplementary Fig. 1. Sensitivity analysis: kernel density estimation (KDE)-based fragility curves	55
Supplementary Fig. 2. Sensitivity analysis: empirical ground-motion prediction equations (GMPEs)	56
Supplementary Fig. 3. Sensitivity analysis: the North Berkeley building portfolio	57
Supplementary Fig. 4. Sensitivity analysis: the Belmont building portfolio	58
Supplementary Fig. 5. Explained-variance spectra from principal component analysis (PCA) . . .	59
Supplementary Fig. 6. Equivalence between the first principal component and the regional damage fraction	60
Supplementary Fig. 7. Evolution of the projected PCA space with increasing earthquake magnitude for Milpitas	61
Supplementary Fig. 8. Evolution of the projected PCA space with increasing earthquake magnitude for northeastern San Francisco	62
Supplementary Fig. 9. Evolution of the projected PCA space with increasing structural diversity for Milpitas	63
Supplementary Fig. 10. Evolution of the projected PCA space with increasing structural diversity for northeastern San Francisco	64
Supplementary Fig. 11. Data-driven Landau free-energy landscape	65

Supplementary Fig. 12. Equilibrium magnetization and susceptibility from the data-driven Landau free-energy landscape	66
Supplementary Fig. 13. Mean and quantile values of regional repair-cost distributions computed with and without engineering simplifications	67
Supplementary Fig. 14. Exceedance probabilities for two reference repair costs	68
Supplementary Fig. 15. Distributions of building attributes for the Milpitas portfolio	69
Supplementary Fig. 16. Selected neighborhoods in northeastern San Francisco	70
Supplementary Fig. 17. Distributions of building attributes for the northeastern San Francisco portfolio	71
Supplementary Fig. 18. Maps of the near-surface shear-wave velocity V_{s30} for Milpitas (left) and northeastern San Francisco (right)	72
Supplementary Fig. 19. Comparison of peak ground acceleration (PGA) distributions between physics-based and empirical models at $M_w = 5.0$ across recording stations	73
Supplementary Fig. 20. Comparison of peak ground acceleration (PGA) distributions between physics-based and empirical models at $M_w = 6.0$ across recording stations	74
Supplementary Fig. 21. Comparison of peak ground acceleration (PGA) distributions between physics-based and empirical models at $M_w = 7.0$ across recording stations	75
Supplementary Fig. 22. Comparison of peak ground acceleration (PGA) distributions between physics-based and empirical models at $M_w = 8.0$ across recording stations	76
Supplementary References	77

Supplementary Notes

Supplementary Note 1. Probabilistic simulations in regional-scale risk analysis

Regional-scale risk analysis to natural hazards fundamentally depends on probabilistic simulations. It is infeasible to directly observe or experimentally reproduce the full-scale response of an entire city to a natural hazard. Field surveys and post-disaster reconnaissance provide only limited, one-shot data point that represents a single realization of complex stochastic processes. To overcome this scarcity of empirical observations, probabilistic simulations serve as an essential tool for exploring the range of possible regional civil structural responses, quantifying uncertainties, and identifying emergent behaviors that cannot be captured from individual events alone. Such simulations enable researchers to represent the inherent randomness in both hazard excitations and structural capacities, forming the foundation for assessing collective risk at the city or regional scale.

Supplementary Methods

Supplementary Method 1. Order parameter identification using principal component analysis

Recent studies have demonstrated that unsupervised machine learning techniques can uncover the underlying order parameters of complex systems directly from empirical data, without prior physical assumptions [7, 14, 26]. While adopting the regional damage fraction as an order parameter follows naturally from the analogy between the RFIM and regional simulations, we further verify that this order parameter can be recovered directly from the data itself, without presuming its form.

To this end, we employ principal component analysis (PCA) as a minimally parametric approach to extract low-dimensional collective modes from ensembles of simulation outcomes. The analyses are conducted for two study regions (Milpitas and northeastern San Francisco) under two distinct simulation scenarios. In the first-order scenario, the earthquake magnitude M_w is varied while structural diversity is fixed at $\sigma = 0$ (no additional heterogeneity). In the second-order scenario, the structural diversity σ is varied while the magnitude is fixed at the critical value $M_w = M_{w_c}$ defined as the magnitude at which the average damage fraction equals 0.5. This design yields four analysis cases in total, one for each combination of region and scenario. For each case, PCA is applied to ensembles of realizations sampled across the corresponding control parameter (M_w for the first-order and σ for the second-order scenario).

The resulting explained-variance spectra are shown in Supplementary Fig. 5. In all cases, the first principal component dominates the total variance, particularly for the first-order scenarios where the system response is governed by a single collective mode representing the abrupt transition between the safe and damaged states. For the second-order scenarios, the variance explained by the first component is relatively lower, reflecting the distributed, continuous reorganization of the system across a broad range of structural diversity. The explained variance for the San Francisco cases is generally smaller than that of Milpitas, indicating the weak inter-building dependence in the San Francisco region that renders the regional damage-fraction distribution approximately Gaussian.

The equivalence between the first principal component (PC1) and the regional damage fraction is demonstrated in Supplementary Fig. 6. Across all four analysis cases, PC1 exhibits a nearly one-to-one correspondence with the damage fraction, confirming that the dominant collective mode identified purely from the data coincides with the physically interpretable order parameter of the system. This alignment validates that the macroscopic organization of regional responses can be fully captured by a single scalar quantity, consistent with the analogy between magnetization in the random-field Ising model and the regional damage

fraction in city-scale simulations.

The visual evolution of ensembles projected onto the PC1–PC2 space is presented in Supplementary Figs. 7–10. Under the first-order scenario (varying M_w at $\sigma = 0$), the Milpitas case exhibits an abrupt shift of the distribution along PC1 around $M_w \approx 5.60$, marking a discontinuous transition from the collectively safe to the collectively damaged state. In contrast, the San Francisco case follows a smooth trajectory without a sudden jump, indicating the absence of a sharp first-order transition. Under the second-order scenario (varying σ at fixed $M_w = M_{w_c}$), Milpitas shows a gradual merging of distributions along PC1, consistent with continuous, second-order-like behavior. The San Francisco case, by contrast, shows no fundamental reorganization across increasing σ , confirming that the region is already in a disordered, paramagnetic-like phase. Together, these PCA projections provide direct visual evidence that the nature of collective regional response transitions is governed by the external excitation intensity and by the strength of inter-building coupling.

Supplementary Method 2. Non-zero temperature simulation

Regional simulations described in the main text correspond to a zero-temperature RFIM. In this setting, the safety margin $M = C - D$, where C and D denotes structural capacity and hazard demand, respectively, fully determines the damage state: if $M < 0$, the structure is classified as damaged; otherwise, it is safe. This deterministic assignment leaves no margin for uncertainty, equivalent to the zero-temperature limit where thermal fluctuations are absent.

We further examine the effect of allowing a *probabilistic margin* to the safety margin. From the perspective of the RFIM–regional simulation analogy, the safety margin M can be regarded as the negative energy difference between the damaged and safe states: $M \propto -\Delta E = -(E_{\text{damaged}} - E_{\text{safe}})$. Maximizing the entropy under this constraint yields the damage probability

$$\mathbb{P}(\text{Damage}) = \frac{1}{1 + \exp(M/T)},$$

where T denotes the probabilistic-margin parameter. This logistic form follows from the principle of maximum entropy. Constraining only the expected energy with an energy gap ΔE (equivalently $M \propto -\Delta E$), the maximum-entropy distribution for the binary damage is the Boltzmann distribution, which yields the logistic damage probability. As $T \rightarrow 0$, the decision rule becomes fully deterministic, while larger T introduce increasing uncertainty around the failure threshold. In the regional simulation context, T represents the epistemic uncertainty or the degree of confidence in the hazard-structure model.

Spatially averaged damage fraction in the magnitude–temperature space is shown in Extended Data Fig. 5, revealing the progressive smoothing of the collective response as temperature increases. Interestingly, the critical structural diversity σ_c , beyond which the region no longer exhibits a first-order-like abrupt transition, varies systematically with temperature, as illustrated in Extended Data Fig. 6.

We observe that σ_c decreases as temperature increases. This suggests that large uncertainty in the hazard–structure model systematically obscures the emergence of collective behavior, smoothing out the distinct phases observed at lower uncertainty levels. Maintaining a consistent phase across analyses therefore becomes crucial for meaningful risk assessment. Conversely, pursuing excessively precise component-level models or datasets may yield limited returns for system-level decision-making, as microscopic refinements are often averaged out when collective dynamics dominate.

Supplementary Method 3. Ising model revisited

The classical Ising model

The Ising model provides a fundamental framework for describing collective behavior that arises from interactions among many coupled components. In its general form, the system consists of N discrete sites that interact with one another, each represented by a spin variable $s_i \in \{-1, +1\}$ corresponding to one of two possible states. The total energy of a given configuration is expressed by the Hamiltonian

$$\mathcal{H} = - \sum_{i < j} J_{ij} s_i s_j - H \sum_i s_i,$$

where J_{ij} denotes the coupling strength between sites i and j , and H is an external field acting uniformly on all sites. The first term captures the tendency of neighboring spins to align when $J_{ij} > 0$, while the second term biases the spins toward the direction of the external field. The balance between these two contributions determines the overall alignment of the system.

At thermal equilibrium, the probability of observing a particular configuration $\{s_i\}$ follows the Boltzmann distribution,

$$p(\{s_i\}) = \frac{1}{Z} \exp(-\beta \mathcal{H}),$$

where $\beta = 1/(k_B T)$ is the inverse temperature, k_B is the Boltzmann constant, T is the absolute temperature, and Z is the partition function that ensures normalization. The macroscopic state of the system is characterized by the equilibrium magnetization

$$m^* \equiv \langle m \rangle = \frac{1}{N} \sum_{i=1}^N \langle s_i \rangle,$$

where $\langle s_i \rangle$ denotes the thermal expectation value of spin s_i . This quantity serves as the order parameter, distinguishing different phases and capturing critical behavior. When the temperature T is high, thermal fluctuations dominate and the spins are randomly oriented, leading to $m \approx 0$ (a disordered phase). Below a critical temperature T_c , the system spontaneously breaks symmetry and develops a nonzero magnetization ($m = \pm m_0$, with $m_0 > 0$), indicating an ordered phase in which most spins align in the same direction. This spontaneous symmetry breaking represents a continuous (second-order) phase transition, providing a minimal mathematical representation of how local interactions can give rise to abrupt macroscopic organization.

Random-field Ising model (RFIM)

The RFIM extends the classical Ising framework by introducing spatial disorder through site-dependent local fields. The Hamiltonian of the RFIM is expressed as

$$\mathcal{H} = - \sum_{i < j} J_{ij} s_i s_j - \sum_i (H + h_i) s_i,$$

where H represents the uniform external field and h_i denotes the local deviation from H at site i . The disorder in the random field h_i is quenched, meaning that the local fields are frozen in each realization and remain fixed during thermal averaging. The random fields $\{h_i\}$ are typically drawn from a Gaussian distribution, $h_i \sim \mathcal{N}(0, \Delta^2)$, where Δ characterizes the strength of disorder. The first term in \mathcal{H} captures the pairwise coupling between sites, while the second term introduces local heterogeneity that competes with the global ordering tendency.

The interplay between the coupling J_{ij} and disorder amplitude Δ governs the collective behavior of the system. For small Δ , the spins remain strongly correlated, and the system exhibits an abrupt transition between ordered and disordered states as the external field H varies. In contrast, large Δ suppresses long-range correlations, leading to a smooth evolution of the macroscopic magnetization. This transition from discontinuous to continuous behavior reflects the shift from a second-order phase transition as disorder increases.

The RFIM thus provides a foundational framework for systems in which local variability modulates global organization. In the context of regional-scale structural responses to natural hazards, the disorder strength Δ represents the degree of heterogeneity in building capacities or subsurface and meteorological conditions, whereas J_{ij} characterizes the effective interaction between structures subjected to correlated hazard excitation. This analogy enables a statistical-physics interpretation of regional risk dynamics through the lens of critical phenomena.

Mean-field approximation and zero-temperature limit of RFIM

To obtain a tractable analytical description of the system's macroscopic behavior, we employ the mean-field approximation, which replaces explicit pairwise interactions with an average coupling to the mean magnetization. In this framework, spatial variations are neglected and the interaction coefficients are replaced by a uniform coupling, $J_{ij} = \frac{J}{N}$. Each spin therefore experiences an effective field $h_i^{\text{eff}} = Jm + H + h_i$, combining the mean-field contribution Jm , the external field H , and the local random perturbation h_i .

At zero temperature, thermal fluctuations vanish, and the state of each spin is determined deterministically by the sign of its local effective field:

$$s_i = \text{sign}(Jm + H + h_i).$$

The ensemble-averaged magnetization is then obtained as

$$\langle m \rangle = \frac{1}{N} \sum_{i=1}^N \langle s_i \rangle = \int_{-\infty}^{\infty} \text{sign}(Jm + H + h) \phi(h) dh,$$

where $\phi(h) = \frac{1}{\sqrt{2\pi\Delta}} \exp\left(-\frac{h^2}{2\Delta^2}\right)$ is the Gaussian distribution of the random field. Exploiting the symmetry of $\phi(h)$, we obtain the self-consistency condition for the magnetization

$$\begin{aligned} m &= \mathbb{P}(Jm + H + h > 0) - \mathbb{P}(Jm + H + h < 0) \\ &= 2\Phi\left(\frac{Jm + H}{\Delta}\right) - 1 \\ &= \text{erf}\left(\frac{Jm + H}{\sqrt{2}\Delta}\right), \end{aligned} \tag{3}$$

where $\Phi(\cdot)$ is the cumulative distribution function of the standard normal random variable. Equation (3) thus defines the equilibrium magnetization $m^* \equiv \langle m \rangle$ as the fixed point of the mean-field map.

Landau free-energy formulation

The equilibrium states of the mean-field RFIM can be characterized by a phenomenological Landau free-energy potential $F_{\text{MF}}(m)$, whose stationary points reproduce the self-consistent condition in Eq. (3). We define its gradient with respect to the order parameter m as

$$\frac{\partial F_{\text{MF}}}{\partial m} = m - \text{erf}\left(\frac{Jm + H}{\sqrt{2}\Delta}\right),$$

so that $\partial F_{\text{MF}}/\partial m = 0$ recovers Eq. (3). Integrating with respect to m yields, up to an additive constant C ,

$$\begin{aligned} F_{\text{MF}}(m; H, \Delta) &= \frac{1}{2}m^2 - \int \text{erf}\left(\frac{Jm + H}{\sqrt{2}\Delta}\right) dm + C \\ &= \frac{1}{2}m^2 - \left(m + \frac{H}{J}\right) \text{erf}\left(\frac{Jm + H}{\sqrt{2}\Delta}\right) - \sqrt{\frac{2}{\pi}} \frac{\Delta}{J} \exp\left(-\frac{(Jm + H)^2}{2\Delta^2}\right) + C. \end{aligned}$$

The shape of $F_{\text{MF}}(m; H, \Delta)$ provides an intuitive picture of how disorder alters collective behavior. For

weak disorder ($\Delta \ll J$), the free-energy landscape exhibits two symmetric minima separated by a barrier, corresponding to bistable ordered states with $m = \pm m_0$. As Δ increases, the barrier gradually flattens and the two minima merge into a single well centered at $m = 0$, exhibiting the disappearance of bistability and the onset of a continuous transition. The evolution of $F_{\text{MF}}(m)$ thus provides an intuitive picture of how local heterogeneity smooths out collective order, linking the microscopic disorder strength to the macroscopic transition type.

In the context of regional-scale structural risk analysis, this free-energy landscape represents the effective potential governing the collective damage state of the built environment. The emergence of bistable minima corresponds to regimes where the region exhibits two distinct macroscopic states, i.e., collectively safe and collectively damaged, while the single well regime reflects a continuous response transition without abrupt shifts in collective condition.

Supplementary Method 4. Ensemble-based estimation of susceptibility, correlations, and data-driven Landau free energy

To quantify collective sensitivity and spatial coherence, we compute the susceptibility χ and the connected two-point correlation function $C(r)$ from the equilibrium ensemble at fixed (M_w, σ) for a fixed portfolio realization (i.e., a fixed set of fragility curves). We repeat the calculation for 50 independent portfolio realizations, all at the same σ , to quantify realization-to-realization variability and obtain robust distributions of χ and ξ .

Equilibrium ensemble selection

We select the narrowest interval of the damage fraction m_d , $[m_{d_{lo}}, m_{d_{hi}}]$, that contains a fixed fraction f of the samples (we use $f = 0.10$, i.e., 1,000 of 10,000). Samples with $m_d \in [m_{d_{lo}}, m_{d_{hi}}]$ form the equilibrium ensemble used to compute the ensemble average $\langle \cdot \rangle$ for χ and $C(r)$.

Connected correlations

For each site $i = 1, \dots, N$, we record $s_i \in \{-1, +1\}$ across $R = 10,000$ realizations $\alpha = 1, \dots, R$ at fixed (M_w, σ) . Ensemble averages are taken over realizations:

$$\langle s_i \rangle = \frac{1}{R} \sum_{\alpha=1}^R s_i^{(\alpha)}, \quad \langle s_i s_j \rangle = \frac{1}{R} \sum_{\alpha=1}^R s_i^{(\alpha)} s_j^{(\alpha)}.$$

The connected correlation is

$$C(i, j) = \langle s_i s_j \rangle - \langle s_i \rangle \langle s_j \rangle.$$

To obtain a distance-dependent correlation, we compute pairwise Euclidean distances $r_{ij} = \|\mathbf{x}_i - \mathbf{x}_j\|$ and radially average $C(i, j)$ over all distinct pairs $i < j$ whose distances fall in bins $[r, r + \Delta r)$, yielding $C(r)$.

We normalize by the on-site variance,

$$C(0) = \frac{1}{N} \sum_{i=1}^N \left(\langle s_i^2 \rangle - \langle s_i \rangle^2 \right) = \frac{1}{N} \sum_{i=1}^N (1 - \langle s_i \rangle^2),$$

and report $C(r)/C(0)$. Correlation lengths ξ are estimated by fitting $C(r)/C(0) \propto e^{-r/\xi}$ over the range shown in Fig. 2e (using only bins with positive $C(r)$).

Susceptibility estimation from a polynomial-fit Landau free energy

Susceptibility can also be expressed in terms of the free-energy curvature as $\chi^{-1} = \frac{\partial^2 F}{\partial m^2} \Big|_{m=m^*}$, where m^* is the equilibrium order parameter. Here we estimate χ from an empirical free-energy landscape reconstructed from the simulated distribution of the regional order parameter m_d .

For each (M_w, σ) , we form the empirical distribution $P(m)$ from a histogram of the damage fraction, mapped to $m \in [-1, 1]$. Up to an additive constant, we define the empirical Landau free energy as

$$F_{\text{emp}}(m) = -\ln P(m),$$

where a small additive offset is applied to $P(m)$ to avoid $\ln 0$ in empty bins.

We then construct a polynomial-fit free energy $F_{\text{poly}}(m)$ by fitting $F_{\text{emp}}(m)$ with a polynomial Landau form,

$$F_{\text{poly}}(m) = c_0 + c_1 m + c_2 m^2 + c_4 m^4 + c_k m^k,$$

where $k \geq 6$ is an even integer. The linear term $c_1 m$ captures weak asymmetry in the empirical landscape, while the high-order stabilizing term $c_k m^k$ enforces boundedness near $|m| \rightarrow 1$ without materially affecting the fit around the minimum (i.e., the equilibrium). We impose $c_k > 0$ and fix $k = 100$, which yields stable fits and prevents spurious minima near the bounds (Supplementary Fig. 11).

From the fitted landscape, the equilibrium magnetization m^* is obtained by the stationary condition $F'_{\text{poly}}(m^*) = 0$. The susceptibility is then estimated from the inverse curvature at the equilibrium magnetization,

$$\chi^{-1} = \frac{\partial^2 F_{\text{poly}}}{\partial m^2} \Big|_{m=m^*}.$$

This curvature-based definition is consistent with the mean-field linear-response relation $\chi = \partial \langle m \rangle / \partial h$, and provides a robust, quantitative measure of collective sensitivity from a finite ensemble. Supplementary Fig. 12 shows the estimated equilibrium order parameter m^* and susceptibility χ for three representative values of σ .

Supplementary Method 5. Simulation framework for regional-scale structural responses

For a region consisting of n structures, consider a *safety margin* (or *safety factor*) vector $\mathbf{X} \in \mathbb{R}^n$, where each element X_i denotes the safety margin of structure i . The damage state of each structure is determined based on its safety margin. For instance, if a binary damage state is of interest, the damage state DS_i of structure i is defined as

$$DS_i = \begin{cases} 1, & \text{if } X_i \leq 0 \\ 0, & \text{if } X_i > 0, \end{cases}$$

where DS_i indicates whether structure i has damaged ($DS_i = 1$) or not ($DS_i = 0$). To capture the uncertainties inherent in hazard events and structural responses, each safety margin X_i is modeled as a random variable. The failure probability of structure i , denoted by P_{f_i} , is then given by

$$P_{f_i} = \mathbb{P}(X_i \leq 0),$$

which depends on the probability distribution of X_i . Since our interest lies in the collective behavior of multiple structures, the *joint* probability distribution of the vector \mathbf{X} becomes central. In other words, regional-scale risk analyses and simulations focus on characterizing the joint distribution of \mathbf{X} , including its mean vector, covariance matrix, and distribution type. This perspective encompasses both stochastic and physics-based approaches, where the resulting distribution may not belong to any standard family of probability distributions. In such cases, the distribution can be developed through repeated simulations under varying sources of uncertainty.

In structural engineering practices, the first- and the second-order central and cross moments of \mathbf{X} are often available; the reliability of individual structures typically needs to be assessed during the design phase, which requires the mean and variance of the safety margin. Many methods can be used to calculate the first- and the second-order central moments, including full-size experiments to high-fidelity finite element analyses with accurate physical parameters, while the inter-building correlation has recently begun to gain attention [13, 16, 28–30]. Oh et al. [22] presented an unbiased approach for constructing a joint probability distribution of \mathbf{X} based on the principle of maximum entropy, given that the first- and second-order central moments are known.

Supplementary Method 6. Implementation of regional-scale structural simulations

Regional data retrieval

All data used in this study were obtained from publicly accessible repositories and open-source libraries to ensure reproducibility. The datasets encompass building inventories, ground-motion records, and administrative boundaries, which together form the basis of the regional simulations.

Building-level attributes were retrieved from the *NHERI SimCenter Earthquake Testbed for the San Francisco Bay Area* [21]. The database provides detailed information on the number of stories, construction year, structural type, occupancy class, plan area, repair cost, and replacement cost for more than 200,000 buildings in the region. Two subsets were used in this study: (1) the city of Milpitas, including 5,943 multi-story buildings, and (2) the northeastern districts of San Francisco, comprising 6,323 buildings across mixed structural types. The data were accessed through the DesignSafe DataDepot (PRJ-3880 [32]) and formatted as geospatial layers to enable spatial mapping and structural model generation.

A total of 100 empirical ground-motion acceleration records were obtained from the *Enhancement of Next Generation Attenuation Relationships for Western US* (NGA-West2) database [2, 6]. The NGA-West2 database provides a comprehensive collection of uniformly processed strong-motion records from shallow-crustal earthquakes in active tectonic regions. The retrieved 100 time-history records were used to perform incremental dynamic analyses for estimating structural capacities. These motions represent crustal earthquakes recorded in California and were scaled to varying intensity levels following the procedure described in the [Methods](#).

City boundaries and building footprints were generated using the open-source *OSMnx* library [4] with base map data from OpenStreetMap [23]. Neighborhood boundaries for San Francisco were obtained from the *Analysis Neighborhoods* dataset on the San Francisco Open Data Portal [11]. All retrieved polygons were projected to the EPSG:3857 coordinate system and used to clip and visualize the regional building portfolios.

Structural capacity modeling

We adopt the peak inter-story drift ratio (IDR) as the engineering demand parameter (EDP). For each structural type and design era, the *Hazus Earthquake Model Technical Manual* (Version 6.1; FEMA, 2024) defines threshold drift ratios at which a building is considered to have reached the slight-damage state [12]. Building capacity is defined as the ground-motion intensity measure (IM) at which the model first reaches

this slight-damage EDP under record scaling. The peak ground acceleration (PGA) is adopted as the intensity measure, expressed in units of g , the gravitational acceleration.

Following the baseline approach of Lu et al. [18], as adopted in the SimCenter R2D Tool [21], we developed a multi-degree-of-freedom (MDOF) shear model for each building using the Hazus 6.1 tabulations [12], characterized by fundamental building attributes such as the number of stories, structural material, construction year, and plan area. Each model is a planar system with one lateral degree of freedom per story (rigid diaphragm action at floor levels). Story response is represented by zero-length elements with a uniaxial hysteretic material capturing yielding, cyclic degradation, and pinching. Models are implemented in OpenSeesPy [20, 31].

Incremental dynamic analyses (IDA) [25] were performed with 100 empirical NGA-West2 ground-motion records. Each record was scaled until the structure reached its slight-damage drift-ratio limit, producing one threshold IM (here, PGA) per record. The resulting 100 threshold PGAs per building constitute a capacity sample in terms of PGA, from which the building-level fragility curve is derived.

The IDA-derived capacity samples were converted into probabilistic models at the building level to propagate uncertainty in regional simulations. In the main text, we employ a parametric lognormal model; in the Supplementary Information, we also report a non-parametric alternative to assess sensitivity to distributional assumptions.

In earthquake engineering practice, building-level fragility curves are most commonly modeled as lognormal, and this convention is adopted widely in guidelines and applications (e.g., Hazus 6.1 [12]; FEMA P-58 [3]). Accordingly, for each building i with structural capacity C_i , we model $\ln C_i \sim \mathcal{N}(\mu_i, \sigma_i^2)$ with (μ_i, σ_i) calibrated from the 100 samples. The resulting fragility (probability of damage at a given IM) is

$$\mathbb{P}(\text{Damage} \geq \text{Slight} \mid \text{IM}) = \Phi\left(\frac{\ln \text{IM} - \mu_i}{\sigma_i}\right),$$

where Φ is the standard normal cumulative distribution function (CDF).

To evaluate the impact of distributional assumptions, we also construct building-level fragility curves directly from the capacity samples using Gaussian kernel density estimation (KDE) on $\ln C$, without imposing a parametric form. The KDE-based density is numerically integrated to obtain a CDF, which represents the individual fragility curves for buildings [9, 19]. Supplementary Figs. 1 present the resulting fragility curves and the corresponding regional simulation outcomes.

We preserve inter-building dependence between structural capacities by estimating regional correlations

from the ensemble of 100 IDA-based capacity samples and retaining this correlation structure when sampling capacities for regional analyses. This captures common-source variability arising from shared structural attributes. For the KDE-based fragility curves, we employ a Gaussian copula to impose the same correlation matrix on the non-parametric marginals, ensuring that both the parametric and non-parametric formulations maintain consistent inter-building dependence in regional simulations.

Hazard demand modeling

We adopt the peak ground acceleration (PGA) as the ground-motion intensity measure at each building location, representing the maximum horizontal acceleration experienced during an earthquake. For each earthquake scenario, spatial PGA fields are computed using empirical ground-motion prediction equations (GMPEs) based on predefined earthquake scenarios that are physically plausible for the study regions. To ensure both statistical realism and physical consistency with regional seismotectonic conditions, physics-based ground-motion simulations are also performed for selected scenarios to cross-validate the PGA fields derived from the GMPEs.

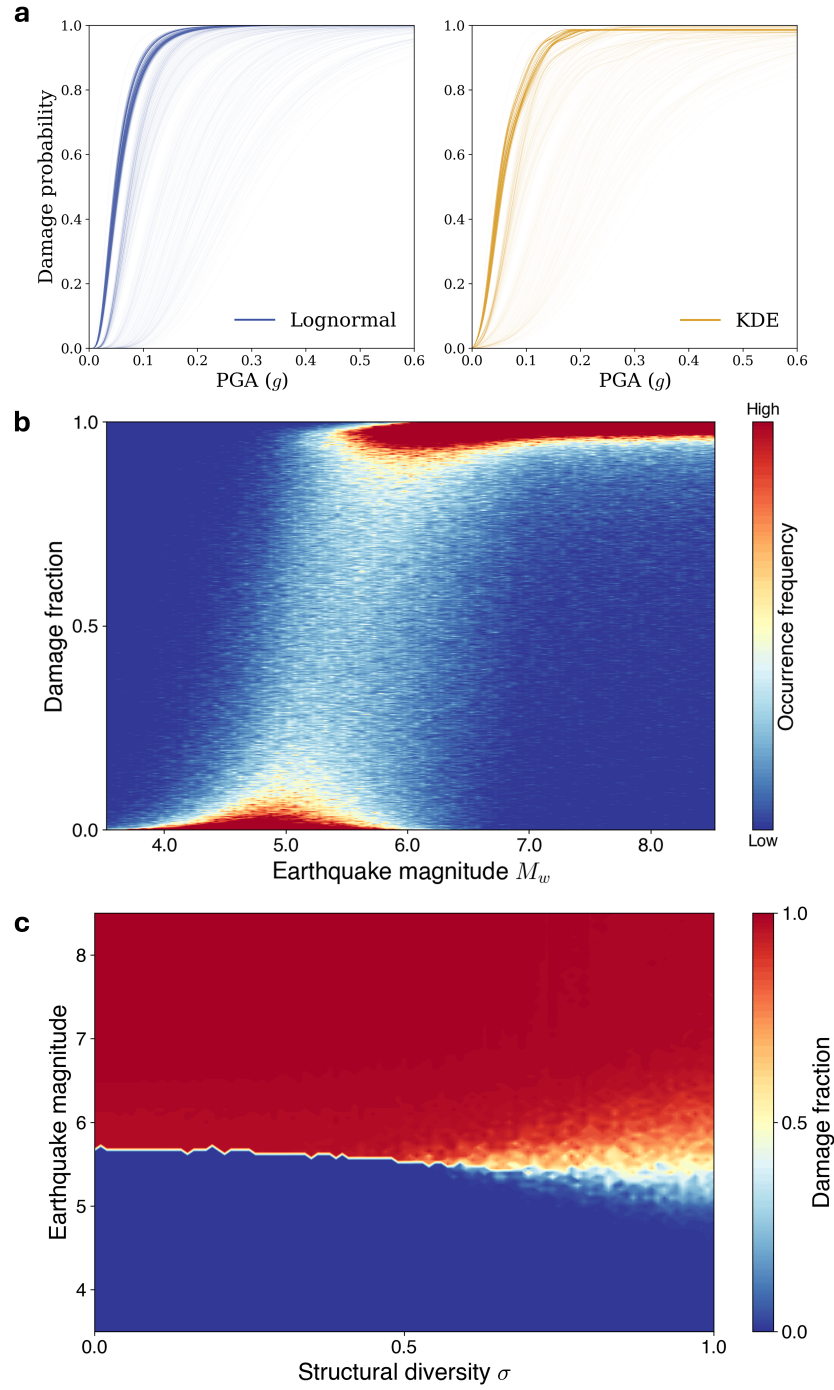
The earthquake scenarios were defined by varying the moment magnitude M_w from 3.5 to 8.5 in increments of 0.05, in which reliability of the adopted GMPEs is ensured, covering the sufficient range from small to large regional events. All scenarios share a common epicenter located at latitude 37.666° N and longitude 122.076° W, approximately along the central segment of the Hayward fault, which poses one of the most significant seismic threats to the San Francisco Bay Area. Since the Hayward fault is a right-lateral strike-slip fault, the fault geometry is defined by a strike of 325°, dip of 90°, and rake of 180°, representing a near-vertical, right-lateral strike-slip mechanism typical of the Hayward fault system. The depth to the top of the rupture plane is set to 3 km, consistent with empirical observations of shallow crustal earthquakes in California. These configurations ensure that the generated ground-motion fields are both realistic and representative of the dominant regional seismotectonic conditions.

For each scenario, we compute spatial fields of the logarithmic PGA mean and standard deviation at every building location using the *Enhancement of Next Generation Attenuation Relationships for Western U.S.* (NGA-West2) GMPE of Chiou and Youngs [10] (CY14). The selected GMPE is implemented through the `pygmm` Python library [17]. The rupture geometry defined above is employed, while the V_{s30} value at each location is retrieved from Thompson [24] (Supplementary Fig. 18) and the rupture length L and width W are estimated from the moment magnitude M_w using the empirical regressions of Wells and Coppersmith [27]. Spatial correlation of intra-event residuals was modeled following Jayaram et al. [15] with an exponential decay function, ensuring realistic spatial variability in ground-motion intensity.

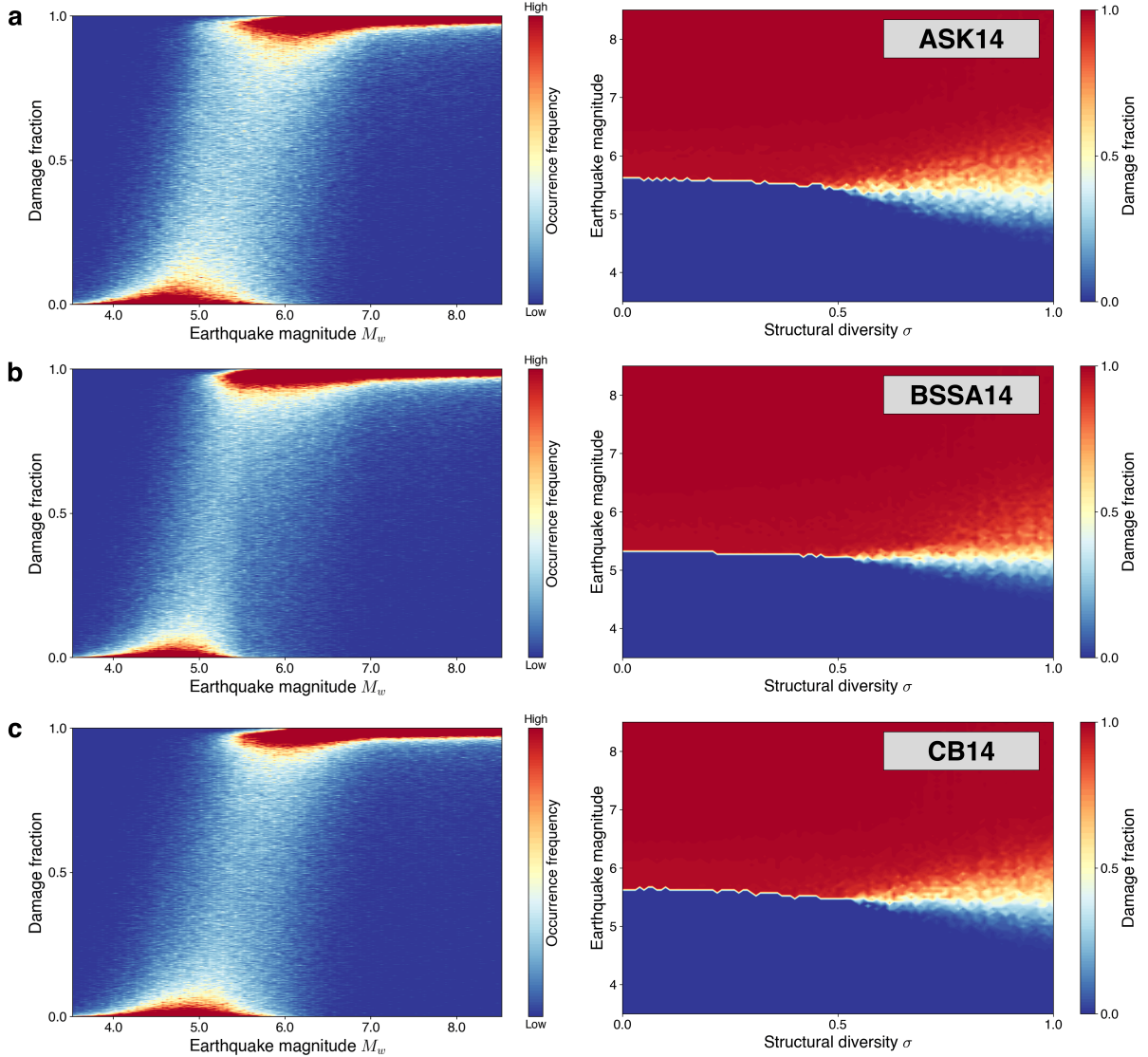
Different empirical GMPEs are applied to the benchmark Milpitas example, including the Abrahamson–Silva–Kamai 2014 (ASK14) GMPE [1], the Boore–Stewart–Seyhan–Atkinson 2014 (BSSA14) GMPE [5], and the Campbell–Bozorgnia 2014 (CB14) GMPE [8], all of which are suitable for active tectonic regions such as California. Supplementary Figs. 2 present the sensitivity analysis comparing the regional simulation outcomes obtained using these different GMPEs.

To complement the empirical models, we employ the *Southern California Earthquake Center Broadband Platform* (SCEC-BBP) to simulate three-dimensional broadband ground motions. For the same earthquake scenarios and input parameters used in the GMPE analyses, time histories are generated on an 8 grid (64 recording stations) within the study region, and the corresponding PGA values are extracted. These simulations capture long-period basin effects and rupture directivity patterns that empirical models cannot represent. The simulated and GMPE-based PGA maps are cross-validated to confirm the realism of the generated ground-motion intensity fields, which are presented in Extended Data Fig. 10 and Supplementary Figs. 19 to 22.

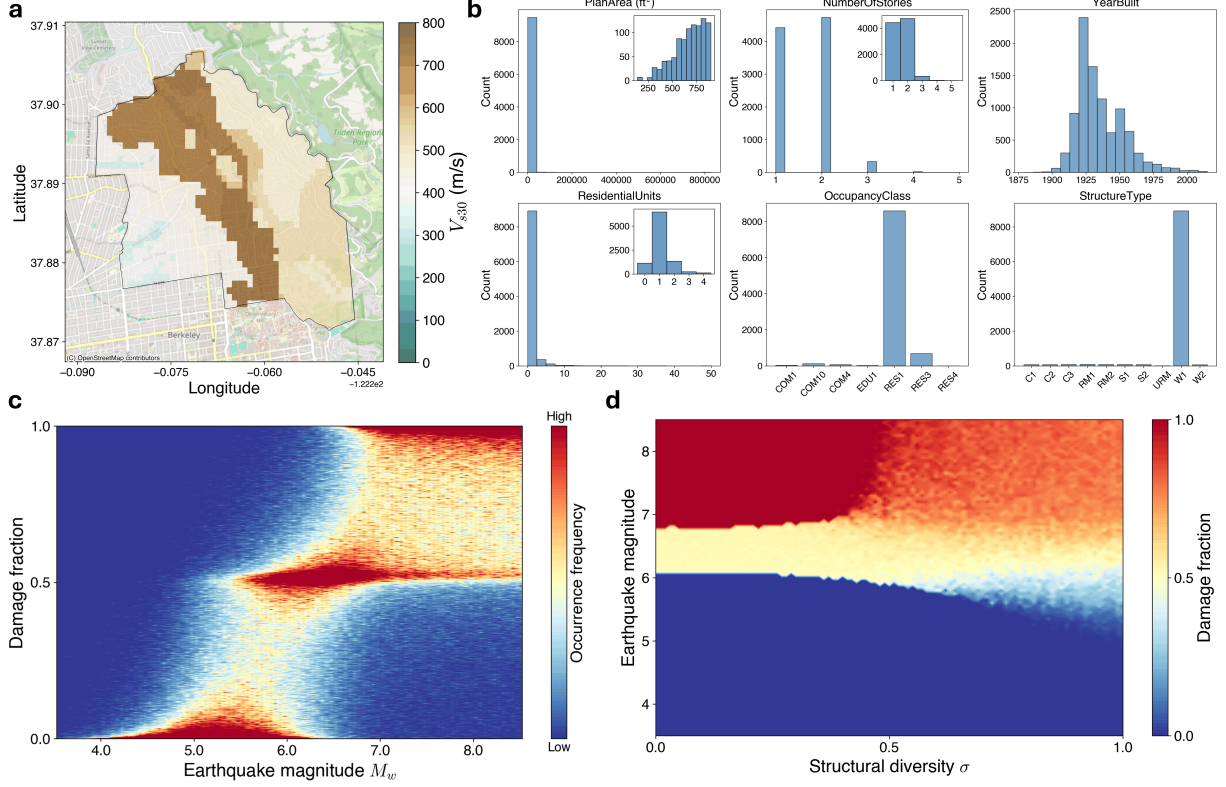
Supplementary Figures



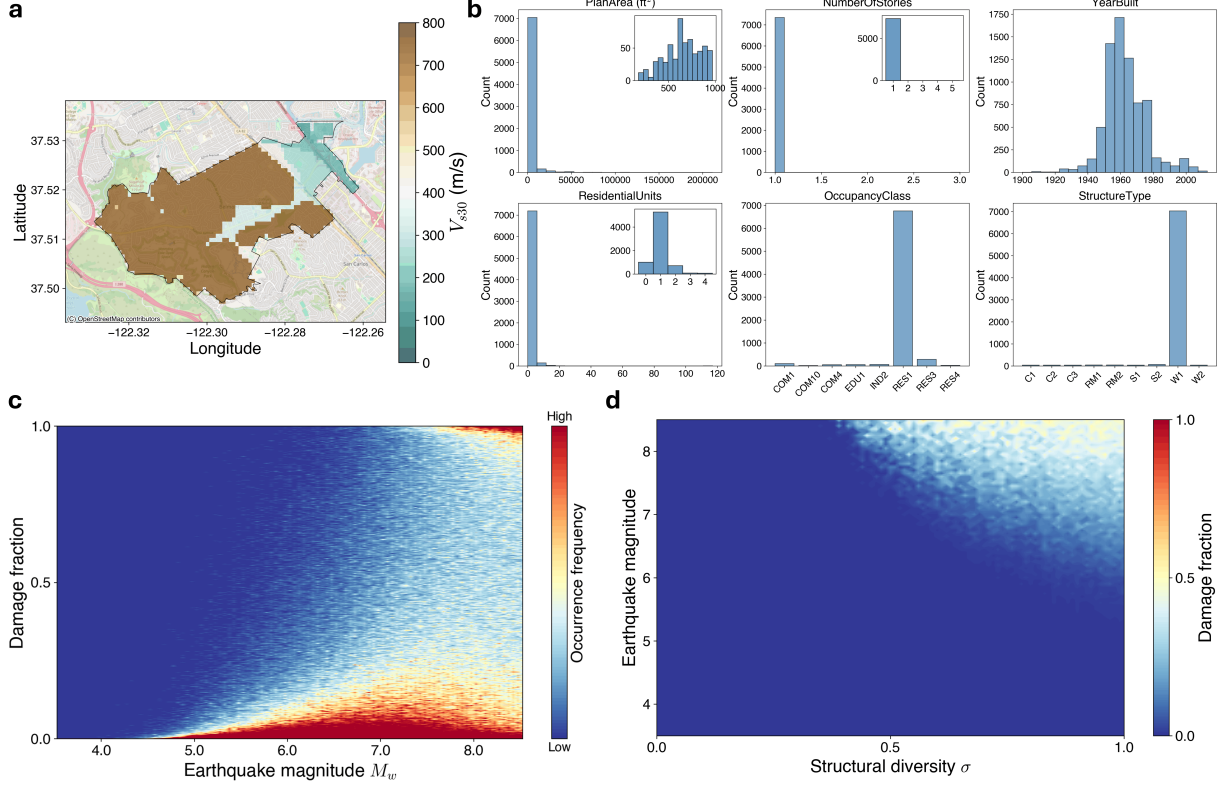
Supplementary Fig. 1: **Sensitivity analysis: kernel density estimation (KDE)-based fragility curves.** **a**, Comparison of fragility curves for the Milpitas portfolio constructed using the conventional lognormal form (left) and the KDE-based non-parametric form (right). **b**, Evolution of regional damage-fraction distributions with increasing earthquake magnitude when the KDE-based fragility curves are used. **c**, Empirical phase diagram of the Milpitas portfolio obtained using the KDE-based fragility curves. It preserves the key features of the phase diagram shown in Fig. 2b of the main text, which is constructed using lognormal fragility curves.



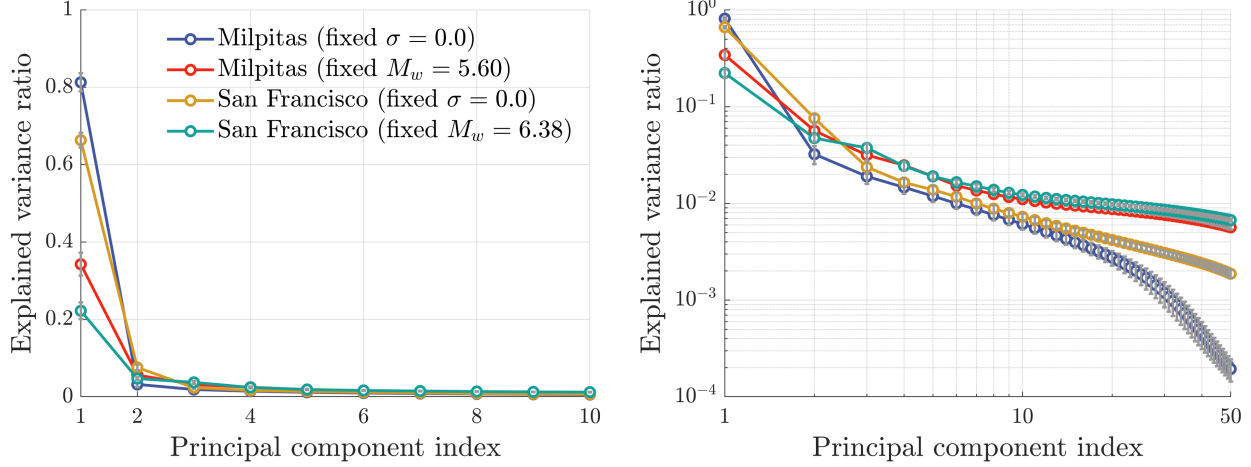
Supplementary Fig. 2: **Sensitivity analysis: empirical ground-motion prediction equations (GMPEs).** The benchmark Milpitas portfolio is evaluated using three NGA-West2 GMPEs. For each model, the evolution of regional damage-fraction distributions with earthquake magnitude (left) and the corresponding empirical phase diagram (right) are shown. **a**, Abrahamson–Silva–Kamai 2014 (ASK14) [1]. **b**, Boore–Stewart–Seyhan–Atkinson 2014 (BSSA14) [5]. **c**, Campbell–Bozorgnia 2014 (CB14) [8]. All three preserve the key features of the phase diagram in Fig. 2b of the main text, which is constructed using the Chiou–Youngs 2014 (CY14) model [10].



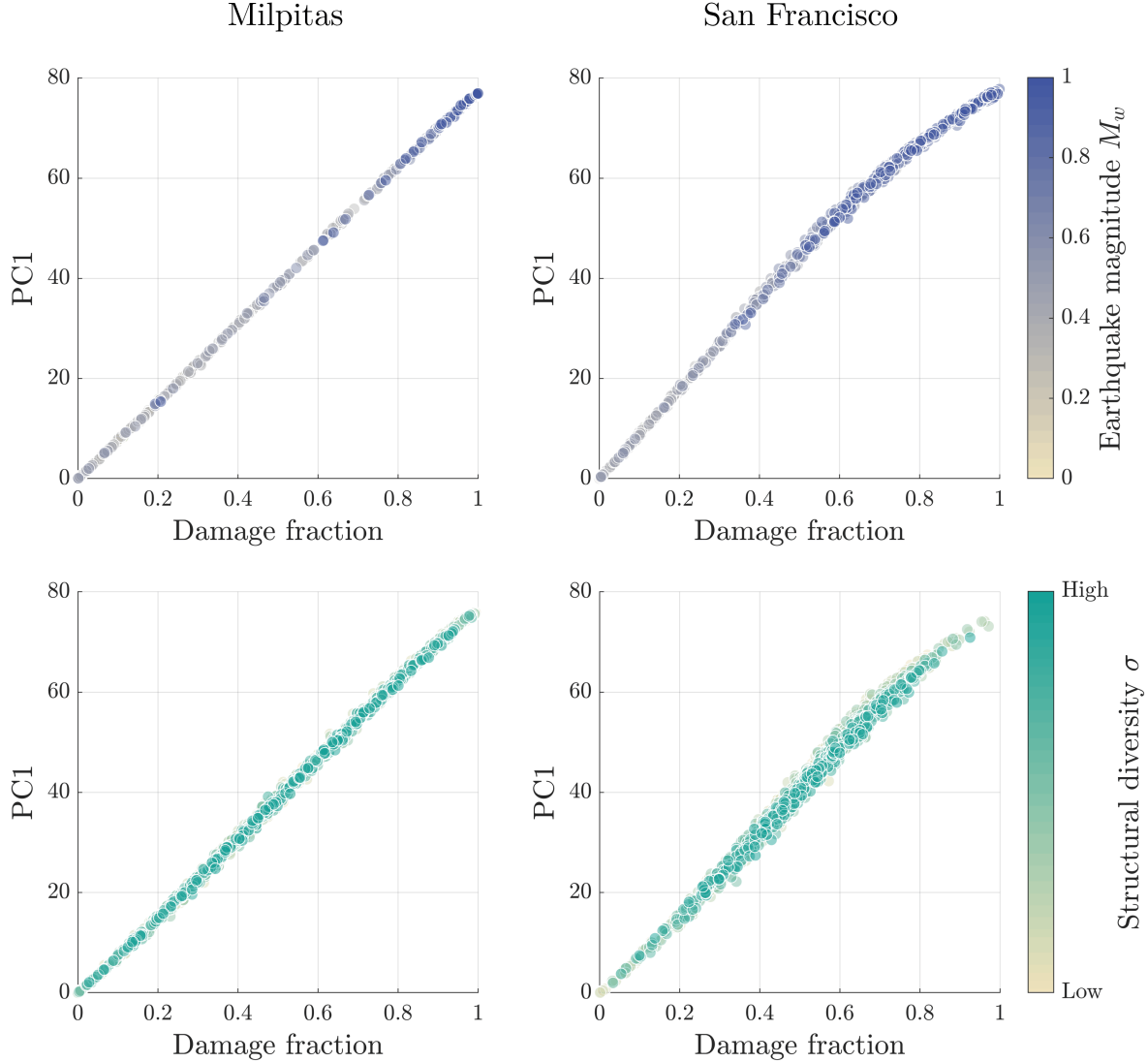
Supplementary Fig. 3: **Sensitivity analysis: the North Berkeley building portfolio.** **a**, Map of the near-surface shear-wave velocity V_{s30} across the North Berkeley region. **b**, Distributions of key building attributes, including plan area, number of stories, construction year, residential units, occupancy class, and structural type. **c**, Evolution of regional damage-fraction distributions with increasing earthquake magnitude for the North Berkeley portfolio. **d**, Empirical phase diagram showing the collective structural response as a function of structural diversity σ and earthquake magnitude. Since the numbers of single-story and multi-story buildings are comparable, while other factors that strongly influence seismic response are relatively uniform across the region, the North Berkeley portfolio exhibits three collective states with two transition boundaries.



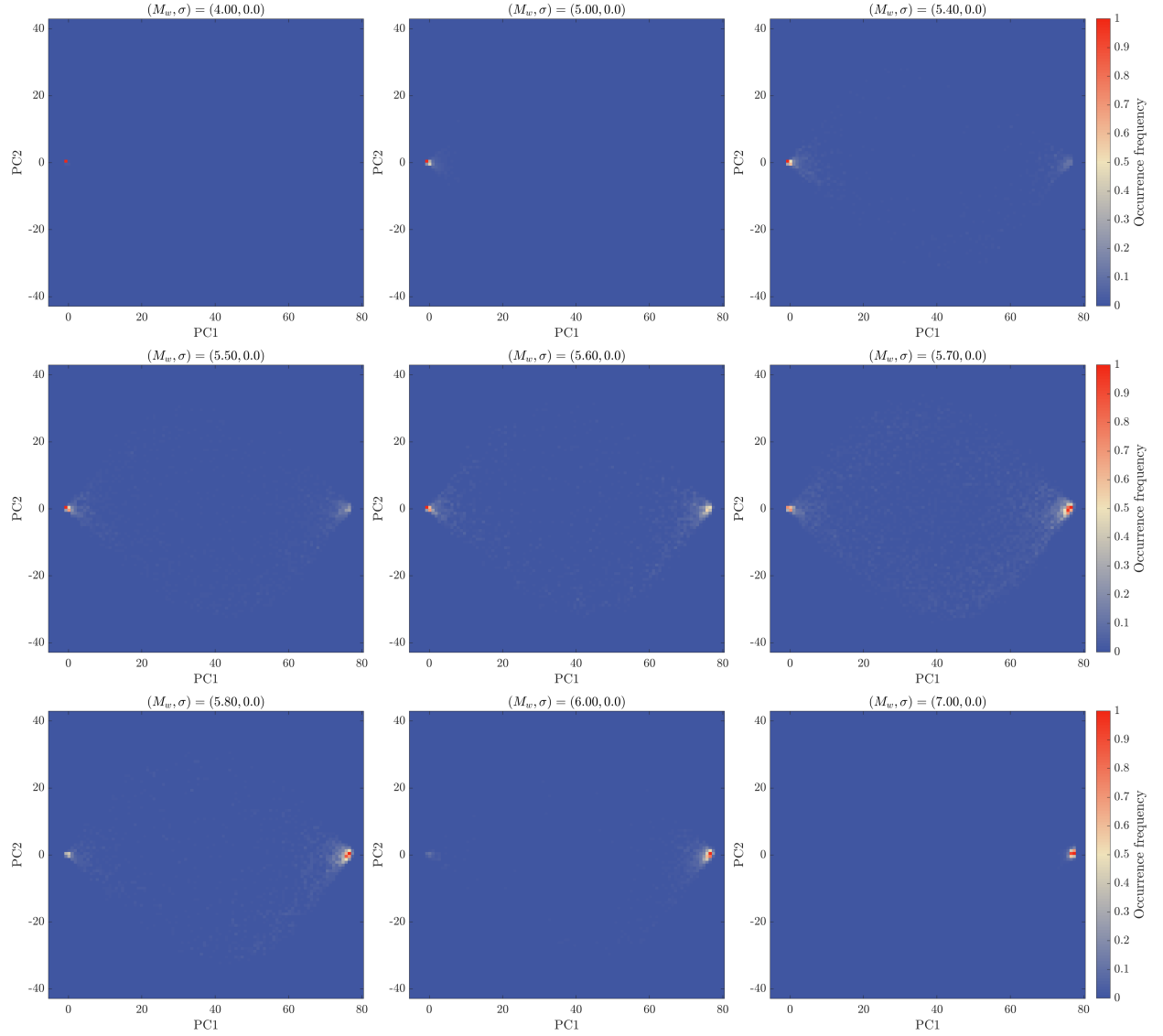
Supplementary Fig. 4: **Sensitivity analysis: the Belmont building portfolio.** **a**, Map of the near-surface shear-wave velocity V_{s30} across the Belmont region. **b**, Distributions of key building attributes, including plan area, number of stories, construction year, residential units, occupancy class, and structural type. **c**, Evolution of regional damage-fraction distributions with increasing earthquake magnitude for the Belmont portfolio. **d**, Empirical phase diagram showing the collective structural response as a function of structural diversity σ and earthquake magnitude. Due to the single-story-dominant building portfolio and the high V_{s30} values across the region, Belmont shows little transition behavior and remains predominantly in the collectively safe state throughout the examined parameter range.



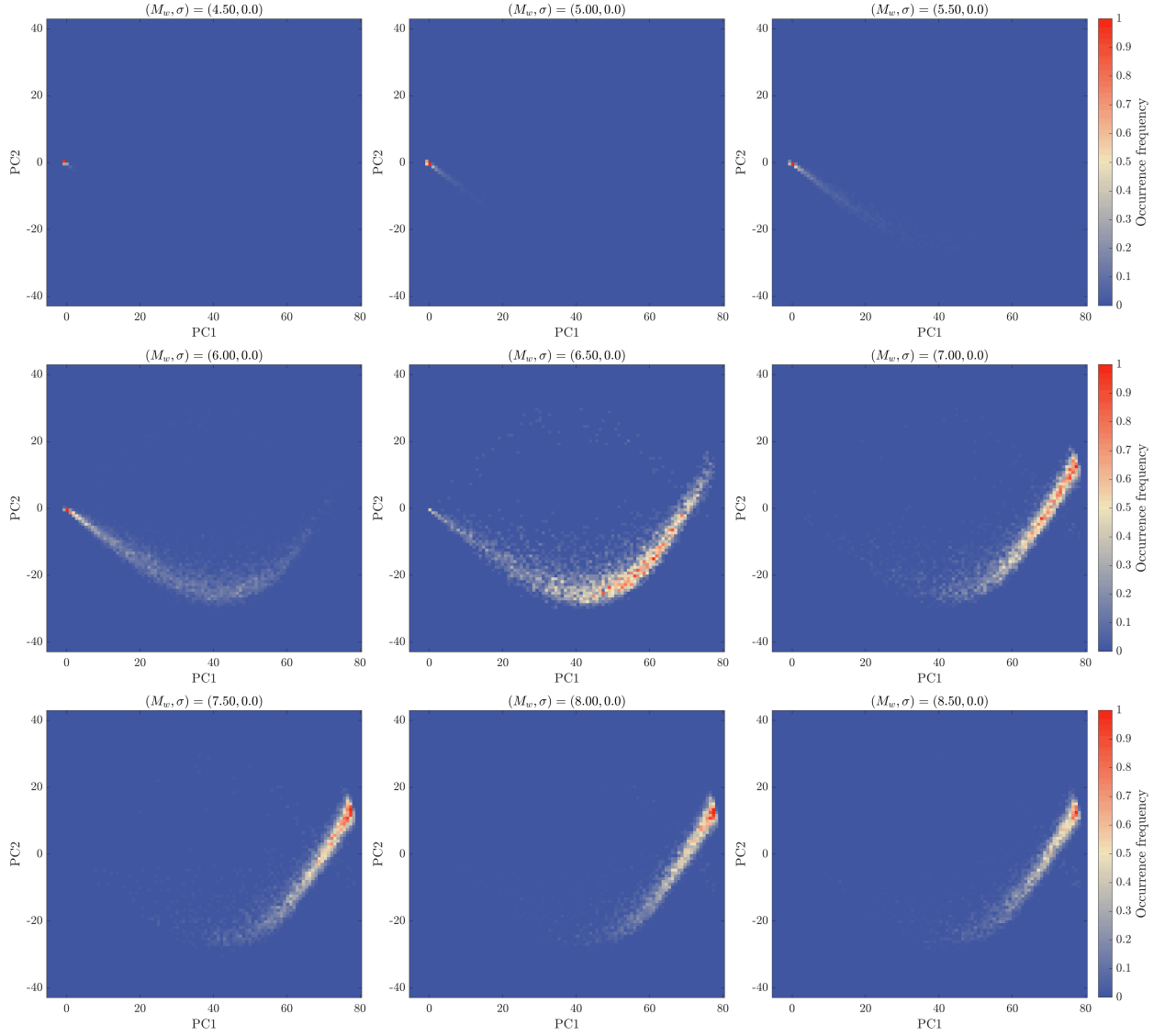
Supplementary Fig. 5: **Explained-variance spectra from principal component analysis (PCA).** Explained variance ratios of successive principal components are shown on linear (left) and log-log (right) scales for four analysis cases: Milpitas and northeastern San Francisco under first-order (fixed $\sigma = 0$) and second-order (fixed $M_w = M_{w_c}$) conditions. The first principal component dominates the variance, particularly for the first-order scenarios, indicating that the collective behavior is largely captured by a single order parameter. For the second-order scenarios, the variance is distributed across multiple components, consistent with the gradual and correlated reorganization of the system as structural diversity increases. The overall lower explained variance in the San Francisco cases reflects weaker inter-building dependence and a more Gaussian-like distribution of regional damage fractions.



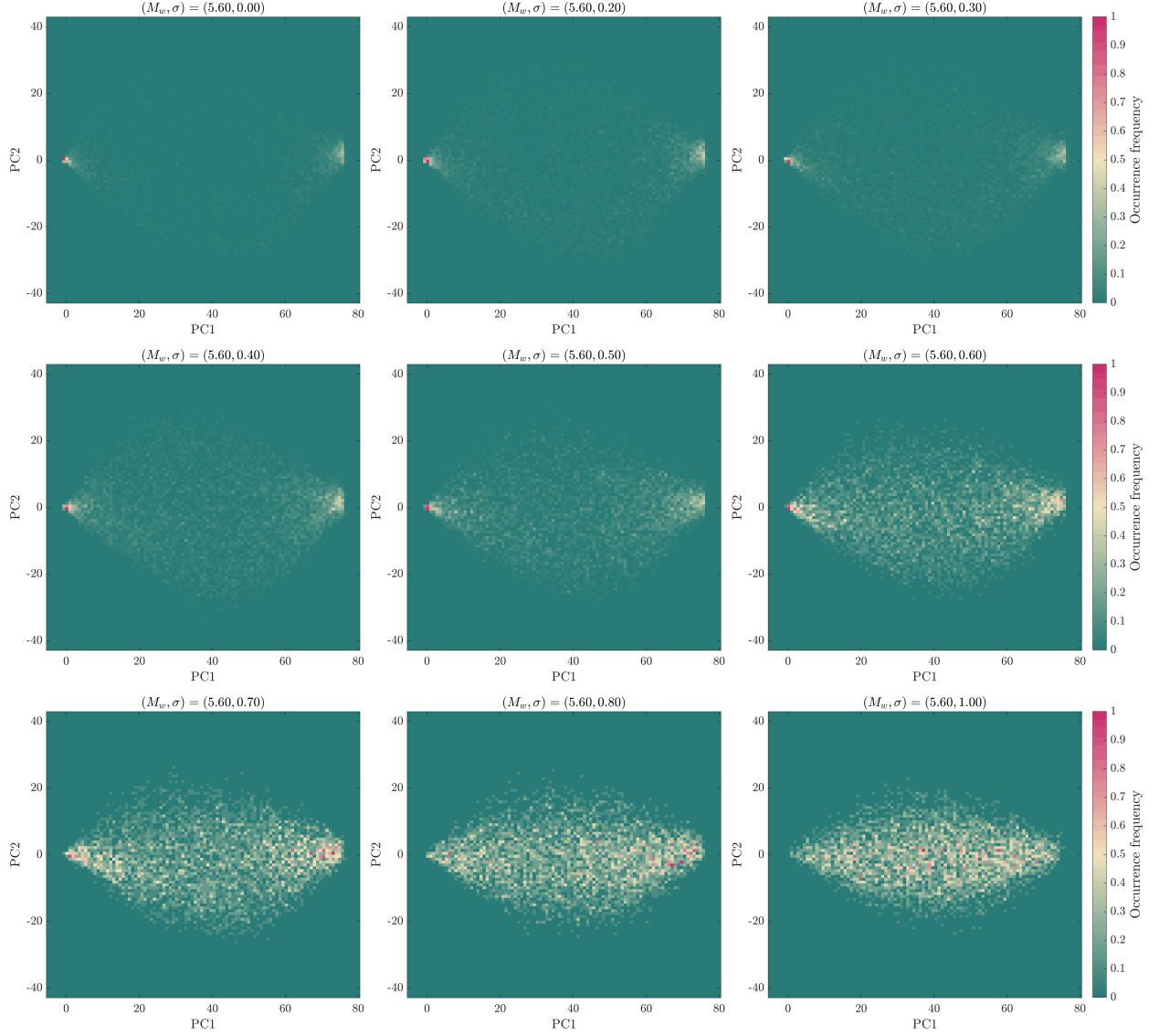
Supplementary Fig. 6: **Equivalence between the first principal component and the regional damage fraction.** The first principal component (PC1) obtained from principal component analysis (PCA) is plotted against the regional damage fraction for two study regions (Milpitas and northeastern San Francisco) under two simulation scenarios. The top row shows the first-order scenario, where the earthquake magnitude M_w is varied at fixed structural diversity $\sigma = 0$, and the bottom row shows the second-order scenario, where σ is varied at fixed $M_w = M_{w_c}$. Ten realizations are shown for each control parameter (M_w or σ), where each point represents a single simulation realization, colored by the corresponding control parameter. In all cases, PC1 exhibits a near one-to-one correspondence with the damage fraction, demonstrating that the dominant mode identified purely from data coincides with the physically interpretable order parameter of the system.



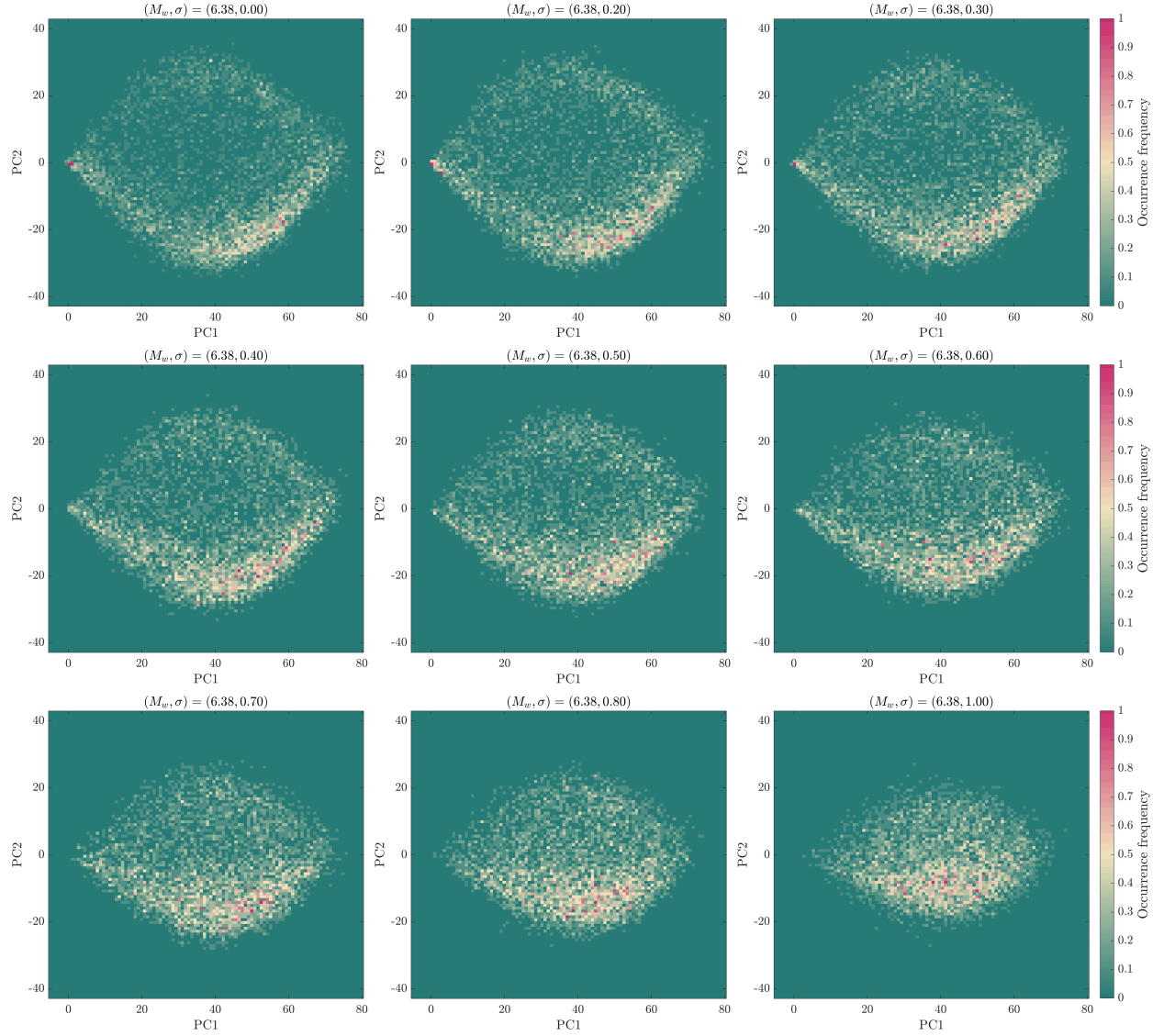
Supplementary Fig. 7: **Evolution of the projected PCA space with increasing earthquake magnitude for Milpitas.** Simulation realizations are projected into the space spanned by the first and second principal components (PC1 and PC2) at fixed structural diversity $\sigma = 0.0$ as the earthquake magnitude M_w increases. Each panel corresponds to a different (M_w, σ) condition, with color indicating the normalized occurrence frequency from 5,000 realizations. The distribution exhibits an abrupt shift from the left to the right cluster in PC1 around $M_w \approx 5.60$, marking a sudden transition from the collectively safe to the collectively damaged state, characteristic of a first-order phase transition.



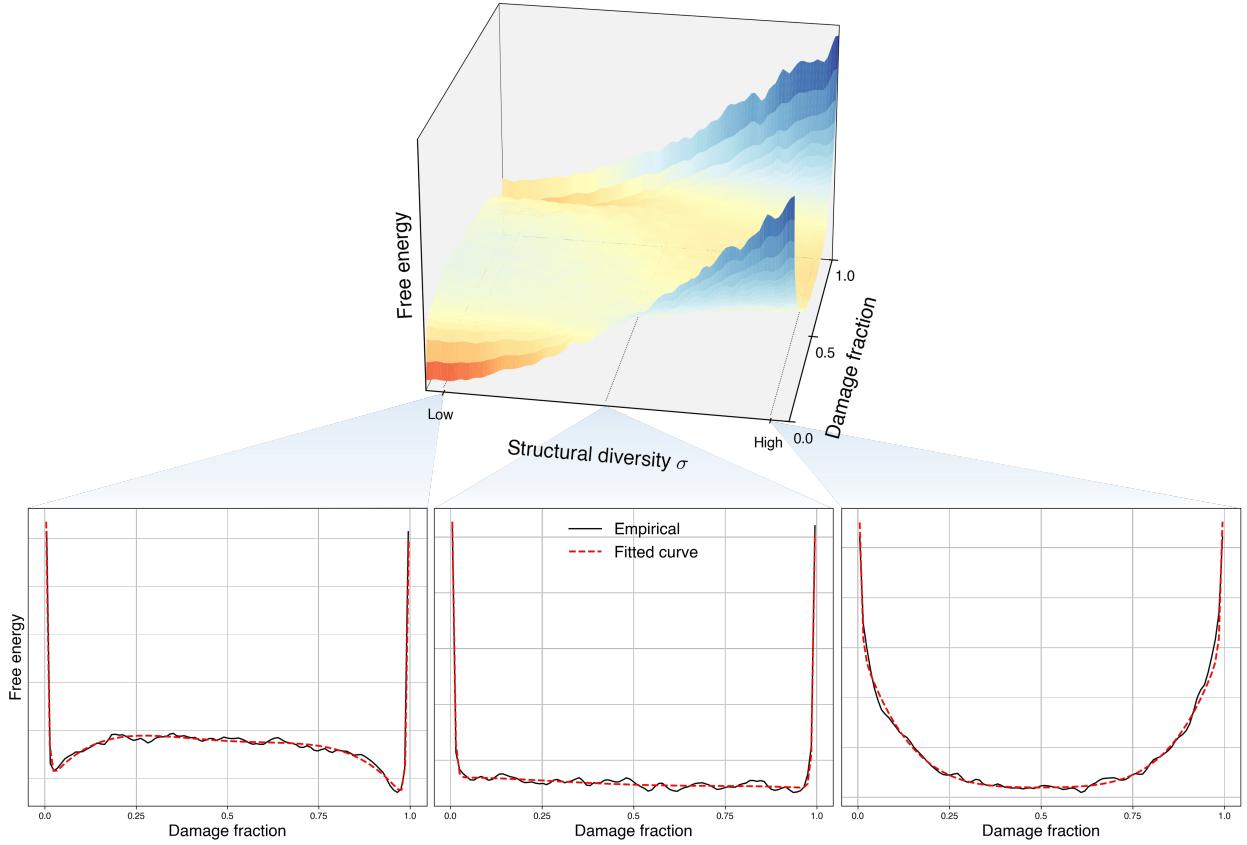
Supplementary Fig. 8: **Evolution of the projected PCA space with increasing earthquake magnitude for north-eastern San Francisco.** Same analysis setup as in Supplementary Fig. 7, performed for San Francisco at fixed structural diversity $\sigma = 0.0$. As M_w increases, the distribution shifts gradually and forms a smooth curved trajectory along PC1-PC2 without an abrupt jump, indicating the absence of a sharp first-order transition. This continuous evolution reflects weaker inter-building coupling and higher intrinsic diversity in the San Francisco region.



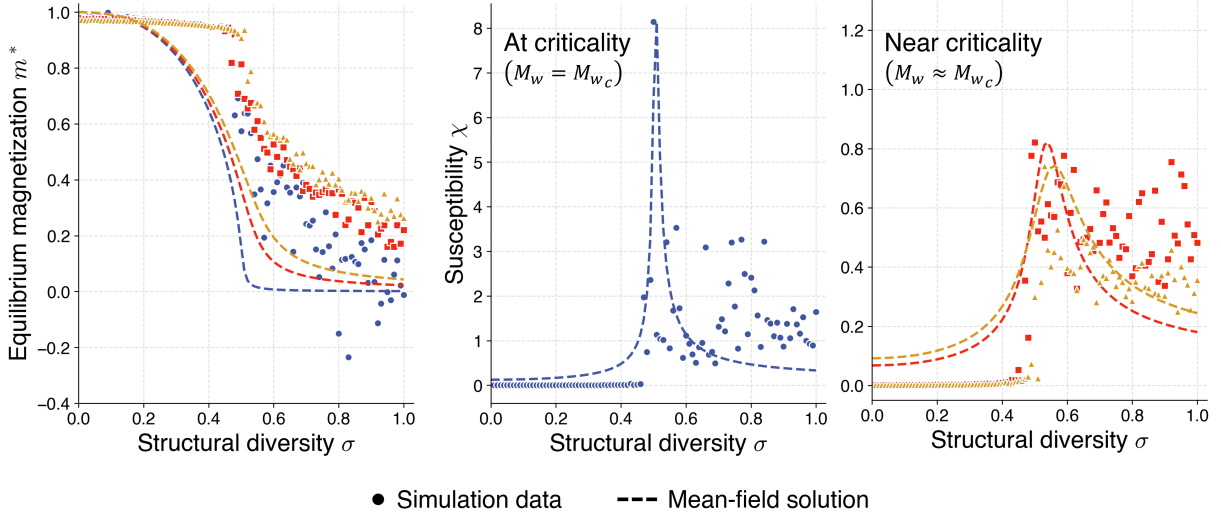
Supplementary Fig. 9: **Evolution of the projected PCA space with increasing structural diversity for Milpitas.** Simulation realizations are projected into the space spanned by PC1 and PC2 for Milpitas at fixed earthquake magnitude $M_w = 5.60$ under increasing structural diversity σ . Each panel shows the normalized occurrence frequency computed from 5,000 realizations. With increasing σ , the initially bimodal distribution along PC1 gradually merges into a single broadened cluster, reflecting a continuous transition from an ordered to a disordered regime, consistent with second-order-like behavior.



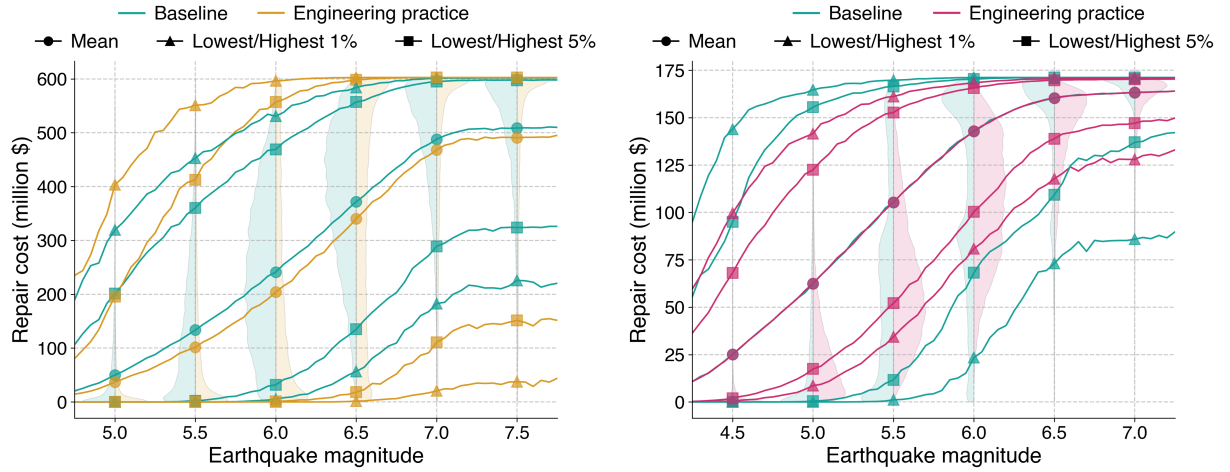
Supplementary Fig. 10: Evolution of the projected PCA space with increasing structural diversity for northeastern San Francisco. Same analysis setup as in Supplementary Fig. 9, performed for San Francisco at fixed earthquake magnitude $M_w = 6.38$. As σ increases, the distribution contracts slightly toward the central cluster but does not exhibit any fundamental reorganization across structural diversity. This behavior visually confirms that the region remains in a disordered, paramagnetic-like phase without undergoing a phase transition.



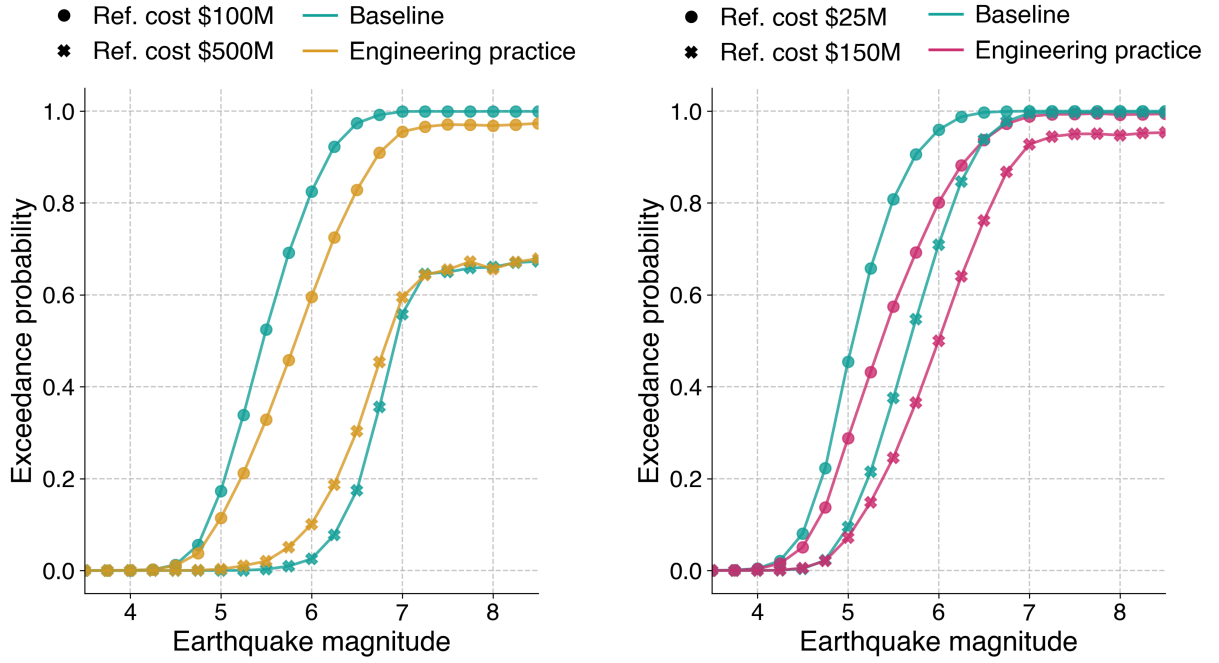
Supplementary Fig. 11: **Data-driven Landau free-energy landscape.** For each (M_w, σ) , we form the empirical distribution $P(m)$ by histogramming the simulated damage fraction m_d after mapping to $m \in [-1, 1]$ (with $m_d = (m + 1)/2$), and define the empirical free energy $F_{\text{emp}}(m) \propto -\ln P(m)$. We fit $F_{\text{emp}}(m)$ with a polynomial Landau form $F_{\text{poly}}(m) = c_0 + c_1 m + c_2 m^2 + c_4 m^4 + c_k m^k$, using $k = 100$ for the stabilizing high-order term. The 3D surface (top) shows $F_{\text{emp}}(m)$, and the 2D projections (bottom) show cross-sections with the fitted $F_{\text{poly}}(m)$ for three representative cases: $\sigma < \sigma_c$ (left), $\sigma \approx \sigma_c$ (center), and $\sigma > \sigma_c$ (right). This polynomial-fit Landau free energy enables curvature-based susceptibility estimates (Supplementary Fig. 12).



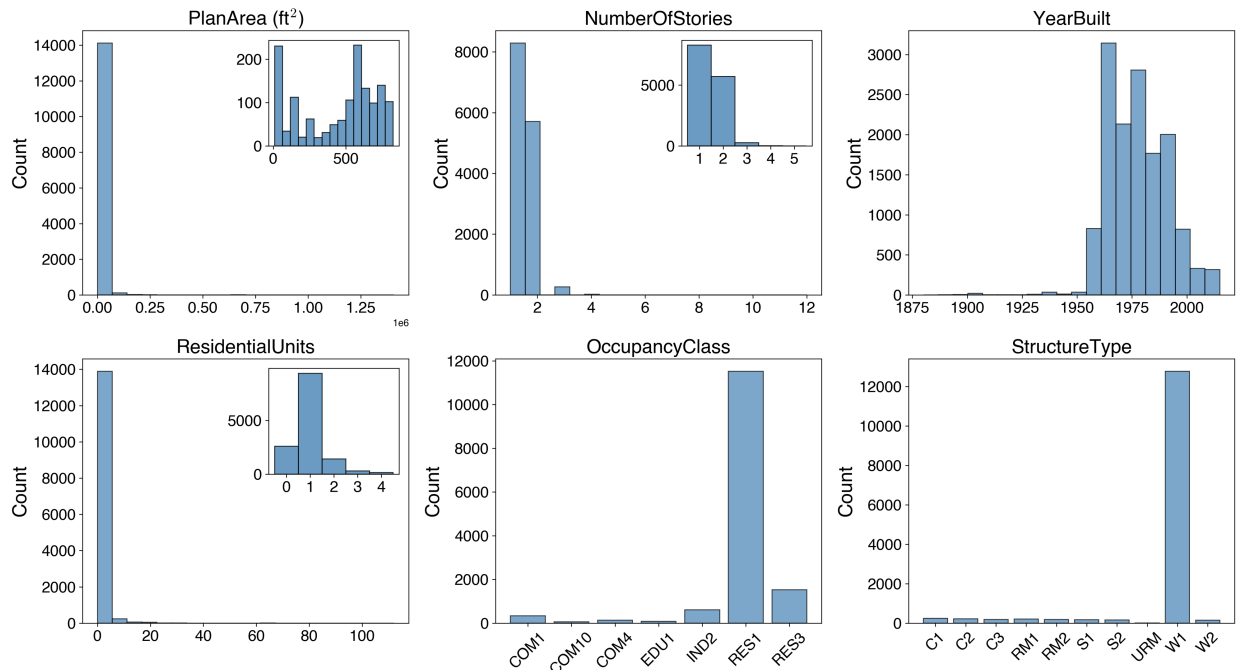
Supplementary Fig. 12: **Equilibrium magnetization and susceptibility from the data-driven Landau free-energy landscape.** Equilibrium magnetization m^* (left) and curvature-based susceptibility χ inferred from the polynomial-fit empirical free energy $F_{\text{poly}}(m)$ (Supplementary Method 4; Supplementary Fig. 11). Blue, red, and yellow indicate $M_w = 5.55, 5.60$, and 5.65 cases. For each (M_w, σ) , m^* is obtained from the minimum of $F_{\text{poly}}(m)$ and χ from the inverse curvature at m^* , $\chi^{-1} = \partial^2 F_{\text{poly}} / \partial m^2|_{m=m^*}$. The center and right panels report χ at criticality ($M_w = M_{wc}$) and near criticality ($M_w \approx M_{wc}$), respectively. Markers show simulation-based estimates from a single portfolio realization and dashed lines indicate the mean-field prediction. The lingering magnetization and slowly decaying susceptibility for $\sigma > \sigma_c$ are consistent with the Griffiths-like behavior described in Figs. 2d,e



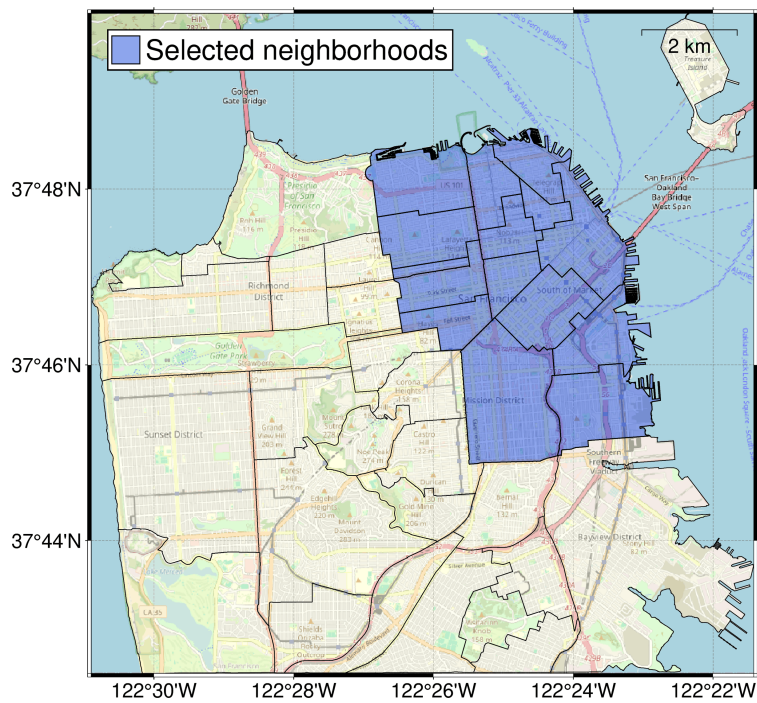
Supplementary Fig. 13: **Mean and quantile values of regional repair-cost distributions computed with and without engineering simplifications.** Left: northeastern San Francisco portfolio; right: Milpitas portfolio. The background violins show the full repair-cost distributions at representative earthquake magnitudes. Mean repair costs are largely insensitive to engineering simplifications, whereas the lower and upper 5% quantiles differ substantially. In the northeastern San Francisco case (left), structural categorization pushes the lower and upper quantile curves farther apart; overestimating upper-tail losses and underestimating lower-tail losses. In Milpitas (right), the conditional-independence assumption has the opposite effect, drawing the two quantile curves closer together by reducing upper-tail losses and inflating lower-tail estimates.



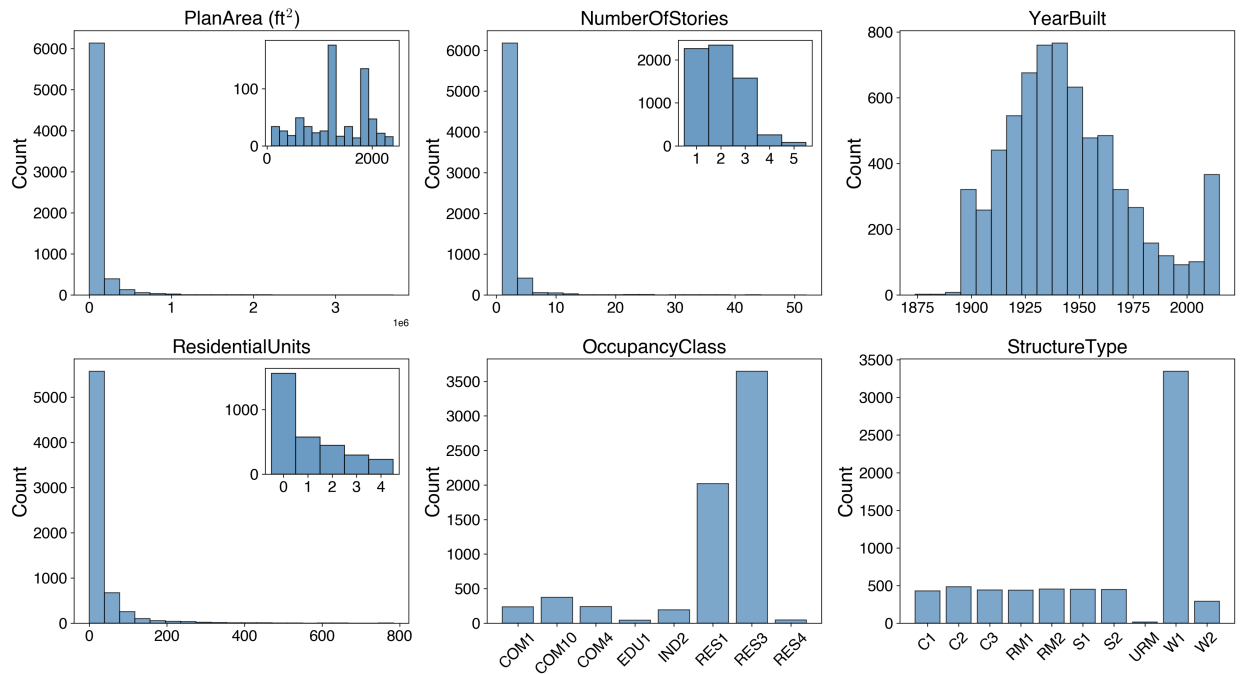
Supplementary Fig. 14: **Exceedance probabilities for two reference repair costs.** Left: northeastern San Francisco portfolio; right: Milpitas portfolio. Curves show the probability that regional repair costs exceed two reference thresholds (circles: lower threshold; crosses: higher threshold) with and without engineering simplifications. In both regions, exceedance probabilities shift noticeably when engineering simplifications are applied.



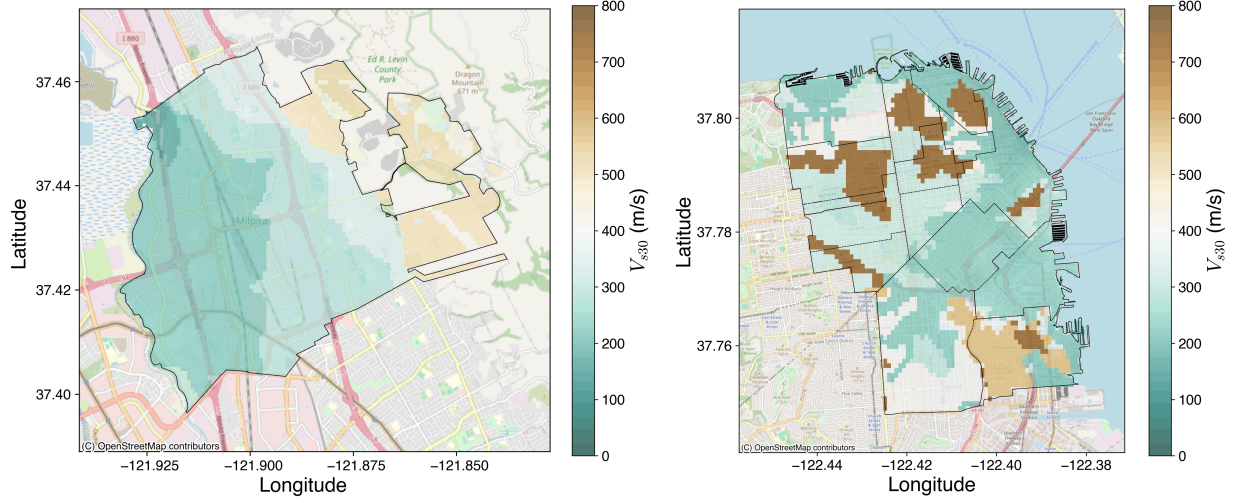
Supplementary Fig. 15: **Distributions of building attributes for the Milpitas portfolio.** Histograms show the distributions of key building attributes, including plan area, number of stories, construction year, residential units, occupancy class, and structure type. Insets magnify the histograms near small values.



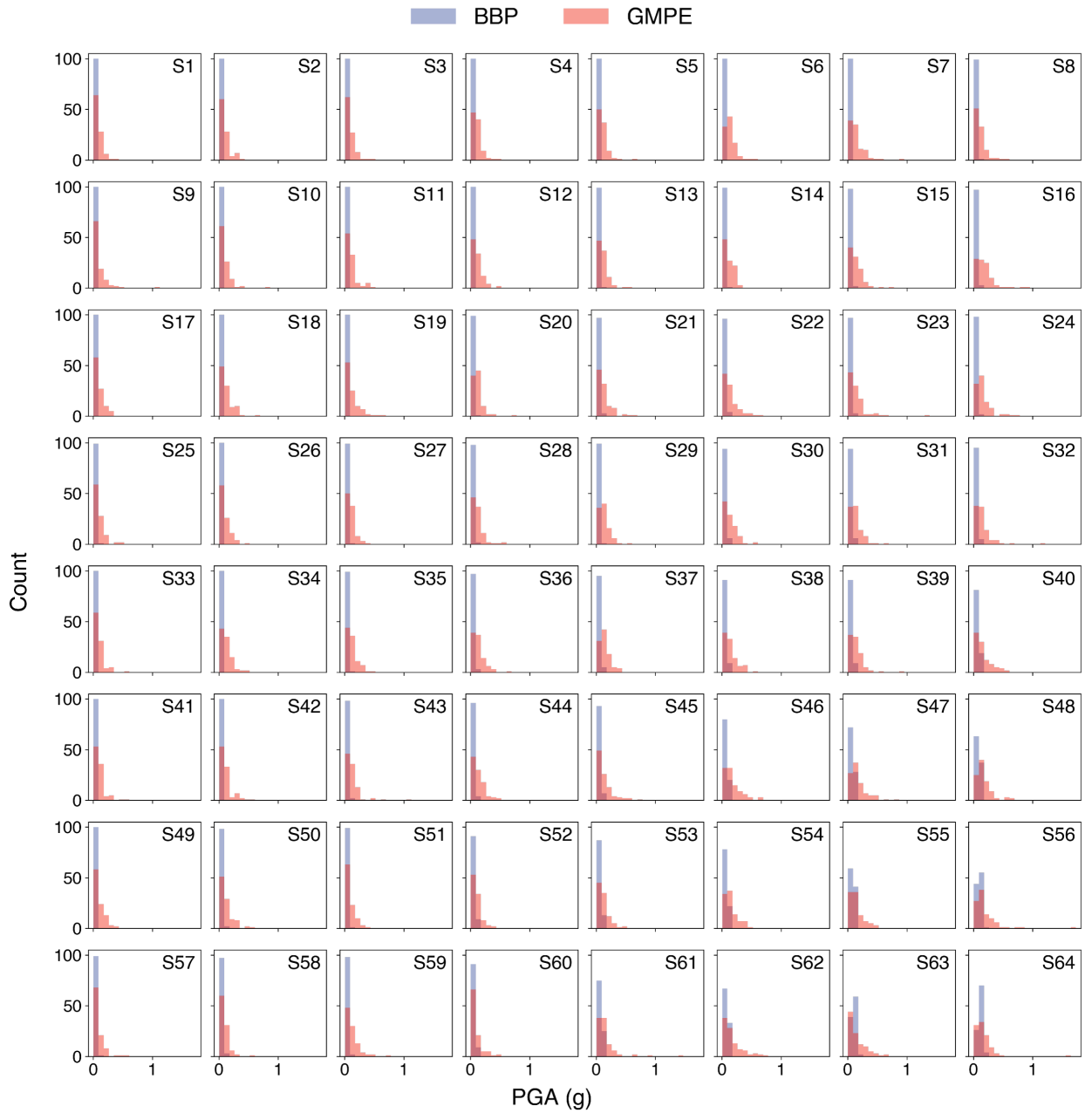
Supplementary Fig. 16: **Selected neighborhoods in northeastern San Francisco.** The analyzed region includes major commercial districts such as the Financial District and Mission Bay, as well as residential neighborhoods including Pacific Heights and Hayes Valley. The highlighted area represents the subset of neighborhoods selected for the building portfolio analysis.



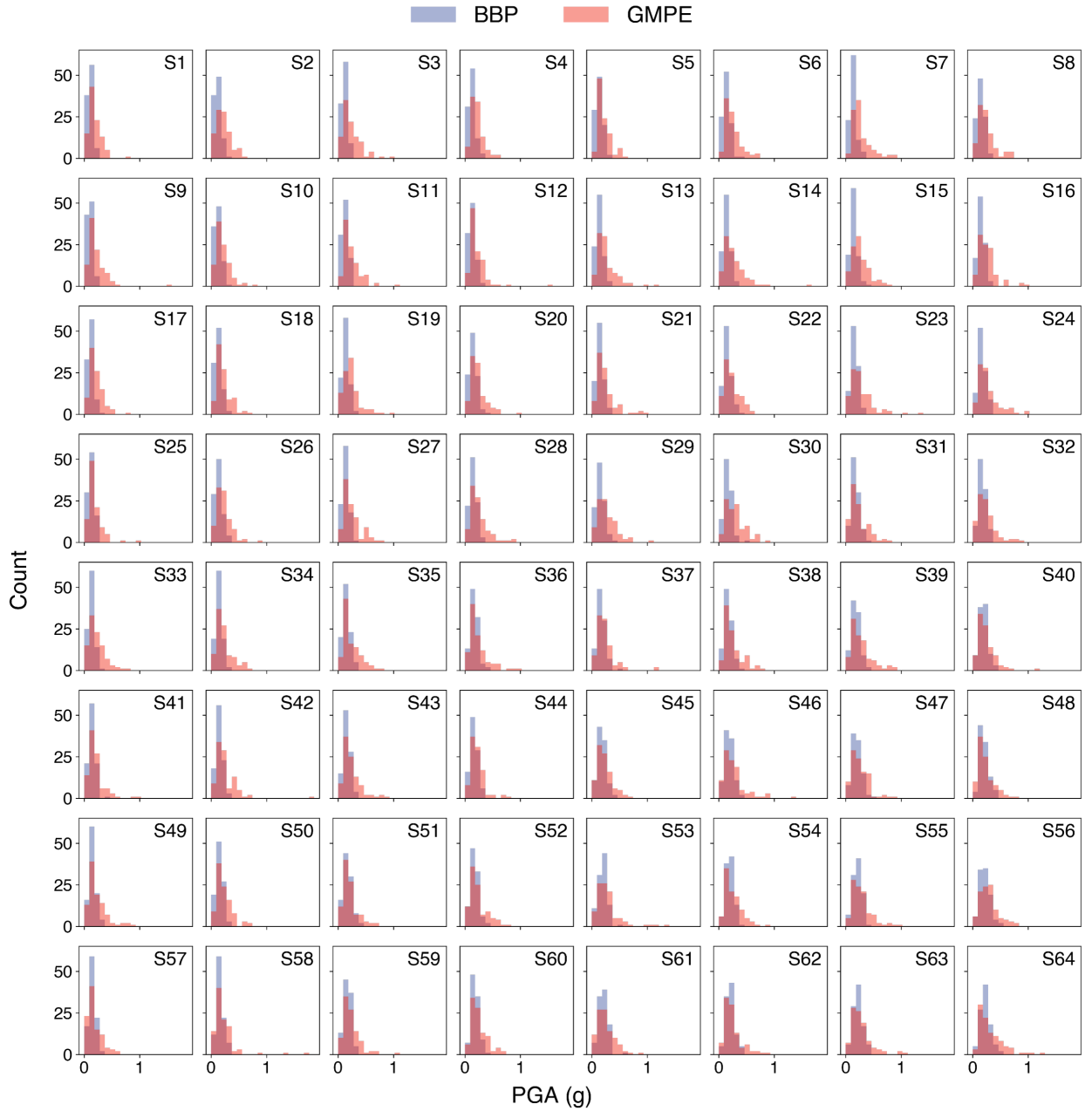
Supplementary Fig. 17: **Distributions of building attributes for the northeastern San Francisco portfolio.** Histograms show the distributions of key building attributes, including plan area, number of stories, construction year, residential units, occupancy class, and structure type. Insets magnify the histograms near small values.



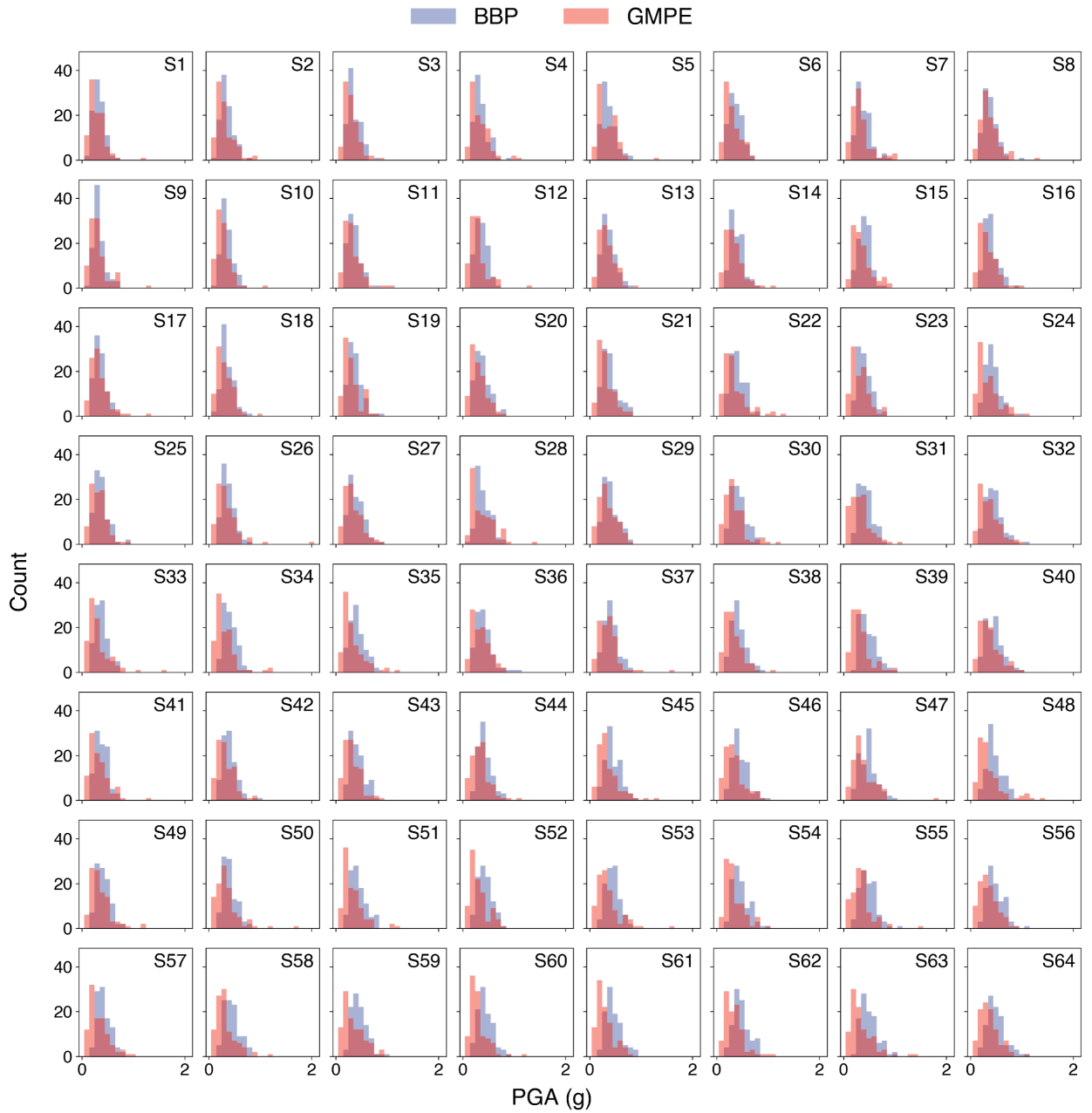
Supplementary Fig. 18: **Maps of the near-surface shear-wave velocity V_{s30} for Milpitas (left) and northeastern San Francisco (right).** The values are retrieved from Thompson [24]. The selected San Francisco region exhibits greater heterogeneity in this geomechanical property, which strongly influences seismic response, as well as greater variation in building types.



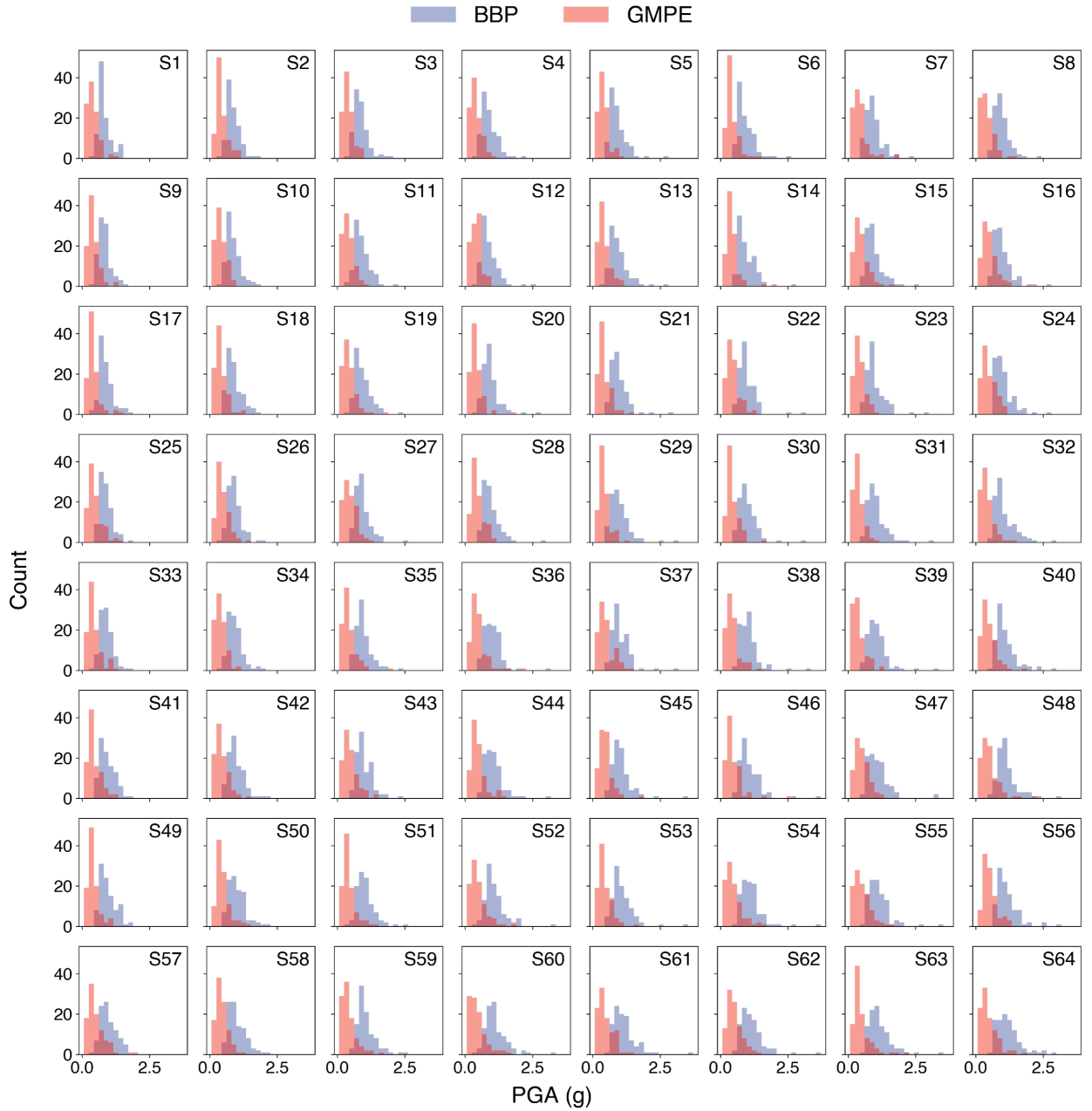
Supplementary Fig. 19: **Comparison of peak ground acceleration (PGA) distributions between physics-based and empirical models at $M_w = 5.0$ across recording stations.** Histograms compare PGA values obtained from the physics-based SCEC Broadband Platform (BBP) simulations and the empirical Chiou and Youngs ground-motion prediction equation (GMPE). Both datasets were sampled at the same 64 recording stations (S1–S64) uniformly distributed across Milpitas, with 100 realizations generated for each method.



Supplementary Fig. 20: **Comparison of peak ground acceleration (PGA) distributions between physics-based and empirical models at $M_w = 6.0$ across recording stations.** Histograms compare PGA values obtained from the physics-based SCEC Broadband Platform (BBP) simulations and the empirical Chiou and Youngs ground-motion prediction equation (GMPE). Both datasets were sampled at the same 64 recording stations (S1–S64) uniformly distributed across Milpitas, with 100 realizations generated for each method.



Supplementary Fig. 21: **Comparison of peak ground acceleration (PGA) distributions between physics-based and empirical models at $M_w = 7.0$ across recording stations.** Histograms compare PGA values obtained from the physics-based SCEC Broadband Platform (BBP) simulations and the empirical Chiou and Youngs ground-motion prediction equation (GMPE). Both datasets were sampled at the same 64 recording stations (S1–S64) uniformly distributed across Milpitas, with 100 realizations generated for each method.



Supplementary Fig. 22: **Comparison of peak ground acceleration (PGA) distributions between physics-based and empirical models at $M_w = 8.0$ across recording stations.** Histograms compare PGA values obtained from the physics-based SCEC Broadband Platform (BBP) simulations and the empirical Chiou and Youngs ground-motion prediction equation (GMPE). Both datasets were sampled at the same 64 recording stations (S1–S64) uniformly distributed across Milpitas, with 100 realizations generated for each method.

Supplementary References

- [1] Norman A. Abrahamson, Walter J. Silva, and Ronnie Kamai. Summary of the ASK14 Ground Motion Relation for Active Crustal Regions. *Earthquake Spectra*, 30(3):1025–1055, August 2014. ISSN 8755-2930, 1944-8201. doi: 10.1193/070913EQS198M. URL <https://journals.sagepub.com/doi/10.1193/070913EQS198M>.
- [2] Timothy D. Ancheta, Robert B. Darragh, Jonathan P. Stewart, Emel Seyhan, Walter J. Silva, Brian S.-J. Chiou, Katie E. Wooddell, Robert W. Graves, Albert R. Kottke, David M. Boore, Tadahiro Kishida, and Jennifer L. Donahue. NGA-West2 Database. *Earthquake Spectra*, 30(3):989–1005, August 2014. ISSN 8755-2930, 1944-8201. doi: 10.1193/070913EQS197M. URL <https://journals.sagepub.com/doi/10.1193/070913EQS197M>.
- [3] Applied Technology Council. Seismic performance assessment of buildings, volume 1 – methodology, second edition. Technical Report FEMA P-58-1, Federal Emergency Management Agency (FEMA), Washington, D.C., December 2018. URL <https://www.atcouncil.org/>. Prepared by the Applied Technology Council for the Federal Emergency Management Agency. Project Officers: Michael Mahoney and Robert D. Hanson.
- [4] Geoff Boeing. Modeling and Analyzing Urban Networks and Amenities With OSMnx. *Geographical Analysis*, 57(4):567–577, October 2025. ISSN 0016-7363, 1538-4632. doi: 10.1111/gean.70009. URL <https://onlinelibrary.wiley.com/doi/10.1111/gean.70009>.
- [5] David M. Boore, Jonathan P. Stewart, Emel Seyhan, and Gail M. Atkinson. NGA-West2 Equations for Predicting PGA, PGV, and 5% Damped PSA for Shallow Crustal Earthquakes. *Earthquake Spectra*, 30(3):1057–1085, August 2014. ISSN 8755-2930, 1944-8201. doi: 10.1193/070113EQS184M. URL <https://journals.sagepub.com/doi/10.1193/070113EQS184M>.
- [6] Yousef Bozorgnia, Norman A. Abrahamson, Linda Al Atik, Timothy D. Ancheta, Gail M. Atkinson, Jack W. Baker, Annemarie Baltay, David M. Boore, Kenneth W. Campbell, Brian S.J. Chiou, Robert Darragh, Steve Day, Jennifer Donahue, Robert W. Graves, Nick Gregor, Thomas Hanks, I. M. Idriss, Ronnie Kamai, Tadahiro Kishida, Albert Kottke, Stephen A. Mahin, Sanaz Rezaeian, Badie Rowshandel, Emel Seyhan, Shrey Shahi, Tom Shantz, Walter Silva, Paul Spudich, Jonathan P. Stewart, Jennie Watson-Lamprey, Kathryn Wooddell, and Robert Youngs. NGA-West2 research project. *Earth-*

quake Spectra, 30(3):973–987, August 2014. ISSN 19448201. doi: 10.1193/072113EQS209M. Publisher: Earthquake Engineering Research Institute.

- [7] Serena Bradde and William Bialek. PCA Meets RG. *Journal of Statistical Physics*, 167(3-4):462–475, May 2017. ISSN 0022-4715, 1572-9613. doi: 10.1007/s10955-017-1770-6. URL <http://link.springer.com/10.1007/s10955-017-1770-6>.
- [8] Kenneth W. Campbell and Yousef Bozorgnia. NGA-West2 Ground Motion Model for the Average Horizontal Components of PGA, PGV, and 5% Damped Linear Acceleration Response Spectra. *Earthquake Spectra*, 30(3):1087–1115, August 2014. ISSN 8755-2930, 1944-8201. doi: 10.1193/062913EQS175M. URL <https://journals.sagepub.com/doi/10.1193/062913EQS175M>.
- [9] Xu-Yang Cao, De-Cheng Feng, and Michael Beer. A KDE-based non-parametric cloud approach for efficient seismic fragility estimation of structures under non-stationary excitation. *Mechanical Systems and Signal Processing*, 205:110873, December 2023. ISSN 08883270. doi: 10.1016/j.ymssp.2023.110873. URL <https://linkinghub.elsevier.com/retrieve/pii/S0888327023007811>.
- [10] Brian S.-J. Chiou and Robert R. Youngs. Update of the Chiou and Youngs NGA Model for the Average Horizontal Component of Peak Ground Motion and Response Spectra. *Earthquake Spectra*, 30(3):1117–1153, August 2014. ISSN 8755-2930, 1944-8201. doi: 10.1193/072813EQS219M. URL <https://journals.sagepub.com/doi/10.1193/072813EQS219M>.
- [11] City and County of San Francisco. Analysis neighborhoods. <https://data.sfgov.org/dataset/Analysis-Neighborhoods/p5b7-5n3h>, 2024. Accessed October 21, 2025.
- [12] Federal Emergency Management Agency (FEMA). Hazus Earthquake Model Technical Manual: Hazus 6.1. Technical report, Federal Emergency Management Agency, Washington, D.C., July 2024. URL <https://www.fema.gov/flood-maps/products-tools/hazus>.
- [13] Pablo Heresi and Eduardo Miranda. Structure-to-structure damage correlation for scenario-based regional seismic risk assessment. *Structural Safety*, 95, March 2022. ISSN 01674730. doi: 10.1016/j.strusafe.2021.102155. Publisher: Elsevier B.V.
- [14] Wenjian Hu, Rajiv R. P. Singh, and Richard T. Scalettar. Discovering phases, phase transitions, and crossovers through unsupervised machine learning: A critical examination. *Physical Review E*, 95(6):062122, June 2017. ISSN 2470-0045, 2470-0053. doi: 10.1103/PhysRevE.95.062122. URL <https://link.aps.org/doi/10.1103/PhysRevE.95.062122>.

[15] Nirmal Jayaram, Jack W Baker, N Jayaram, and J W Baker. Correlation model for spatially distributed ground-motion intensities. *Earthquake Engineering & Structural Dynamics*, 38(15):1687–1708, 12 2009. ISSN 1096-9845. doi: 10.1002/EQE.922. URL <https://onlinelibrary.wiley.com/doi/full/10.1002/eqe.922><https://onlinelibrary.wiley.com/doi/abs/10.1002/eqe.922><https://onlinelibrary.wiley.com/doi/10.1002/eqe.922>.

[16] Chulyoung Kang, Oh Sung Kwon, and Junho Song. Evaluation of correlation between engineering demand parameters of structures for seismic system reliability analysis. *Structural Safety*, 93, 11 2021. ISSN 01674730. doi: 10.1016/j.strusafe.2021.102133.

[17] Albert Kottke, Greg Lavrentiadis, Nasser Marafi, M. Bahrampouri, and Renmin Pretell. arkotke/pygmm: v0.8.0 (2025-07-24), 2025. URL <https://doi.org/10.5281/zenodo.16422451>.

[18] Xinzheng Lu, Frank McKenna, Qingle Cheng, Zhen Xu, Xiang Zeng, and Stephen A Mahin. An open-source framework for regional earthquake loss estimation using the city-scale nonlinear time history analysis. *Earthquake Spectra*, 36(2):806–831, May 2020. ISSN 8755-2930, 1944-8201. doi: 10.1177/8755293019891724. URL <https://journals.sagepub.com/doi/10.1177/8755293019891724>.

[19] Chu Mai, Katerina Konakli, and Bruno Sudret. Seismic fragility curves for structures using non-parametric representations. *Frontiers of Structural and Civil Engineering*, 11(2):169–186, June 2017. ISSN 2095-2430, 2095-2449. doi: 10.1007/s11709-017-0385-y. URL <http://link.springer.com/10.1007/s11709-017-0385-y>.

[20] Frank McKenna. OpenSees: A Framework for Earthquake Engineering Simulation. *Computing in Science & Engineering*, 13(4):58–66, 2011.

[21] Frank McKenna, Stevan Gavrilovic, Jinyan Zhao, Kuanshi Zhong, Adam Zsarnoczay, Barbaros Cetiner, Sina Naeimi, Sang ri Yi, Akash Bangalore Satish, Amin Packzad, Pedro Arduino, and Wael Elhaddad. NHERI-SimCenter/R2DTool: Version 5.5.0 (v5.5.0), 2025. URL <https://doi.org/10.5281/zenodo.16884221>. NHERI SimCenter, Rapid Regional Resilience Determination Tool (R2DTool).

[22] Sebin Oh, Sangri Yi, and Ziqi Wang. Long-range Ising model for regional-scale seismic risk analysis. *Earthquake Engineering & Structural Dynamics*, 53(12):3904–3923, 2024.

[23] OpenStreetMap contributors. Planet dump retrieved from <https://planet.osm.org> . <https://www.openstreetmap.org>, 2017.

[24] Eric M. Thompson. An updated Vs30 map for california with geologic and topographic constraints (ver. 2.0, july 2022), 2018. URL <https://doi.org/10.5066/F7JQ108S>. U.S. Geological Survey data release.

[25] Dimitrios Vamvatsikos and C. Allin Cornell. Incremental dynamic analysis. *Earthquake Engineering & Structural Dynamics*, 31(3):491–514, March 2002. ISSN 0098-8847, 1096-9845. doi: 10.1002/eqe.141. URL <https://onlinelibrary.wiley.com/doi/10.1002/eqe.141>.

[26] Lei Wang. Discovering phase transitions with unsupervised learning. *Physical Review B*, 94(19):195105, November 2016. ISSN 2469-9950, 2469-9969. doi: 10.1103/PhysRevB.94.195105. URL <https://link.aps.org/doi/10.1103/PhysRevB.94.195105>.

[27] Donald L. Wells and Kevin J. Coppersmith. New empirical relationships among magnitude, rupture length, rupture width, rupture area, and surface displacement. *Bulletin of the Seismological Society of America*, 84(4):974–1002, August 1994. ISSN 1943-3573, 0037-1106. doi: 10.1785/BSSA0840040974. URL <https://pubs.geoscienceworld.org/bssa/article/84/4/974/119792/New-empirical-relationships-among-magnitude>.

[28] Mengjie Xiang, Jiaxu Shen, Zekun Xu, and Jun Chen. Structure-to-structure seismic damage correlation model. *Earthquake Engineering & Structural Dynamics*, 53(10):3205–3229, 2024. ISSN 1096-9845. doi: 10.1002/eqe.4172. URL <https://onlinelibrary.wiley.com/doi/abs/10.1002/eqe.4172>. _eprint: <https://onlinelibrary.wiley.com/doi/pdf/10.1002/eqe.4172>.

[29] Tian You and Solomon Tesfamariam. Spatial correlation in building seismic performance for regional resilience assessment. *Resilient Cities and Structures*, 3(2):57–65, June 2024. ISSN 27727416. doi: 10.1016/j.rcns.2024.06.004. URL <https://linkinghub.elsevier.com/retrieve/pii/S2772741624000267>.

[30] Jian Zhong, Sien Zhou, Hao Wang, and Huimin Hu. Regional seismic fragility of bridge network derived by covariance matrix model of bridge portfolios. *Engineering Structures*, 309, June 2024. ISSN 18737323. doi: 10.1016/j.engstruct.2024.118035. Publisher: Elsevier Ltd.

[31] Minjie Zhu, Frank McKenna, and Michael H. Scott. OpenSeesPy: Python library for the OpenSees finite element framework. *SoftwareX*, 7:6–11, January 2018. ISSN 23527110. doi: 10.1016/j.softx.2017.10.009. URL <https://linkinghub.elsevier.com/retrieve/pii/S2352711017300584>.

[32] Adam Zsarnóczay, Wael Elhaddad, Barbaros Cetiner, Kuanshi Zhong, Frank McKenna, and Gregory Deierlein. SimCenter Earthquake Testbed: San Francisco, CA, 2023. URL <https://www.designsafe-ci.org/data/browser/public/designsafe.storage.published/PRJ-3880>.